# A Nonlinear Wave Load Model for Extreme and Fatigue Responses of Offshore Floating Wind Turbines

by

Sungho Lee



Submitted to the Department of Mechanical Engineering
in partial fulfillment of the requirements for the degree of

Doctor of Philosophy in Mechanical Engineering

at the

MASSACHUSETTS INSTITUTE OF TECHNOLOGY

June 2012



Author:.....

Department of Mechanical Engineering
April 24, 2012

Certified by:.....

Paul D. Sclavounos
Professor of Mechanical Engineering
Thesis Supervisor

Accepted by:.....

David E. Hardt
Chairman, Department Committee on Graduate Students

# A Nonlinear Wave Load Model for Extreme and Fatigue Responses of Offshore Floating Wind Turbines

by

Sungho Lee

## Abstract

Ocean energy is one of the most important sources of alternative energy and offshore floating wind turbines are considered viable and economical means of harnessing ocean energy. The accurate prediction of nonlinear hydrodynamic wave loads and the resulting nonlinear motion and tether tension is of crucial importance in the design of floating wind turbines.

A new theoretical framework is presented for analyzing hydrodynamic forces on floating bodies which is potentially applicable in a wide range of problems in ocean engineering. The total fluid force acting on a floating body is obtained by the time rate of change of the impulse of the velocity potential flow around the body. This new model called Fluid Impulse Theory is used to address the nonlinear hydrodynamic wave loads and the resulting nonlinear responses of floating wind turbine for various wave conditions in a highly efficient and robust manner in time domain.

A three-dimensional time domain hydrodynamic wave-body interaction computational solver is developed in the frame work of a boundary element method based on the transient free-surface Green-function. By applying a numerical treatment that takes the free-surface boundary conditions linearized at the incident wave surface and takes the body boundary condition satisfied on the instantaneous underwater surface of the moving body, it simulates a potential flow in conjunction with the Fluid Impulse Theory for nonlinear wave-body interaction problems of large-amplitude waves and motions in time domain.

Several results are presented from the application of the Fluid Impulse Theory to the extreme and fatigue wave load model: the time domain analysis of nonlinear dynamic response of floating wind turbine for extreme wave events and the time domain analysis of nonlinear wave load for an irregular sea state followed by a power spectral density analysis.

Thesis Supervisor: Paul D. Sclavounos

Title: Professor of Mechanical Engineering

# Acknowledgements

The author first wishes to express grateful thanks to his advisor, Professor Paul D. Sclavounos. His infinite encouragement, guidance, and patience were all greatly appreciated throughout the long haul. Greatest thanks are due to my parents, whose endless love and encouragement have supported me throughout many years of school. Finally, the author wishes to thank his wife, and also his best friend, Dr. Jieun Choi. Her tremendous patience and support got me to the end of this long journey. Also, financial supports from the United States Office of Naval Research and the Alstom Wind are all gratefully acknowledged.

# Contents

# List of Figures

Figure 3-39: Incident wave elevation ($\zeta_I$) from the mean waterline; Horizontal load on anchor; Vertical pull-out load on anchor; Net moment in pitch on anchor for incident wave of A=1m and w=0.5 rad/sec.

Figure 3-40: Incident wave elevation ($\zeta_I$) from the mean waterline; Motion in surge ($\xi_1$); Motion in heave ($\xi_3$) for incident wave of A=6m and w=0.5 rad/sec.

Figure 3-41: Incident wave elevation ($\zeta_I$) from the mean waterline; Tension of line#1 ($T_1^*$); Tension of line#2 ($T_2$) for incident wave of A=6m and w=0.5 rad/sec.

Figure 3-42: Incident wave elevation ($\zeta_I$) from the mean waterline; Horizontal load on anchor; Vertical pull-out load on anchor; Net moment in pitch on anchor for incident wave of A=6m and w=0.5 rad/sec.

Figure 3-43: Incident wave elevation ($\zeta_I$) from the mean waterline; Motion in surge ($\xi_1$); Motion in heave ($\xi_3$) for incident wave of A=10m and w=0.5 rad/sec.

Figure 3-44: Incident wave elevation ($\zeta_I$) from the mean waterline; Tension of line#1 ($T_1^*$); Tension of line#2 ($T_2$) for incident wave of A=10m and w=0.5 rad/sec.

Figure 3-45: Incident wave elevation ($\zeta_I$) from the mean waterline; Horizontal load on anchor; Vertical pull-out load on anchor; Net moment in pitch on anchor for incident wave of A=10m and w=0.5 rad/sec.

Figure 3-46: The power spectral density of wave exciting force in surge ($F_{Hydro_1}$) for irregular waves of $H_s$ = 6.0 m and $T_m$ = 11.6 sec.

Figure 3-47: The power spectral density of tether tension#2 $T_2(t)$ for irregular waves of $H_s$ = 6.0 m and $T_m$ = 11.6 sec.

# Chapter 1

# Introduction

## 1.1 Offshore Floating Wind Turbines

Ocean energy is one of the most reliable energy alternatives for countries that have sufficiently large wind and wave sources. Given the steady and strong wind energy resources off the coastline of many countries, the offshore wind farm has become highly attractive as an ideal energy solution ([33]). A floating wind turbine system is being considered a key solution to making offshore wind farms feasible from an economic standpoint, and viable as an energy resource.

The offshore floating wind turbine is a complex system that has multiple design objectives, variables and constraints, and this complexity requires an efficient and robust modeling and analysis method. A linear wave theory captures most of the leading order aspects of hydrodynamic wave loads on offshore structures in most sea states. A frequency domain analysis method based on linear wave theory provides an efficient way to explore the design space, to understand the system responses and to obtain fundamental insights into the optimization of the system's design.

Due to the stochastic characteristics of the ocean environment, a reliability-index-based design method with a spectral representation of ocean waves was adopted and has proven greatly useful as an efficient design space exploration tool for offshore floating wind turbines (Tracy [40], Lee [17] and Sclavounos, Tracy & Lee [36]). Two new design concepts were proposed and developed for a 3-5MW wind turbine as an application for shallow and intermediate water depths, *i.e.* the tension leg platform (TLP) and the tension leg buoy (TLB) (Sclavounos, Lee, DiPietro, Potenza, Caramuscio & Michele [35]).

The TLP design concept which was inspired by floater designs in the oil and gas industry is based on a floating platform highly constrained with vertical tethers balanced by an excessive buoyancy force upward and it has a large but mild compliance in translational modes of motion. The motion compliance often referred to as set-down, however, is not excessive because the buoyancy effect compensates and restores the system to its mean position. By virtue of the dynamic restoring mechanism, TLP naturally acts to convert the wave energy into a form of inertia and gravity which may help to absorb or mitigate the wave loads via its compliance and to diminish the loads on tethers and anchors in severe sea states. For most cases except for extremely shallow waters, the TLP design appears to be far more attractive than the TLB in terms of the practical operation with offshore wind turbines and the dynamic loading on tethers and anchors.

In a typical design process of TLP-based (or TLB-based) offshore floating wind turbines (Lee, Luypaert & Sclavounos [18]), it is of a great interest first to determine the design pretension on the tethers given the static payload from the wind turbine. A small design pretension is preferred to minimize the anchor

capacity needed on the seafloor, but it has to be large enough to take the dynamic loading from the wave and still maintain a tension on all tethers. The pretension, however, affects the required volume of the floating platform, which in turn, is proportional to the body disturbances in ambient waves, and thus the wave load as well. So an iterative method with an accurate wave load model is necessary to determine the minimum pretension on tethers, the required anchor capacity and the overall floating foundation cost.

Extreme wave environments are often observed on the ocean and they involve steep and large amplitude waves which create significant nonlinear contributions. In steep waves, ringing loads (Sclavounos [38] and Faltinsen, Newman & Vinje [11]) may occur and excite the floating structure, which in this work is a floating wind turbine. Since the natural frequency of the wind turbine tower falls around 1.7 rad/sec, this ringing load may have a substantial effect on the fatigue life of the tower, and thus lead to a system failure. Large amplitude waves cause extreme wave loads. The nonlinear hydrostatic force and nonlinear Froude-Krylov and diffraction forces are the greatest concern because they govern limits of the state of loads on tethers and anchors. For TLPs, the nonlinear extreme wave loads may lead to tether overload and tether slack which are undesirable for the foundation design. Nonlinear aspects of the hydrodynamic wave-body interaction have a significant impact on these ringing loads, extreme wave loads and the resultant system responses.

The biggest limitation of a frequency domain analysis based on the linear wave and linear dynamics theory is that the amplitudes of ambient wave and body motions have to be small compared to the ambient wavelength. With a linear

theory, the amplification of wave loads could be easily predicted by a standard numerical diffraction-radiation approach. However, the linearity assumptions on the wave and motion amplitudes prevent us from investigating many of the interesting and crucial hydrodynamic interactions between waves and bodies in severe seas as addressed earlier.

Time-domain based analysis is an essential design tool to better predict the nonlinear hydrodynamic wave load and dynamic responses in extreme ocean environments. A proper design evaluation of floating wind turbines requires an accurate simulation of nonlinear system responses, such as the maximum peak value for the pull-out load on the anchors on the sea floor, the maximum dynamic tension of the tethers on the fairleads and the maximum acceleration at the nacelle of the wind turbine. These values are the critical design performance indices of the primary cost of installation and operation of the offshore floating wind turbine. A nonlinear time-domain method is promising in terms of its computational modeling capability for those extreme events of large amplitude wave and motion.

## 1.2 Hydrodynamic Theory

Since Froude [10] and Krylov [15] first established a theoretical approach to the hydrodynamic analysis of a floating body's motion, there has been a tremendous advancement in computational fluid dynamics technology. It has occurred through advances in analytical modeling of fluid flow and numerical representation

technique. A strip theory was implemented for the study of wave loads on a body for short waves (Ogilvie & Tuck [29]), followed by a slender body theory which was applied for the wave loads on a slender ship (Newman [22]), but is potentially applicable to any floating body in general. A variety of numerical methods have been developed for understanding the relevant physics and accurate prediction of the interaction between fluids and bodies. Among all of these methods, the boundary element method based on the potential flow theory has become one of the most popular tools because of its efficiency, reliability and conciseness (Newman & Sclavounos [20] and Newman [23]).

Linear frequency-domain methods are very useful in many applications. Based on linear wave theory, an offshore structure's response to a random sea can be estimated by superposing the response to each wave frequency component in the wave spectrum (St. Denis & Pierson [8]). By virtue of linear wave theory, a reliability-index-based design method for a given sea spectrum provides an efficient and accurate analysis tool for hydrodynamic wave loads and system responses, and it captures most of the leading order effects in a mild sea condition.

In severe sea states or large-amplitude body motions, nonlinear effects are of great importance and interest. Examples of nonlinear effects include a nonlinear hydrostatic load by large-amplitude wave elevations, a nonlinear Froude-Krylov force and a ringing load by steep large-amplitude waves, and a nonlinear wave force by large-amplitude body motions. A nonlinear time-domain simulation is

necessary for the accurate prediction of those nonlinear wave-body interaction effects encountered with severe seas.

Due to the excessive computational cost involved with the complexity of fluid and body interaction, the three-dimensional fully nonlinear numerical simulations are often quite limited. Most of the recent developments in three-dimensional time-domain methods has resulted in several useful computational methods: boundary-discretization methods which are often called boundary element method (BEM), and volume-discretization methods. Although boundary-discretization methods are much more efficient than volume-discretization methods, the computational cost substantially increases to achieve the desired accuracy and thus limits the practical applications.

The boundary element methods can be formulated in two different ways: the Rankine panel method (RPM) (e.g. [24], [25] and [16]) or the transient free surface Green function method (e.g. [3] and [2]). Each method can fall into two categories: the body-nonlinear method or the fully nonlinear method. The body-nonlinear method linearizes the dynamic and kinematic free surface conditions about the mean surface which is the z=0 plane, but it takes the exact body boundary condition imposed on the instantaneous body surface under the water, not at the mean position of body surface. The fully nonlinear method however takes the nonlinear boundary conditions on both the free surface and the body wetted surface.

In the present study, the fully nonlinear problem is approached by a weak scatterer formulation based on the transient free-surface Green-function method ([19]). Assuming a small body induced wave disturbance compared to the incident wave disturbance, the free surface boundary conditions are linearized about the incident wave surface and the nonlinear body boundary condition is applied on the instantaneous underwater surface of the moving body. By applying this numerical treatment, the nonlinear wave-body interaction problem is simulated by the Green function method to obtain the fluid flow solution.

Based upon the solution for a wave-body interaction, the hydrodynamic pressure over the body surface is obtained by the Bernoulli equation. The direct integration of the pressure over the instantaneous underwater body surface gives a fully nonlinear hydrodynamic force and moment on the body at each time. Since the Bernoulli equation involves a partial temporal derivative and spatial derivative of the velocity potential over the body surface, however, a Bernoulli-based direct integration method often becomes challenging from a computational cost perspective.

A proper application of the momentum conservation principle leads to a new way of obtaining the nonlinear hydrodynamic force and moment on the body that does not involve the temporal and spatial derivatives of the potential over the body surface (Sclavounos [39]). Based on this newly developed theoretical model called Fluid Impulse Theory, the force on the body is expressed by two distinct components: the body surface impulse and the free surface impulse. An order of

magnitude analysis demonstrates that the contribution from the free surface impulse is negligible for mild wave steepnesses and body disturbances consistent with a weak-scatterer condition. This thesis focuses upon the weak-scatterer free-surface condition which leads to an accurate and efficient computational implementation: the total fluid force acting on a floating body is modeled by the time rate of change of the impulse of the velocity potential over the body surface only. It presents a new theoretical framework for analyzing the dominant nonlinear hydrodynamic forces on floating bodies which is potentially applicable in a wide range of problems in ocean engineering.

This thesis focuses on the new nonlinear wave load model in conjunction with the Green-function-based potential flow solver to address the nonlinear hydrodynamic wave loads and the resulting nonlinear responses of floating wind turbines in a highly efficient and robust manner in the time domain.

## 1.3 Overview

The rest of this thesis is organized as follows. Chapter 2 presents theoretical formulations: the boundary value problem for a hydrodynamic wave-body interaction, the treatment of nonlinear free-surface conditions in the context of a transient free-surface Green-function method, equations of motion of a floating wind turbine, a linearization of the equations of motion for a validation study, and a nonlinear wave load model based on Fluid Impulse Theory. Chapter 3 presents

numerical algorithms and simulation results: the numerical representation of the integral equation with a constant-strength source element, a numerical study of weak-scatterer condition followed by defining a simpler form of the Fluid Impulse Theory, a time domain simulation of a floating wind turbine for extreme wave events and a ringing load analysis by a power spectral density analysis for nonlinear wave loads in irregular seas. Chapter 4 discusses the results and contributions of this thesis and addresses the remaining outstanding issues and suggested future work.

# Chapter 2

# Theory

## 2.1 The Boundary Value Problem

Assuming incompressible, inviscid and irrotational fluid flow, the flow velocity can be described by the gradient of a velocity potential,

$$\vec{V}(x,y,z,t) = \nabla\varphi(x,y,z,t) \tag{2.1}$$

Applying the principle of conservation of momentum, the pressure in the fluid can be described by the flow kinematics following the Bernoulli equation

$$P - P_a = -\rho\left(\frac{\partial\varphi}{\partial t} + \frac{1}{2}\nabla\varphi\cdot\nabla\varphi + gz\right) \tag{2.2}$$

where $\rho$ is the density of the fluid, $g$ is the gravitational acceleration, and $P_a$ is the atmospheric pressure, which is the reference pressure. Since the atmospheric pressure is assumed to be constant which leads to vanishing forces after integration, our reference pressure $P_a$ will hereafter be assumed to be equal to zero.

By the principle of conservation of mass, the Laplace equation is satisfied over the entire fluid domain as

$$\nabla^2\varphi = 0$$

On the free surface the mathematical function $z-\zeta(x,y,z) \triangleq F(x,y,z,t)$ is always seen to be zero by the free-surface fluid particles, so the material derivative of $F$ has to be zero

$$\frac{DF}{Dt} = \left(\frac{\partial}{\partial t} + \vec{V}\cdot\nabla\right)F = 0 \text{ on } z = \zeta \tag{2.3}$$

which provides the kinematic free-surface condition:

$$\frac{\partial\zeta}{\partial t} + \frac{\partial\varphi}{\partial x}\frac{\partial\zeta}{\partial x} + \frac{\partial\varphi}{\partial y}\frac{\partial\zeta}{\partial y} = \frac{\partial\varphi}{\partial z} \text{ on } z = \zeta \tag{2.4}$$

Applying the Bernoulli equation we can obtain the dynamic free-surface condition:

$$\frac{\partial\varphi}{\partial t} + \frac{1}{2}\nabla\varphi\cdot\nabla\varphi + gz = 0 \text{ on } z = \zeta \tag{2.5}$$

On the body wetted surface, a no-flux boundary condition is required:

$$\frac{\partial\phi}{\partial n} = \frac{\partial V}{\partial n} \text{ on } S_B(t) \tag{2.6}$$

where $S_B(t)$ is the exact wetted surface of the body and $n$ is the unit vector normal to the body surface and pointing out of the fluid domain.

The total velocity potential can be represented by the following decompositions

$$\varphi = \varphi_I + \varphi_D$$
$$\varphi_D = \varphi_{DIF} + \varphi_{RAD}$$

where $\varphi_I$ is the ambient wave potential; $\varphi_D$ is the disturbance potential; $\varphi_{DIF}$ is the diffraction potential; $\varphi_{RAD}$ is the radiation potential.

The undisturbed incident wave is referred to as the ambient wave potential $\varphi_I$. Solving for the diffraction potential $\varphi_{DIF}$ on a motionless body given an ambient wave potential $\varphi_I$ will be referred to as the diffraction problem. Solving for the radiation potential due to a body's prescribed motion in any mode of motion in calm water will be referred to as the radiation problem. All of these velocity potentials are subject to the same boundary condition except for the body boundary condition.

By assuming a small steepness for the ambient surface wave, which is a reasonable assumption due to the high gravitational force, the following perturbation expansion for the velocity potential and free-surface elevation can be postulated

$$\varphi = \varphi_1 + \varphi_2 + \varphi_3 + \ldots$$
$$\zeta = \zeta_1 + \zeta_2 + \zeta_3 + \ldots$$

where

$$\varphi_1 = O(\delta); \varphi_2 = O(\delta^2); \varphi_3 = O(\delta^3) \ldots$$
$$\zeta_1 = O(\delta); \zeta_2 = O(\delta^2); \zeta_3 = O(\delta^3) \ldots$$

The fully nonlinear free-surface conditions may be expanded and reformulated by taking terms of up to first order, which lead us to the linearized kinematic and dynamic free-surface conditions:

$$\frac{\partial \zeta_1}{\partial t} = \frac{\partial \varphi_1}{\partial z} \text{ on } z = 0 \tag{2.7}$$

$$\zeta_1 = -\frac{1}{g}\frac{\partial \varphi_1}{\partial t} \text{ on } z = 0 \tag{2.8}$$

By differentiating the dynamic free-surface condition with respect to time on the plane of $z$=0 and substituting into the kinematic free-surface condition, a single boundary condition for the free-surface is obtained as follows:

$$\frac{\partial^2 \varphi}{\partial t^2} + g\frac{\partial \varphi}{\partial z} = 0 \text{ on } z = 0. \tag{2.9}$$

A no-flux boundary condition is required on the seafloor with a finite water depth $H$:

$$\frac{\partial \phi}{\partial n} = 0 \text{ on } z = -H \tag{2.10}$$

With the linearized free-surface boundary conditions presented above and applying separation of variables, the solution of the wave velocity potential and the dynamic pressure in a plane progressive wave take the form:

$$\begin{aligned} \varphi_I(x,z,t) &= \mathrm{Re}\left\{ \frac{igA}{w} \frac{\cosh k(z+H)}{\cosh kH} e^{-ikx+iwt} \right\} \\ P_I(x,z,t) &= -\rho \frac{\partial \varphi_1(x,z,t)}{\partial t} = \mathrm{Re}\left\{ \rho g A \frac{\cosh k(z+H)}{\cosh kH} e^{-ikx+iwt} \right\} \end{aligned} \tag{2.11}$$

where $A$ is the wave amplitude; $w$ is the wave frequency; $k$ is the wave number; $H$ is the water depth.

Upon substitution in the dynamic free-surface condition, the linear free-surface elevation takes the form:

$$\zeta(x,t) = -\frac{1}{g} \frac{\partial \varphi}{\partial t}\bigg|_{z=0} = \mathrm{Re}\left\{ A e^{-ikx+iwt} \right\} \tag{2.12}$$

Upon substitution of the velocity potential Eq. (2-2) in the free-surface condition Eq. (2-1), the relationship between $w$, $k$ and $H$ is obtained as follows:

$$w^2 = gk \tanh kH \tag{2.13}$$

This is the wave dispersion relation, which determines a unique wave frequency $w$ for given values of a wave number $k$ and water depth $H$, or the vice versa.

For deep water ($kH >> 1$), the wave velocity potential and the dispersion relation simply take the form:

$$\varphi_I(x,z,t) = \mathrm{Re}\left\{\frac{igA}{w} e^{-ikx+iwt}\right\} \text{ for } kH >> 1 \tag{2.14}$$
$$w^2 = gk$$

## 2.2 A Source-only Formulation

The boundary value problem described above may be represented by an integral equation based on a transient free-surface Green-function. It can be expressed as derived in Wehausen and Laitone [42] by

$$G(\vec{x};\vec{\xi},t) = G^{(0)}(\vec{x};\vec{\xi}) + H(\vec{x};\vec{\xi},t-\tau), \tag{2.15}$$

where

$$
\begin{aligned}
&G^{(0)}(\bar{x};\bar{\xi}) = -\frac{1}{4\pi}\left(\frac{1}{r}-\frac{1}{r'}\right) \\
&H(\bar{x};\bar{\xi},t-\tau) = -\frac{1}{2\pi}\int_0^\infty \left(1-\cos\left[\sqrt{gk}(t-\tau)\right]\right)\exp(kZ)J_0(kR)dk \\
&r = \sqrt{(x-\xi)^2+(y-\eta)^2+(z-\varsigma)^2} \\
&r' = \sqrt{(x-\xi)^2+(y-\eta)^2+(z+\varsigma)^2} \\
&Z = (z+\varsigma) \\
&R = \sqrt{(x-\xi)^2+(y-\eta)^2}
\end{aligned}
\qquad (2.16)
$$

The impulsive Green function component $G^{(0)}(\bar{x};\bar{\xi})$ imposes the $\varphi = 0$ condition on the $z$ =0 plane which satisfies the linearized free-surface condition for the frequency $w$ that goes to infinity. The impulsive potential generates a Cauchy-Poisson type wave system which is represented by $H(\bar{x};\bar{\xi},t-\tau)$. The Cauchy-Poisson wave analysis is an important mathematical theory for the treatment of initial-value problems and is applied in the present study to describe the waves on the surface of a fluid caused by a given initial perturbation, which is represented by the impulsive potential component as above. This is the key concept in the present hydrodynamics model for the body wave disturbance over time.

A wave source formulation will be used in the present study to represent the disturbance potentials which are assumed to satisfy the proper body boundary conditions and the free-surface condition on z=0. The strength of the wave source at source point $\bar{\xi}$ at time $t$ is now the primary unknown.

Using Green's second theorem,

$$\varphi(\vec{x},t) = \iint_{S_B(t)} \sigma(\vec{\xi},t) G^{(0)}(\vec{x};\vec{\xi}) d\vec{\xi} + \int_0^t d\tau \iint_{S_B(\tau)} \sigma(\vec{\xi},\tau) H_t(\vec{x};\vec{\xi},t-\tau) d\vec{\xi}$$
$$\text{where, } H_t(\vec{x};\vec{\xi},t-\tau) = -\frac{1}{2\pi}\int_0^\infty \sqrt{gk}\sin\left[\sqrt{gk}(t-\tau)\right]\exp(kZ)J_0(kR)dk \tag{2.17}$$

The second term in the right hand side of Eq. (2.17) represents the transient wave part of the Green function, the so-called memory effect, which contributes a velocity potential component at time $t$ arising from the entire time history of the source strength distribution on the body surface. The normal derivative of the velocity potential over the body surface is the key property that is imposed into the body boundary condition formulation.

Applying the body boundary condition $V_n(\vec{x},t) = \vec{n}_{\vec{x}} \cdot \nabla_{\vec{x}} \varphi(\vec{x},t)$ by taking a derivative in a normal direction with respect to the surface at $\vec{x}$,

$$V_n(\vec{x},t) = \vec{n}_{\vec{x}} \cdot \iint_{S_B(t)} \sigma(\vec{\xi},t) \nabla_{\vec{x}} G^{(0)}(\vec{x};\vec{\xi}) d\vec{\xi} + \vec{n}_{\vec{x}} \cdot \int_0^t d\tau \iint_{S_B(\tau)} \sigma(\vec{\xi},\tau) \nabla_{\vec{x}} H_t(\vec{x};\vec{\xi},t-\tau) d\vec{\xi} \tag{2.18}$$

Thus the impulsive part can now be related to the memory part and the impulsive body boundary condition as follows.

$$\vec{n}_{\vec{x}} \cdot \iint_{S_B(t)} \sigma(\vec{\xi},t) \nabla_{\vec{x}} G^{(0)}(\vec{x};\vec{\xi}) d\vec{\xi} = -\vec{n}_{\vec{x}} \cdot \int_0^t d\tau \iint_{S_B(\tau)} \sigma(\vec{\xi},\tau) \nabla_{\vec{x}} H_t(\vec{x};\vec{\xi},t-\tau) d\vec{\xi} + V_n(\vec{x},t) \tag{2.19}$$

The impulsive potential generates a Cauchy-Poisson type wave system which is represented by $H(\bar{x};\bar{\xi},t-\tau)$ above. The Green function satisfies the free-surface condition and the Laplace equation in the rest of the fluid domain. An integral equation can be generated in terms of the Green function over the body boundary over time.

By taking the normal derivative,

$$\iint_{S_B(t)} \sigma(\bar{\xi},t)\frac{\partial}{\partial n_{\bar{x}}}G^{(0)}(\bar{x};\bar{\xi})d\bar{\xi} = -\int_0^t d\tau \iint_{S_B(\tau)} \sigma(\bar{\xi},\tau)\frac{\partial}{\partial n_{\bar{x}}}H_t(\bar{x};\bar{\xi},t-\tau)d\bar{\xi} + V_n(\bar{x},t) \tag{2.20}$$

This leads to the general source integral equation for the body disturbance velocity potential over time. In the three dimensional wave-body hydrodynamic interaction problem, the computation of the memory contribution becomes highly challenging. There exist computation methods which carry out an efficient memory component computation which is crucial for implementation in the design process.

Assuming efficient methods for memory component computation have been used, the resulting expression in a matrix notation is as follows.

$$B_{ij}\,\sigma(\bar{x}_j,t) = -K_1(\bar{x}_j,t) + V_n(\bar{x}_j,t) \tag{2.21}$$

$$\textit{where, } K_1(\bar{x}_j,t) \triangleq \int_0^t d\tau \iint_{S_B(\tau)} \sigma(\bar{\xi},\tau)\frac{\partial}{\partial n_{\bar{x}}}H_t(\bar{x};\bar{\xi},t-\tau)d\bar{\xi}$$

$B_{ij}$ is the influence coefficient matrix which does not depend on time in the present study. At every time step t the body boundary condition $V_n(\vec{x}_j,t)$ is provided by the body's forced oscillation or resultant dynamic response, and the memory component $K_1(\vec{x}_j,t)$ is evaluated carefully which may require an efficient treatment of principal value integrals. Numerical methods for efficient evaluation of this memory component will be presented in detail in the next chapter. The strength of source $\sigma(\vec{x}_j,t)$ is determined from the solution of the linear system.

$$\{\sigma(t)\} = [B]^{-1}\{-K_1(t) + V_n(t)\} \tag{2.22}$$

## 2.3 The Transient Wave Part of the Green Function

The body boundary condition enforced using Green's second theorem is as follows.

$$\iint_{S_B(t)} \sigma(\vec{\xi},t)\frac{\partial}{\partial n_{\vec{x}}}G^{(0)}(\vec{x};\vec{\xi})d\vec{\xi} = -\int_0^t d\tau \iint_{S_B(\tau)} \sigma(\vec{\xi},\tau)\frac{\partial}{\partial n_{\vec{x}}}H_t(\vec{x};\vec{\xi},t-\tau)d\vec{\xi} + V_n(\vec{x},t) \tag{2.23}$$

The wave part of the Green function is:

$$H_t(\vec{x};\vec{\xi},t-\tau) = -\frac{1}{2\pi}\int_0^\infty \sqrt{gk}\sin\left[\sqrt{gk}(t-\tau)\right]\exp(kZ)J_0(kR)dk$$

$$\text{where, } r = \sqrt{(x-\xi)^2+(y-\eta)^2+(z-\varsigma)^2}$$

$$r' = \sqrt{(x-\xi)^2+(y-\eta)^2+(z+\varsigma)^2} \qquad (2.24)$$

$$Z = (z+\varsigma)$$

$$R = \sqrt{(x-\xi)^2+(y-\eta)^2}$$

As revealed by the work of Clement [7], the wave part of the Green function $H_t(\vec{x};\vec{\xi},t-\tau)$ can be evaluated by solving an ordinary differential equation as follows.

$H_t(\vec{x};\vec{\xi},t-\tau)$ can be rewritten as:

$$F(\bar{r},\bar{Z};t-\tau) = -\frac{1}{2\pi}\int_0^\infty \sqrt{gk}\sin[\sqrt{gk}(t-\tau)]e^{gk(\bar{z}+\bar{z}')}J_o(k\bar{R})dk \qquad (2.25)$$

Variable changes are introduced as follows.

$$\begin{aligned} K &= gk, \\ R &= \frac{\bar{R}}{g}, \\ z &= \frac{\bar{z}}{g}; z' = \frac{\bar{z}'}{g}, \\ r &= \frac{\bar{r}}{g}; r_1 = \frac{\bar{r}_1}{g}, \\ F(r,Z;t-\tau) &= g\bar{F}(\bar{r},\bar{Z};t-\tau), \end{aligned} \qquad (2.26)$$

This leads to a new equation:

$$F(r,Z;t-\tau)=-\frac{1}{2\pi}\int_0^\infty \sqrt{K}\sin[\sqrt{K}(t-\tau)]e^{K(z+z')}J_o(KR)dK \tag{2.27}$$

By a variable change ( $Kr_1 \to \lambda$ ) above, it can be expressed as a function of two new real variables $(\mu,\tau)$:

$$F(r,Z;t-\tau)=-\frac{1}{2\pi}r_1^{-3/2}\tilde{F}(\mu,\tau) \tag{2.28}$$

where

$$\tilde{F}(\mu,\tau)=\int_0^\infty J_o(\lambda\sqrt{1-\mu^2})e^{-\lambda\mu}\sqrt{\lambda}\sin(\sqrt{\lambda}\tau)d\lambda$$
$$\mu=-Z/r_1;\ \tau=(t-\tau)/\sqrt{r_1}$$

$\tilde{F}(\mu,\tau)$ satisfies the following fourth-order differential equation:

$$\tilde{F}^{(4)}+\mu\tau\tilde{F}^{(3)}+(\frac{1}{4}\tau^2+4\mu)\tilde{F}^{(2)}+\frac{7}{4}\tau\tilde{F}^{(1)}+\frac{9}{4}\tilde{F}=0 \tag{2.29}$$

with the initial conditions

$$\tilde{F}^{(2k)}(\mu,0)=0,\tilde{F}^{(2k+1)}(\mu,0)=(-1)^k(k+1)!P_{k+1}(\mu);$$
$$(k=0,1,...)$$

where $\tilde{F}^{(k)}$ denotes the $k^{\text{th}}$-order differentiation of $\tilde{F}$ with respect to $\tau$.

The derivatives of the Green function, $\frac{\partial F}{\partial x}$ and $\frac{\partial F}{\partial y}$, can be computed as follows:

$$\begin{aligned}\frac{\partial F}{\partial x} &= \frac{x-x'}{r}F_r \\ \frac{\partial F}{\partial y} &= \frac{y-y'}{r}F_r \\ \frac{\partial F}{\partial z} &= \frac{z-z'}{r}F_r\end{aligned} \tag{2.30}$$

where

$$F_r(r,Z;t) = \frac{1}{2\pi} r_1^{-5/2}\tilde{K}(\mu,\tau)$$

$\tilde{K}(\mu,\tau)$ satisfies the following fourth-order differential equation:

$$\tilde{K}^{(4)} + \mu\tau\tilde{K}^{(3)} + (\frac{1}{4}\tau^2 + 6\mu)\tilde{K}^{(2)} + \frac{11}{4}\tau\tilde{K}^{(1)} + \frac{21}{4}\tilde{K} = 0 \tag{2.31}$$

with the initial conditions

$$\tilde{K}^{(2k)}(\mu,0) = 0, \tilde{K}^{(2k+1)}(\mu,0) = (-1)^k(k+1)!\sqrt{1-\mu^2}\,\frac{d}{d\mu}P_{k+2}(\mu);$$

$$(k = 0,1,...)$$

The equation for $\tilde{F}(\mu,\tau)$ and $\tilde{K}(\mu,\tau)$ can be expressed and unified in a general form as follows.

$$K_F^{(4)} + \mu\tau K_F^{(3)} + (\frac{1}{4}\tau^2 + A\mu)K_F^{(2)} + B\tau K_F^{(1)} + CK_F = 0$$

$$\text{where, } A = 4;\ B = \frac{7}{4};\ C = \frac{9}{4} \text{ for } K_F = \tilde{F} \qquad (2.32)$$

$$A = 6;\ B = \frac{11}{4};\ C = \frac{21}{4} \text{ for } K_F = \tilde{K}$$

Instead of solving it with a Runge-Kutta numerical scheme, a Taylor series expansion method is applied to achieve an analytical solution for low computational cost. Firstly $\tilde{K}(\mu,\tau)$ is assumed to be represented in a polynomial form as follows.

$$K_F(\tau) = a_o + \sum_{n=1}^{\infty} a_n(\tau - \tau_1)^n \qquad (2.33)$$

Based on the recent work of Chuang [6], the coefficients $a_n$ can be obtained in closed form solution as shown below.

$$a_4 = -\frac{1}{24\kappa_1}(6\kappa_3 a_3 + 2\kappa_6 a_2 + \kappa_8 a_1 + \kappa_9 a_o)$$

$$a_{n+4} = \frac{1}{y_{n+4}}(y_{n+3}a_{n+3} + y_{n+2}a_{n+2} + y_{n+1}a_{n+1} + y_n a_n) \quad \text{for } n = 1,2,3,... \qquad (2.34)$$

where

$$
\begin{aligned}
y_{n+4} &= \kappa_1(n+4)(n+3)(n+2)(n+1) \\
y_{n+3} &= \kappa_3(n+3)(n+2)(n+1) \\
y_{n+2} &= \kappa_2(n+2)(n+1)n + \kappa_6(n+2)(n+1) \\
y_{n+1} &= \kappa_5(n+1)n + \kappa_8(n+1) \\
y_n &= \kappa_4 n(n-1) + \kappa_7 n + \kappa_9
\end{aligned}
$$

Once those coefficients are obtained, $\tilde{F}(\mu,\tau)$ and $\tilde{K}(\mu,\tau)$ can be computed and therefore the wave part of the Green function can be evaluated very efficiently from the computational perspective.

The number of terms needed in the Taylor series expansion should be determined carefully. A convergence property has been tested and plotted below. The minimum number of terms needed for convergence will depend on the temporal and spatial condition denoted here as $t-\tau$ and $\mu$ respectively. The wave part of Green function $H_t(P,Q,t-\tau)$ is obtained from $\tilde{F}(\mu,\tau)$ which is computed by a Taylor series expansion solution $a_1, a_2, ...., a_n, ....$ as presented above.

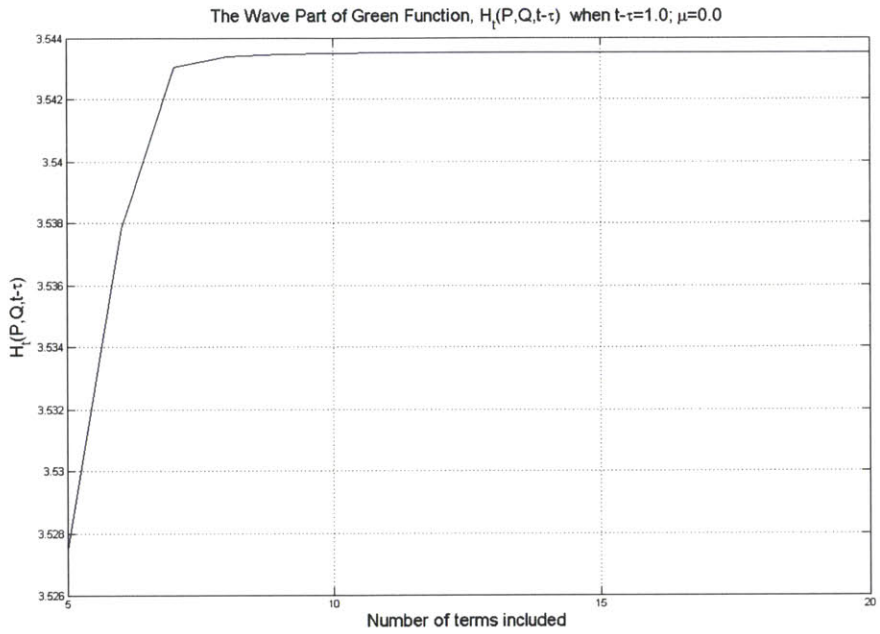


Figure 2-1: The wave part of Green function $H_t(P,Q,t-\tau)$ when $t-\tau=1.0;\ \mu=0.0$

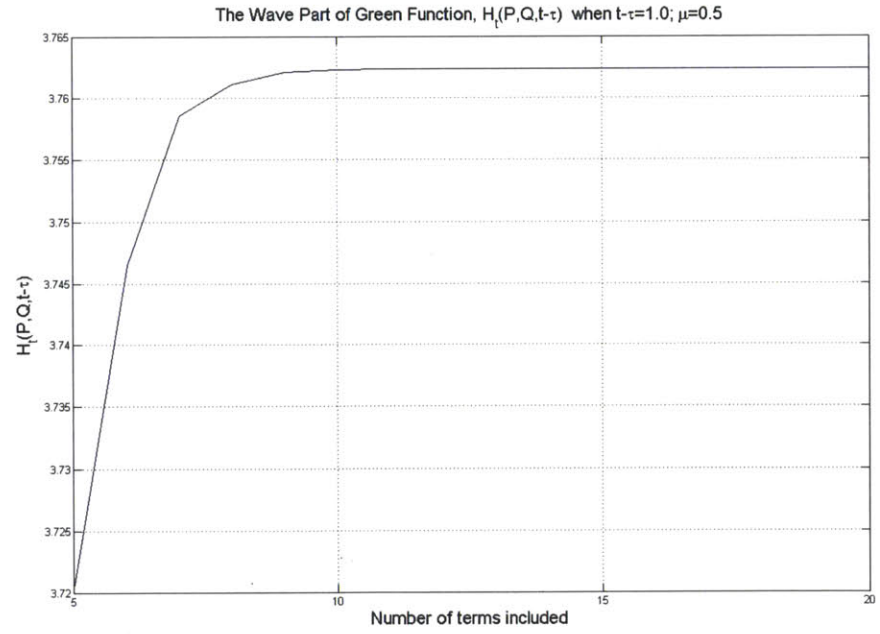


Figure 2-2: The wave part of Green function $H_t(P,Q,t-\tau)$ when $t-\tau=1.0;\ \mu=0.5$

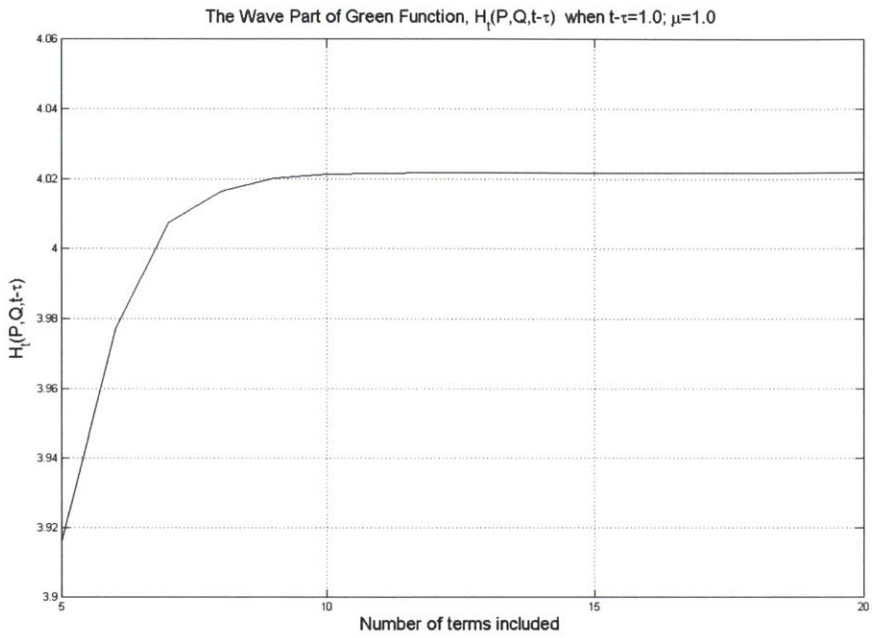


Figure 2-3: The wave part of Green function $H_t(P,Q,t-\tau)$ when $t-\tau=1.0;\ \mu=1.0$

The minimum number of terms needed in the Taylor series expansion depends on $\mu$ and $t-\tau$. For $\mu$ and $t-\tau$ ranging from 0.0 to 1.0 and 0.0 to 15.0 respectively, it has been proven that the number of Taylor expansion terms has to be larger than 50 with a tolerance of $10^{-6}$ between successive terms in the partial sum. The smaller number of required terms contributes to a higher computational efficiency and therefore I will only take the first 50 terms in the computation of $\tilde{F}(\mu,\tau)$ at every time $\tau$.

The time step needs to be carefully chosen and be sufficiently small. Based on convergence tests over different values of $\mu$ and $t-\tau$, the time step has to be smaller than 0.001 sec which satisfies a convergence tolerance of 0.1%. With both conditions fully satisfied as above in terms of the number of Taylor series coefficients and the time step, the resultant Green function has been computed and plotted as follows.

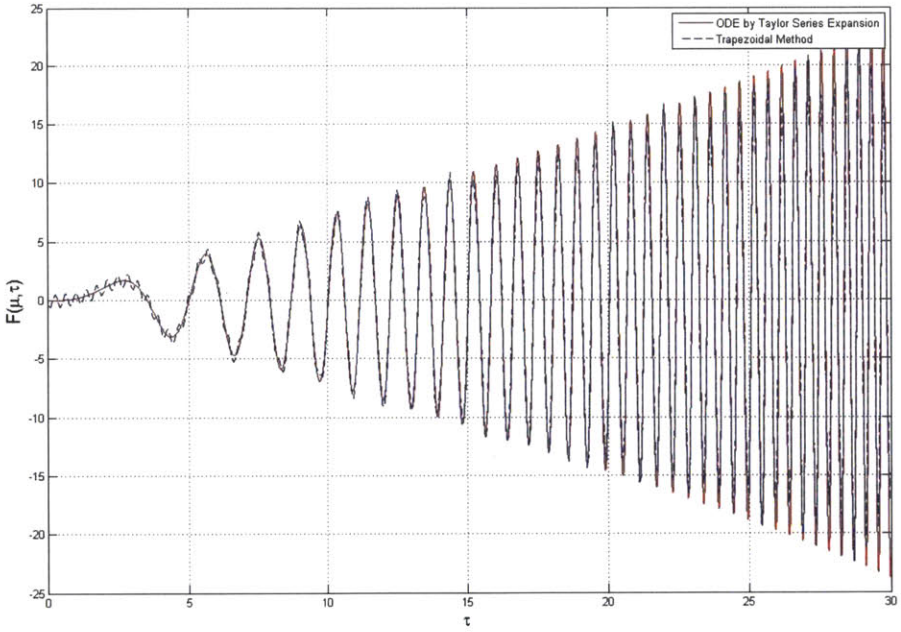


Figure 2-4: The Green function $\tilde{F}(\mu,\tau)$ when $\mu$=0.0

When the field point and source point are both located on the free-surface, which means $\mu$ becomes zero, the time step size in $\tau$ needs to be decreased down

to a sufficiently small value in order to provide an accurate solution by the present method based on Taylor series expansion.

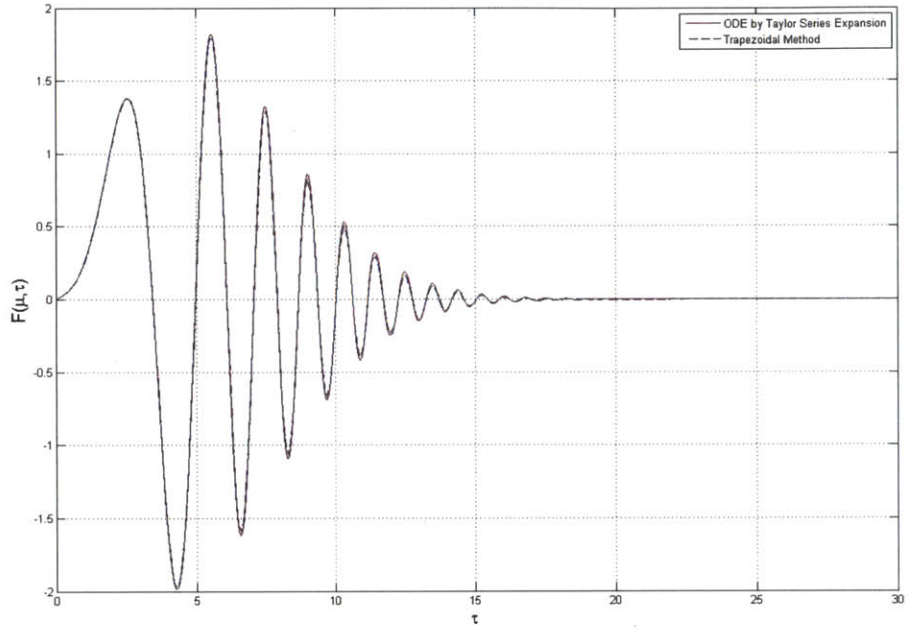


Figure 2-5: The Green function $\tilde{F}(\mu,\tau)$ when $\mu$=0.1

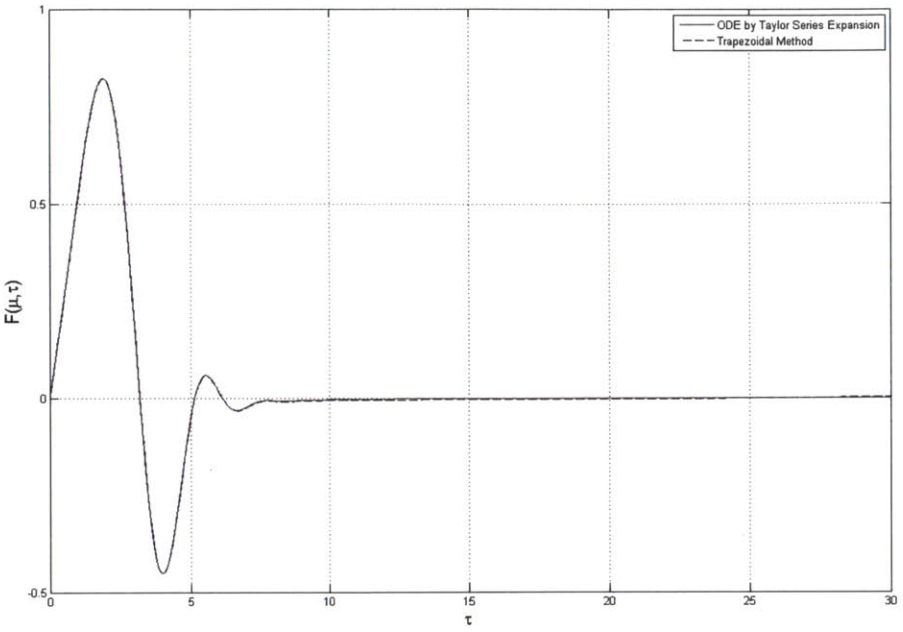


Figure 2-6: The Green function $\tilde{F}(\mu,\tau)$ when $\mu$=0.5

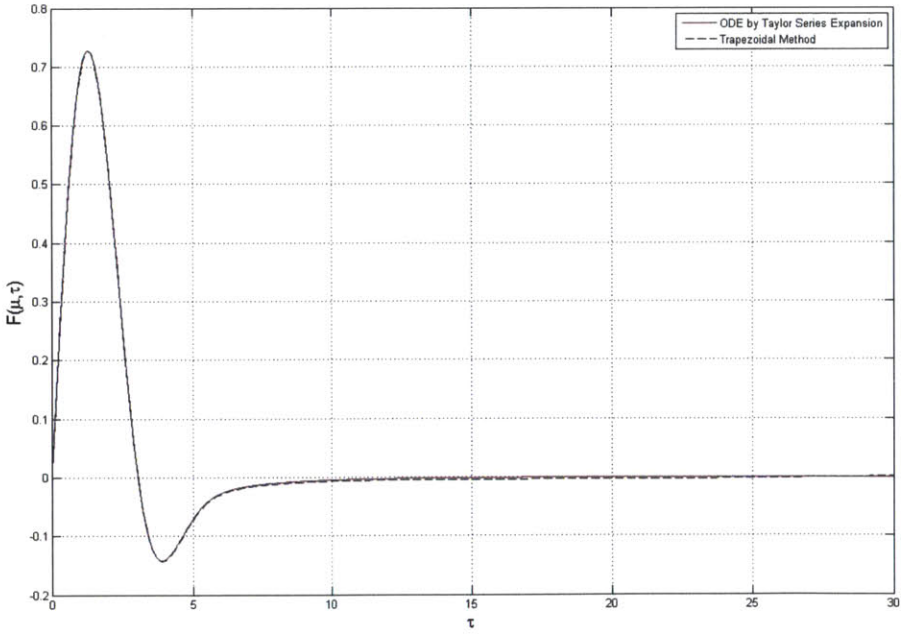


Figure 2-7: The Green function $\tilde{F}(\mu,\tau)$ when $\mu$=0.9

$\tilde{F}(\mu,\tau)$ needs to be computed for all possible sets of $\mu$ and $t-\tau$ in the spatial and temporal domain that can possibly occur during the computation of the memory effect. In the computation of the memory effect Kernel at every time step t, it will just take the proper value from this pre-computed $\tilde{F}(\mu,\tau)$ based on the spatial and temporal condition $\mu$ and $t-\tau$ that accounts for a pair points P and Q. This will enhance the computational efficiency significantly and therefore the time domain evaluation of hydrodynamic interactions between surface waves and the floating body can be simulated efficiently and effectively over various wave conditions and body shapes.

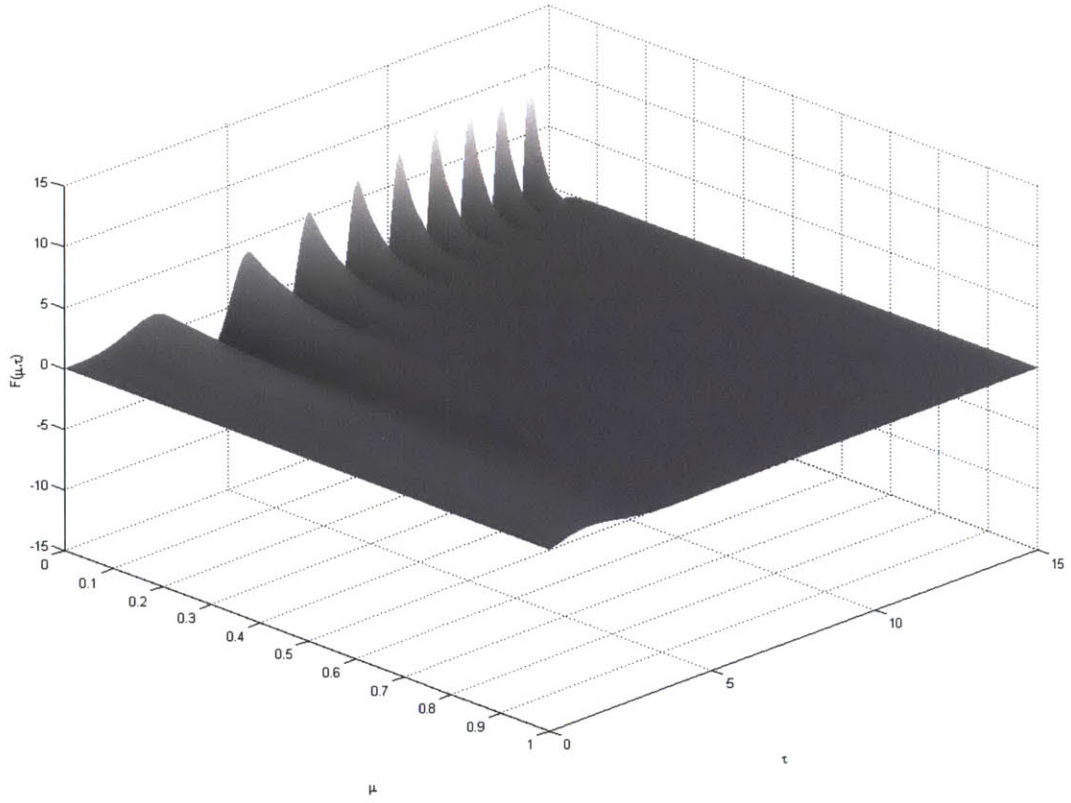


Figure 2-8: The Green function $\tilde{F}(\mu,\tau)$ over the entire domain of natural variables $(\mu,\tau)$.

These tabulated $\tilde{F}(\mu,\tau)$ values will be used in subsequent time domain simulations which need to evaluate the wave part of the Green function over time called the wave memory effect. By the way this $\tilde{F}(\mu,\tau)$ is well matched up with the results presented at Clement [7].

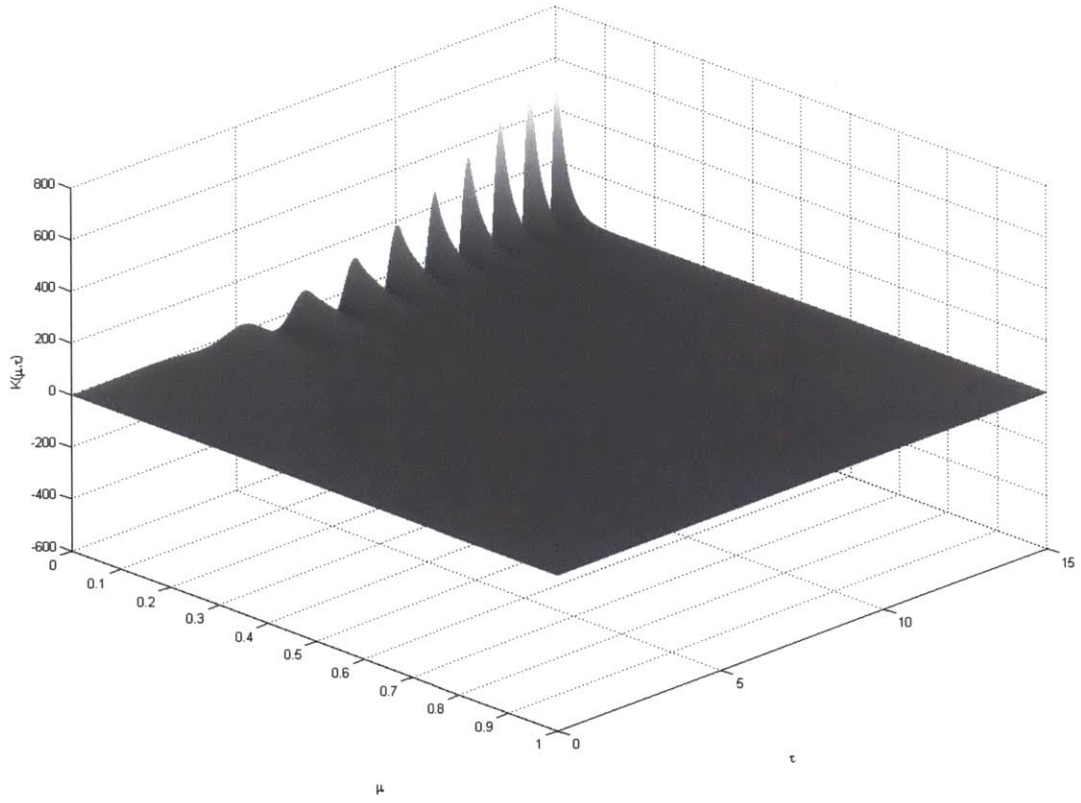


Figure 2-9: The Green function derivative $\tilde{K}(\mu,\tau)$ over the entire domain of natural variables ( $\mu,\tau$ ).

## 2.4 The Treatment of Nonlinear Free-Surface Condition

For a large-amplitude incident wave, the kinematic and dynamic free-surface conditions are highly nonlinear and imposed on the exact wave surface elevation which in the time domain becomes an unknown variable, the result of a fully nonlinear wave-body hydrodynamic interaction. The linear wave theory loses its accuracy significantly as the wave steepness increases. A highly elaborate computational effort is required to solve for this fully nonlinear incident wave potential which involves a systematic computation of velocity potential components of second and third or higher orders.

The present work adopts the Weak-Scatterer hypothesis which assumes that the body wave disturbances propagate on the step incident wave surface profile and are small. Therefore the incident wave free-surface elevation over space and time may be decoupled from the body disturbances even for large-amplitude body motions and large-amplitude ambient waves. The main idea was first proposed by Pawlowski [31]. It is quite justifiable considering that offshore structures are in most cases designed to be slender and therefore the wave surface disturbance they induce is relatively small compared to the incident wave surface elevation.

By virtue of this Weak-Scatterer hypothesis, the wave disturbances may be linearized about the incident wave surface which is known a priori. By implementing this novel idea that enforces the free-surface boundary conditions about the incident wave surface, the fully nonlinear problem can be approached in an efficient manner by using the transient free-surface Green-function method.

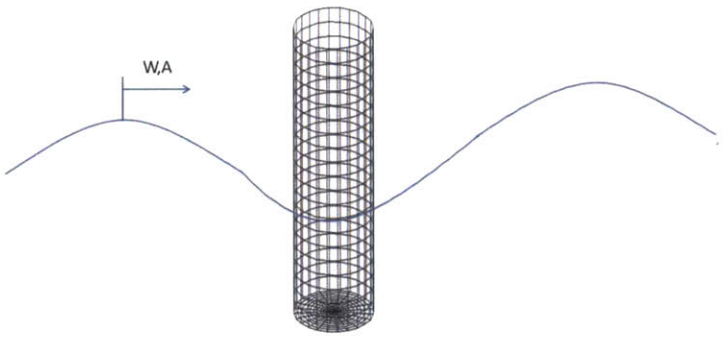


Master domain

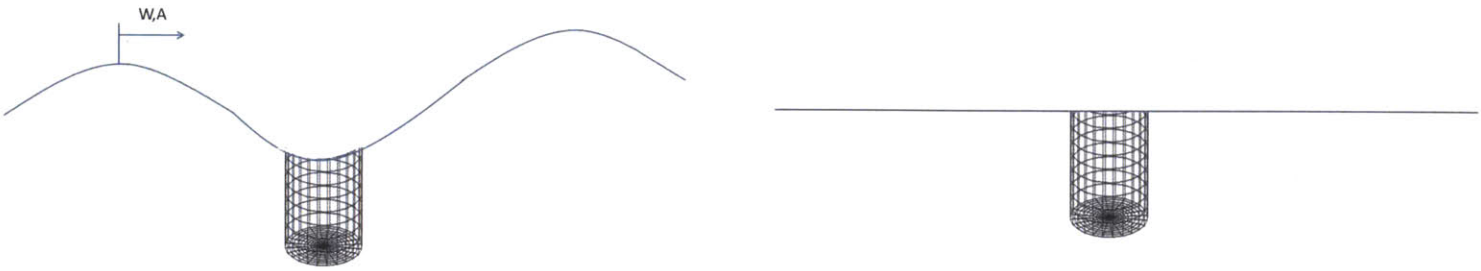


Physical domain Stretched computational domain

Figure 2-10: The treatment of nonlinear free-surface condition by the 3D transient free-surface Green-function method

The perturbation expansion for the velocity potential and free-surface elevation can be postulated as follows.

$$\varphi = \varphi_1 + \varphi_2 + \varphi_3 + \ldots$$
$$\zeta = \zeta_1 + \zeta_2 + \zeta_3 + \ldots$$

Where,

$$\varphi_1 > \varphi_2 > \varphi_3 > \ldots$$
$$\zeta_1 > \zeta_2 > \zeta_3 > \ldots$$

Assuming that disturbance flow quantities are small compared to the incident potential and free-surface elevation, the following perturbation expansion is postulated.

$$\varphi = \varphi_I + \varphi_D$$
$$\zeta = \zeta_I + \zeta_D$$

$$\varphi_I \sim o(\delta) \quad ,$$
$$\zeta_I \sim o(\delta)$$
$$\varphi_D \sim o(\varepsilon)$$
$$\zeta_D \sim o(\varepsilon)$$

where $\varphi_I$ is the incident wave potential; $\zeta_I$ is the incident wave elevation from z=0 plane; $\varphi_D$ is the linearized disturbance wave potential; $\zeta_D$ is the linearized disturbance surface elevation from the incident free-surface elevation.

In the present work, the incident wave potential and free-surface elevation shown above are assumed to be large and fully nonlinear. The disturbance potential and free-surface elevation can be properly evaluated by solving a linear boundary value problem defined below.

The linear dynamic and kinematic boundary conditions for the disturbance potential and free-surface elevation take the form,

$$\begin{aligned} &\frac{\partial \varphi_D}{\partial t} + g\zeta_D = 0 \\ &\frac{\partial \zeta_D}{\partial t} - \frac{\partial \varphi_D}{\partial z} = 0 \end{aligned} \quad \text{on } S_F^I(t), \tag{2.35}$$

where $S_F^I(t)$ is the incident ambient wave free-surface.

The linear body boundary condition imposes a normal velocity given by

$$\frac{\partial \varphi}{\partial n} = \vec{V} \cdot \vec{n} \text{ on } S_B^I(t),$$

where

$S_B^I(t)$ is the instantaneous body surface under the ambient wave

$\varphi$ is the total velocity potential, $\varphi_I + \varphi_D$

A computer code has been developed for the evaluation of the disturbance potential and free-surface elevation that satisfy the boundary conditions properly on the surface of a large-amplitude incident wave.

## - Linear Waves and Linear Motions

Free-surface boundary conditions are imposed on the mean surface at z=0, and the body boundary condition is imposed on the mean position of the body at x=0. The underwater body geometry remains uniform over time and the impulsive Green-function coefficients need to be evaluated only once and may be reused at every time step. However, the transient Green-function coefficients, the so-called memory contribution, have to be evaluated for $\tau$ at every time step.

## - Large-Amplitude Waves and Large-Amplitude Motions

In the case of large-amplitude waves and large-amplitude motions, free-surface boundary conditions are imposed on the ambient incident wave surface at $z=\zeta(t)$, and the body boundary condition is imposed on the exact position of the body at $x=\xi_1(t)$. In addition, since the underwater body geometry varies over time, the impulsive Green-function coefficients, which are often called 'Influence Coefficients', have to be reevaluated at every single time step. The transient Green-function coefficients now have to be evaluated in a convolution sense for different $\tau$'s at every time step because the combination of spatial and temporal variables $\mu$ and $\tau$ varies in time which is the primary source of the computational cost.

## 2.5 Tension Leg Platform Equations of Motion

- Coordinate system: Earth-fixed coordinate system (X-Y-Z) as shown at Figure 2-12
- Unknown variables:
    - Motion in $\theta(t)$, which is an inclination angle of the vertical tether as shown at Figure 2-12
    - Tensions of line, $T_1^*(t)$ and $T_2(t)$
- Number of equations:
    - Two linear momentum conservations in X(surge) and Z(heave)
    - One angular momentum conservation in Y(pitch)
- Assumptions:
    - Zero motion in pitch (Line tensions become the unknown variables instead)
    - Unidirectional incident wave propagating in the X-axis
    - Deep water

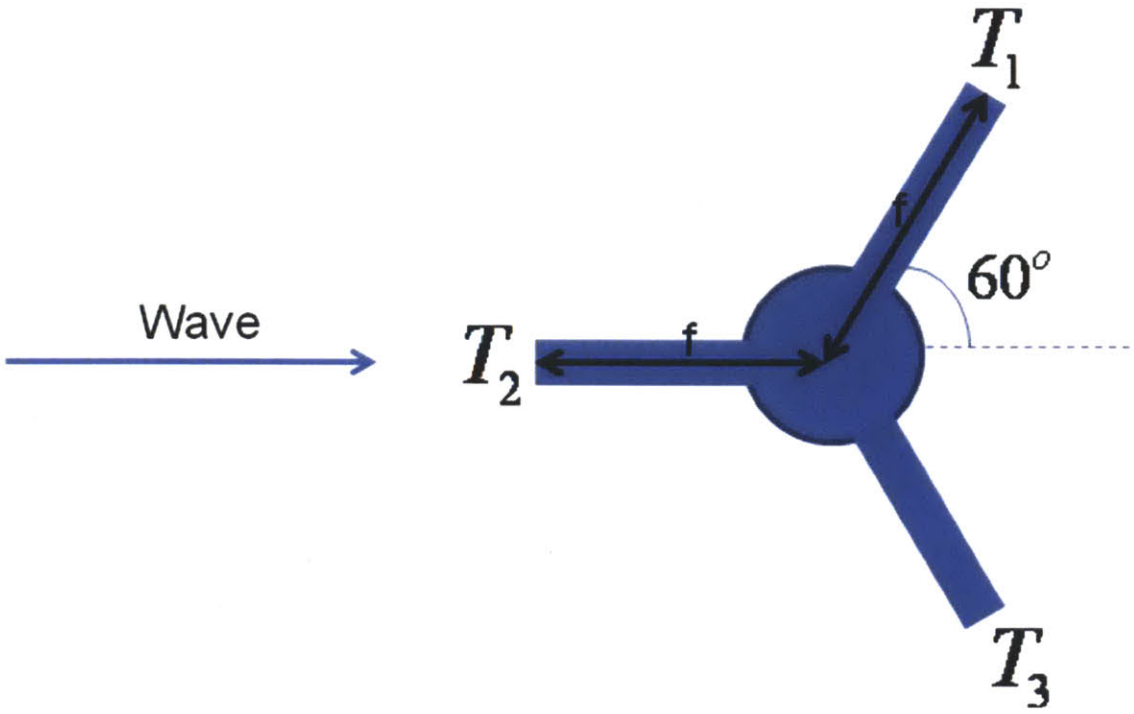


Figure 2-11: Top view of three legs for the vertical tether

$$T_1(t) = T_3(t)$$
$$T_1^*(t) \triangleq T_1(t) + T_3(t)$$

The floating wind turbine is supported by a Tension Leg Platform (TLP) floating system that has three legs and pre-tensioned vertical tethers. Since the incident wave is assumed to be unidirectional along the X-axis, the two leeward-side tensions $T_1(t)$ and $T_3(t)$ in the three-leg mooring system shown above have to be equal and therefore those two tension variables are modeled by a single lumped tension $T_1^*(t)$ in the following formulation of the equations of motion.

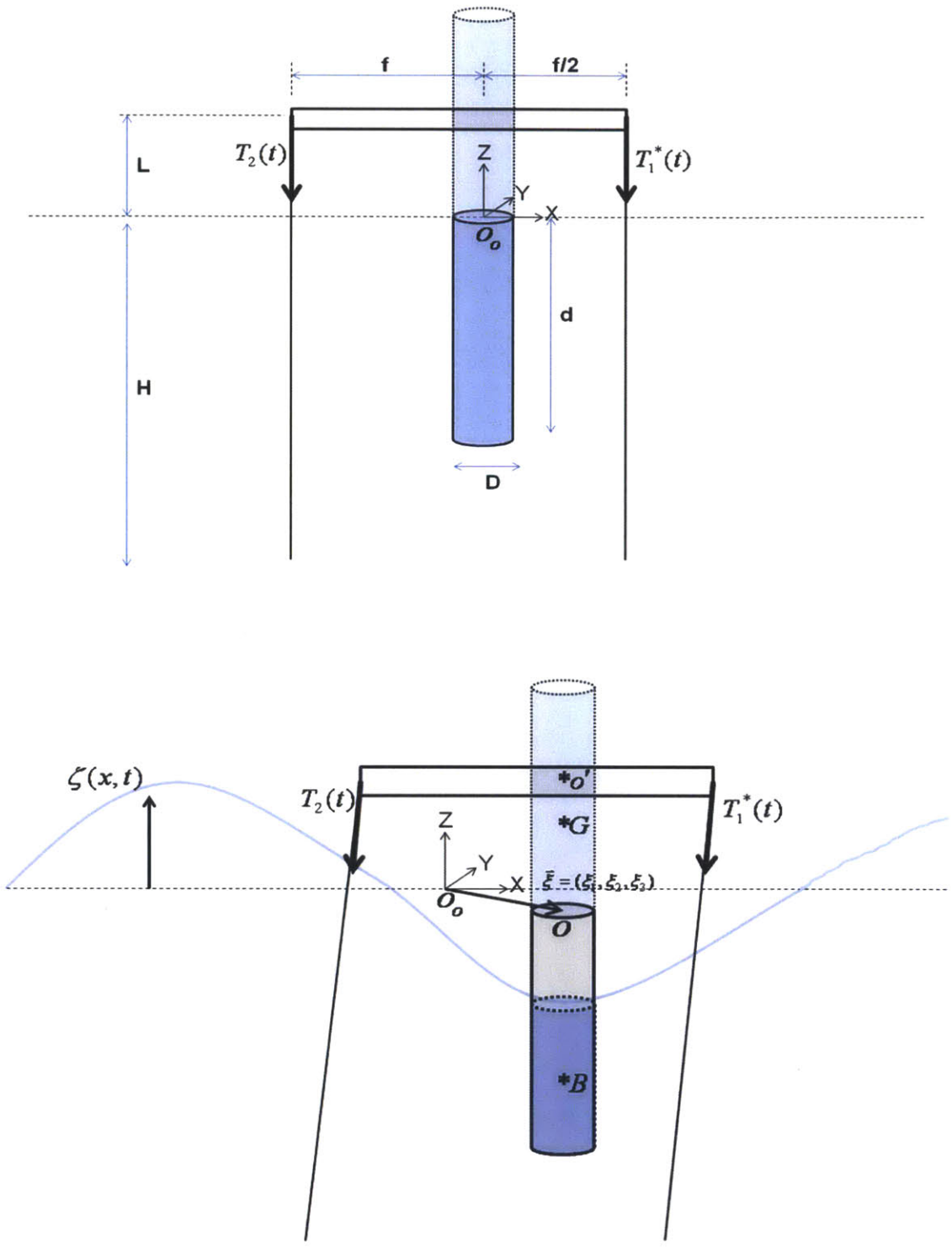


Figure 2-12: The coordinate system for equations of motion of the floating wind turbine.

Applying the linear momentum conservation principle for the surge and heave modes of motions, the total net force drives the time rate of change of a linear momentum in surge and heave respectively as follows.

$$\begin{aligned}
&\frac{d}{dt}\vec{P}(t) = \sum \vec{F}(t) \\
&M\ddot{\xi}_1(t) = \vec{F}_{Aero}(t)\cdot\vec{e}_1 + \vec{F}_{Hydro}(t)\cdot\vec{e}_1 + \vec{F}_{Mooring}(t)\cdot\vec{e}_1 + \vec{F}_{Viscous}(t)\cdot\vec{e}_1 \\
&M\ddot{\xi}_3(t) = \vec{F}_{Aero}(t)\cdot\vec{e}_3 + \vec{F}_{Hydro}(t)\cdot\vec{e}_3 + \vec{F}_{Mooring}(t)\cdot\vec{e}_3 + \vec{F}_{Viscous}(t)\cdot\vec{e}_3 - W_3
\end{aligned} \tag{2.36}$$

The total force consists of aerodynamic force from the wind $\vec{F}_{Aero}(t)$, hydrodynamic force from the wave $\vec{F}_{Hydro}(t)$, line force from the mooring lines $\vec{F}_{Mooring}(t)$, and viscous forces from the fluid $\vec{F}_{Viscous}(t)$.

Applying the angular momentum conservation principle about a moving reference point $o'$,

$$\begin{aligned}
&\Sigma\vec{M}_{o'}(t) = \frac{d}{dt}\vec{H}_{o'}(t) + \vec{V}_{o'}(t)\times\vec{P}(t) \\
&\textit{where} \\
&\vec{H}_{o'}(t) = \vec{H}_G(t) + \vec{r}_{O'G}(t)\times\vec{P}(t) \\
&\vec{H}_G(t) = I_{22}\dot{\xi}_5(t)\vec{e}_2 \approx 0 \\
&\vec{P}(t) = M\vec{V}_G(t)
\end{aligned} \tag{2.37}$$

Recall that

$$
\begin{aligned}
\vec{r}_{O'G}(t) &= (Z_G)\vec{e}_3 \\
\vec{V}_G(t) &= \frac{d}{dt}\vec{r}_{OG}(t) \\
&= \dot{\xi}_1\vec{e}_1 + \dot{\xi}_3\vec{e}_3 \\
\vec{r}_{O'G}(t)\times\vec{P}(t) &= M\left[(Z_G)\vec{e}_3\right]\times\left[\dot{\xi}_1\vec{e}_1 + \dot{\xi}_3\vec{e}_3\right] \\
&= M\left[(Z_G)\dot{\xi}_1\right]\vec{e}_2
\end{aligned}
\tag{2.38}
$$

Thus,

$$
\begin{aligned}
\frac{d}{dt}\vec{H}_{o'}(t) &\approx \frac{d}{dt}\left(\vec{r}_{O'G}(t)\times\vec{P}(t)\right) \\
&= M\left[(Z_G)\ddot{\xi}_1\right]\vec{e}_2 \\
\vec{V}_{o'}(t)\times\vec{P}(t) &= (\dot{\xi}_1\vec{e}_1 + \dot{\xi}_3\vec{e}_3)\times M(\dot{\xi}_1\vec{e}_1 + \dot{\xi}_3\vec{e}_3) \\
&= 0
\end{aligned}
\tag{2.39}
$$

Therefore,

$$
M(Z_G)\ddot{\xi}_1 = \vec{M}_{o'_{Aero}}(t)\cdot\vec{e}_2 + \vec{M}_{o'_{Hydro}}(t)\cdot\vec{e}_2 + \vec{M}_{o'_{Mooring}}(t)\cdot\vec{e}_2 + \vec{M}_{o'_{Viscous}}(t)\cdot\vec{e}_2 \tag{2.40}
$$

The total moment consists of an aerodynamic moment from the wind $\vec{M}_{o'_{Aero}}(t)$, hydrodynamic moment from the wave $\vec{M}_{o'_{Hydro}}(t)$, moment from the mooring lines $\vec{M}_{o'_{Mooring}}(t)$, the viscous moment from the fluid $\vec{M}_{o'_{Viscous}}(t)$.

The fully nonlinear equations of motion are obtained as follows.

$$
\begin{aligned}
M\ddot{\xi}_1(t) &= \vec{F}_{Aero}(t)\cdot\vec{e}_1 + \vec{F}_{Hydro}(t)\cdot\vec{e}_1 + \vec{F}_{Mooring}(t)\cdot\vec{e}_1 + \vec{F}_{Viscous}(t)\cdot\vec{e}_1 \\
M\ddot{\xi}_3(t) &= \vec{F}_{Aero}(t)\cdot\vec{e}_3 + \vec{F}_{Hydro}(t)\cdot\vec{e}_3 + \vec{F}_{Mooring}(t)\cdot\vec{e}_3 + \vec{F}_{Viscous}(t)\cdot\vec{e}_3 - W_3 \\
MZ_G\ddot{\xi}_1(t) &= \vec{M}_{O'_{Aero}}(t)\cdot\vec{e}_2 + \vec{M}_{O'_{Hydro}}(t)\cdot\vec{e}_2 + \vec{M}_{O'_{Mooring}}(t)\cdot\vec{e}_2 + \vec{M}_{O'_{Viscous}}(t)\cdot\vec{e}_2
\end{aligned}
\tag{2.41}
$$

where $M$ =total mass; $W_3$=total weight ($=Mg$); $\vec{r}_{O'G} = (0,0,Z_G)$.

Due to the kinematic constraint by the TLP tethers foundation, the translational motion variables, $\xi_1(t)$ and $\xi_3(t)$, can be expressed in terms of mooring line inclination angle, $\theta(t)$.

$$
\begin{aligned}
\xi_1(t) &= l\sin\theta(t) \\
\xi_3(t) &= l\left[\cos\theta(t) - 1\right]
\end{aligned}
\tag{2.42}
$$

The force from the mooring lines can be decomposed as follows.

$$
\vec{F}_{Mooring}(t) = \vec{T}_1^*(t) + \vec{T}_2(t) \tag{2.43}
$$

The mooring line forces in surge and heave are as follows respectively.

$$
\begin{aligned}
\vec{F}_{Mooring}(t)\cdot\vec{e}_1 &= -T_1^*(t)\sin\theta(t) - T_2(t)\sin\theta(t) \\
\vec{F}_{Mooring}(t)\cdot\vec{e}_3 &= -T_1^*(t)\cos\theta(t) - T_2(t)\cos\theta(t)
\end{aligned}
\tag{2.44}
$$

The total moment is defined as follows assuming unidirectional motion in surge.

$$\bar{M}_{O_{Mooring}}(t)\cdot\bar{e}_2 = -T_2(t)f\cos\theta + T_1^*(t)\frac{f}{2}\cos\theta \tag{2.45}$$

In an extreme wave environment or sea conditions, the offshore wind turbine tends to limit the rotor operation to prevent mechanical damages on the turbine. For the purpose of nonlinear dynamic response analysis of the floating wind turbine for extreme wave conditions, the wind turbine is assumed to stop operating the rotor and consequently the aerodynamic loading is set to zero in the present modeling of the equations of motion which justifies a zero aerodynamic force, $\bar{F}_{Aero}(t)$.

The viscous force from the fluid may be defined by the damping coefficients, $B_{v11}$ and $B_{v33}$, as follows.

$$\begin{aligned}\bar{F}_{Viscous}(t) &\approx -B_{v11}\dot{\xi}_1\left|\dot{\xi}_1\right|\bar{e}_1 - B_{v33}\dot{\xi}_3\left|\dot{\xi}_3\right|\bar{e}_3 \\ &= -B_{v11}(l\cos\theta(t)\dot{\theta}(t))\left|(l\cos\theta(t)\dot{\theta}(t))\right|\bar{e}_1 - B_{v33}(-l\sin\theta(t)\dot{\theta}(t))\left|(-l\sin\theta(t)\dot{\theta}(t))\right|\bar{e}_3\end{aligned} \tag{2.46}$$

The fully nonlinear equations of motion are re-formulated as follows.

$$
\begin{aligned}
&Ml\left[-sin\theta(t)\cdot\dot{\theta}(t)^2+\cos\theta(t)\cdot\ddot{\theta}(t)\right]+B_{v11}(l\cos\theta(t)\dot{\theta}(t))\left|(l\cos\theta(t)\dot{\theta}(t))\right| \\
&=\vec{F}_{Hydro}(t)\cdot\vec{e}_1-T_2(t)sin\theta(t)-T_1^*(t)\sin\theta(t)
\end{aligned}
$$

$$
\begin{aligned}
&Ml\left[-\cos\theta(t)\cdot\dot{\theta}(t)^2-\sin\theta(t)\cdot\ddot{\theta}(t)\right]+B_{v33}(-l\sin\theta(t)\dot{\theta}(t))\left|(-l\sin\theta(t)\dot{\theta}(t))\right| \\
&=\vec{F}_{Hydro}(t)\cdot\vec{e}_3-T_2(t)\cos\theta(t)-T_1^*(t)\cos\theta(t)-W_3
\end{aligned}
$$

$$
\begin{aligned}
&MZ_{CG}l\left[-sin\theta(t)\cdot\dot{\theta}(t)^2+\cos\theta(t)\cdot\ddot{\theta}(t)\right]++B_{v11}Z_{CB}(t)(l\cos\theta(t)\dot{\theta}(t))\left|(l\cos\theta(t)\dot{\theta}(t))\right| \\
&=\vec{M}_{o_{Hydro}}(t)\cdot\vec{e}_2-T_2(t)f\cos\theta(t)+T_1^*(t)\frac{f}{2}\cos\theta(t)
\end{aligned}
$$

(2.47)

where $M$ =total mass; $W_3$=total weight ($=Mg$); $\vec{r}_{\dot{O}G}=(0,0,Z_{CG})$; $\vec{r}_{\dot{O}B}=(0,0,Z_{CB})$

In a large-amplitude nonlinear wave event, the $Z_{CB}(t)$ is varying over time depending on the ambient wave elevation and the body's vertical displacement at each time step.

The hydrodynamic force, $\vec{F}_{Hydro}(t)$, is obtained by the Fluid Impulse Theory which contains a nonlinear Froude-Krylov force, a nonlinear disturbance force and a nonlinear hydrostatic force as presented in section 2.7.

$$
\vec{F}_{Hydro}(t)=-\rho\frac{d}{dt}\oint_{S_B^I(t)}\varphi_I\vec{n}ds-\rho\frac{d}{dt}\int_{S_B^I(t)}\varphi_D\vec{n}ds-\rho g\oint_{S_B^I(t)}Z\vec{n}ds \tag{2.48}
$$

where $\varphi_D$ is obtained by the time-domain 3D potential-flow simulation based on a transient free-surface Green-function method; $S_B^I(t)$ is the instantaneous body surface under the ambient wave.

With this nonlinear wave load model applied to large amplitude waves and large amplitude body motions, a direct numerical integration of the equations of motion will be carried out to solve for the nonlinear dynamic responses of buoy motion and line tension in extreme wave conditions.

A numerical time marching scheme may be designed accordingly by setting up 4 state variables as follows.

$$y_1 = \theta(t)$$
$$y_2 = \dot{\theta}(t)$$
$$y_3 = T_1^*(t)$$
$$y_4 = T_2(t)$$

## 2.6 Linearized Equations of Motion in Long Waves

For the purpose of validation of the nonlinear response simulations and analysis, linearized equations of motion have been derived as follows. It may be of a great interest to see the how this linear result compares with the nonlinear simulation results, which will be addressed in the subsequent chapters.

In the study of extreme wave load and response analysis of the floating wind turbine, the wind turbine is assumed to stop operating the rotor which means the mean wind thrust becomes zero and therefore the dynamic equilibrium point is defined as equal to zero. But under normal operating conditions, the mean wind thrust value is often taken as an additional input parameter which may require a non-zero equilibrium point.

Assuming motion and tension responses to be small, and by taking a linear perturbation analysis around the dynamic equilibrium point,

$$\begin{aligned}
\theta(t) &= \theta_o + \delta\theta(t) \\
\dot{\theta}(t) &= \delta\dot{\theta}(t) \\
\ddot{\theta}(t) &= \delta\ddot{\theta}(t) \\
T_1^*(t) &= T_{1o}^* + \delta T_1^*(t) \\
T_2(t) &= T_{2o} + \delta T_2(t)
\end{aligned} \tag{2.49}$$

where $\theta_o$, $T_{1o}^*$ and $T_{2o}$ are the mean value of displacement, lumped tension#1 and tension#2 respectively at the dynamic equilibrium point given the mean wind thrust.

Assuming the motion response, $\delta\theta(t)$, to be small,

$$\begin{aligned}
\cos\delta\theta(t) &\approx 1 \\
\sin\delta\theta(t) &\approx \delta\theta(t)
\end{aligned}$$

The viscous force from the fluid may be redefined by the equivalent linear damping coefficients, $B_{v11}^{e}$ and $B_{v33}^{e}$, obtained by equivalent linearization.

$$\begin{aligned}\vec{F}_{Viscous}(t) &\approx -B_{v11}^{e}\dot{\xi}_1\vec{e}_1 - B_{v33}^{e}\dot{\xi}_3\vec{e}_3 \\ &= -B_{v11}^{e}(l\cos\theta(t)\dot{\theta}(t))\vec{e}_1 - B_{v33}^{e}(-l\sin\theta(t)\dot{\theta}(t))\vec{e}_3\end{aligned} \tag{2.50}$$

The equations of motion can be expressed in terms of the perturbation variables $\delta\theta(t)$ , $\delta\dot{\theta}(t)$ , $\delta\ddot{\theta}(t)$ , $\delta T_1^*(t)$ and $\delta T_2(t)$ followed by a linearization process eliminating higher order terms. It yields a linear form of equations of motion as follows.

$$\begin{aligned}&M\left[l\cos\theta_o\delta\ddot{\theta}(t)\right] + B_{v11}^{e}\left[l\cos\theta_o\delta\dot{\theta}(t)\right] \\ &= \vec{F}_{Hydro}\cdot\vec{e}_1 - T_{2_o}\cos\theta_o\delta\theta(t) - \delta T_2(t)\sin\theta_o - T_{1_o}^{*}\cos\theta_o\delta\theta(t) - \delta T_1^{*}(t)\sin\theta_o\end{aligned}$$

$$\begin{aligned}&M\left[-l\sin\theta_o\delta\ddot{\theta}(t)\right] + B_{v33}^{e}\left[-l\sin\theta_o\delta\dot{\theta}(t)\right] \\ &= \vec{F}_{Hydro}(t)\cdot\vec{e}_3 + T_{2_o}\sin\theta_o\delta\theta(t) - \delta T_2(t)\cos\theta_o + T_{1_o}^{*}\sin\theta_o\delta\theta(t) - \delta T_1^{*}(t)\cos\theta_o\end{aligned}$$

$$\begin{aligned}&MZ_{CG}\left[l\cos\theta_o\delta\ddot{\theta}(t)\right] + B_{v11}^{e}Z_{CB}(t)\left[l\cos\theta_o\delta\dot{\theta}(t)\right] \\ &= \vec{M}_{O'_{Hydro}}\cdot\vec{e}_2 + f\left[T_{2_o}\sin\theta_o\delta\theta(t) - \delta T_2(t)\cos\theta_o\right] + \frac{f}{2}\left[-T_{1_o}^{*}\sin\theta_o\delta\theta(t) + \delta T_1^{*}(t)\cos\theta_o\right]\end{aligned}$$

(2.51)

By virtue of the linear wave and linear dynamics theory, the hydrodynamic force $\vec{F}_{Hydro}$ can be decomposed into the diffraction and radiation forces respectively, each of which is independent of the other.

$$\vec{F}_{Hydro}(t) = \vec{F}_{Hydro}^{DIF}(t) + \vec{F}_{Hydro}^{RAD}(t) \tag{2.52}$$

The extreme wave loads response is simulated for a monochromatic incident wave of a long wavelength, and therefore the radiation force $\vec{F}_{Hydro}^{RAD}(t)$ may be represented by using the impulsive added mass properties as follows.

$$\vec{F}_{Hydro}^{RAD}(t)\cdot\vec{e}_1 = -A_{11}\ddot{\xi}_1(t)$$
$$\vec{F}_{Hydro}^{RAD}(t)\cdot\vec{e}_3 = -A_{33}\ddot{\xi}_3(t)$$

where the $A_{11}$ and $A_{33}$ are the added mass in surge and heave respectively for w <<1, which can be obtained from WAMIT or can be approximated by $\rho\pi a^2 d$ and $\frac{2}{3}\rho\pi a^3$.

By virtue of the slenderness of the buoy, the diffraction force, $\vec{F}_{Hydro}^{DIF}(t)$, can be obtained by a strip theory which is a long-wave approximation method. For the extreme wave load analysis, it is justifiable to consider the wave length is large compared to dimensions of the buoy. Based on a strip theory and GI-Taylor's formula, the diffraction force $\vec{F}_{Hydro}^{DIF}(t)$ for x-unidirectional incident waves is evaluated by

$$\begin{aligned}
F_x(t) &= \int_{-d}^{0} F_x(z,t)dz = \int_{-d}^{0} -\left(\pi a^2 + \frac{A_{11}^{2D}}{\rho}\right)\left.\frac{\partial P_I(x,z,t)}{\partial x}\right|_{x=0} dz \\
M_y(t) &= \int_{-d}^{0} F_x(z,t)z dz = \int_{-d}^{0} -\left(\pi a^2 + \frac{A_{11}^{2D}}{\rho}\right)\left.\frac{\partial P_I(x,z,t)}{\partial x}\right|_{x=0} (z-L)dz \qquad (2.53) \\
F_z(t) &= \pi a^2 P_I(x,z,t)\big|_{\substack{x=0\\z=-d}}
\end{aligned}$$

where the $P_I(x,z,t)$ is the incident wave pressure, and the $A_{11}^{2D}$ is the sectional added mass in surge which can be approximated by $\rho\pi a^2$.

With a linear wave theory applied for the incident wave pressure for deep water,

$$F_x(t) = \mathrm{Re}\left\{2\rho\pi a^2 A w^2 \left(\frac{1-\exp(-kd)}{k}\right) i\exp(iwt)\right\}$$
$$M_y(t) = \mathrm{Re}\left\{2\rho\pi a^2 A w^2 \left(-\frac{1}{k^2}[1-\exp(-kd)] + \frac{1}{k} d\exp(-kd) - \frac{L}{k}[1-\exp(-kd)]\right) i\exp(iwt)\right\}$$
$$F_z(t) = \mathrm{Re}\left\{\pi a^2 \rho g A \exp(-kd + iwt)\right\}$$

(2.54)

Rearranging the equations of motion by moving the radiation force terms to the left-hand side of the equations,

$$(M + A_{11})\left[l\cos\theta_o \delta\ddot{\theta}(t)\right] + B^e_{v11}\left[l\cos\theta_o \delta\dot{\theta}(t)\right]$$
$$= \vec{F}^{DIF}_{Hydro}(t)\cdot\vec{e}_1 - T_{2_o}\cos\theta_o \delta\theta(t) - \delta T_2(t)\sin\theta_o - T^*_{1_o}\cos\theta_o \delta\theta(t) - \delta T^*_1(t)\sin\theta_o$$

$$(M + A_{33})\left[-l\sin\theta_o \delta\ddot{\theta}(t)\right] + B^e_{v33}\left[-l\sin\theta_o \delta\dot{\theta}(t)\right]$$
$$= \vec{F}^{DIF}_{Hydro}(t)\cdot\vec{e}_3 + T_{2_o}\sin\theta_o \delta\theta(t) - \delta T_2(t)\cos\theta_o + T^*_{1_o}\sin\theta_o \delta\theta(t) - \delta T^*_1(t)\cos\theta_o$$

$$(MZ_{CG} + A_{11}Z_{CB}(t))\left[l\cos\theta_o \delta\ddot{\theta}(t)\right] + B^e_{v11}Z_{CB}(t)\left[l\cos\theta_o \delta\dot{\theta}(t)\right]$$
$$= \vec{M}^{DIF}_{o_{Hydro}}(t)\cdot\vec{e}_2 + f\left[T_{2_o}\sin\theta_o \delta\theta(t) - \delta T_2(t)\cos\theta_o\right] + \frac{f}{2}\left[-T^*_{1_o}\sin\theta_o \delta\theta(t) + \delta T^*_1(t)\cos\theta_o\right]$$

(2.55)

where

$$\vec{F}^{DIF}_{Hydro}(t)\cdot\vec{e}_1 = \mathrm{Re}\left\{2\rho\pi a^2 A w^2 \left(\frac{1-\exp(-kd)}{k}\right) i\exp(iwt)\right\}$$
$$\vec{M}^{DIF}_{o_{Hydro}}(t)\cdot\vec{e}_2 = \mathrm{Re}\left\{2\rho\pi a^2 A w^2 \left(-\frac{1}{k^2}[1-\exp(-kd)] + \frac{1}{k} d\exp(-kd) - \frac{L}{k}[1-\exp(-kd)]\right) i\exp(iwt)\right\}$$
$$\vec{F}^{DIF}_{Hydro}(t)\cdot\vec{e}_3 = \mathrm{Re}\left\{\pi a^2 \rho g A \exp(-kd + iwt)\right\}$$

(2.56)

Again this is an efficient and accurate method just for a long wave with reasonably small wave steepness $kA$ which justifies a long-wave approximation method. It is useful to see how this linear long-wavelength model compares to the nonlinear simulation results, which are addressed in the following chapters.

## 2.7 Nonlinear Hydrodynamic Force

Total velocity potential in the fluid domain is denoted by $\varphi(X,Y,Z,t)$, and the fluid pressure $P(X,Y,Z,t)$ is obtained by the Bernoulli's formula

$$P(X,Y,Z,t) = -\rho\left(\frac{\partial\varphi}{\partial t} + \frac{1}{2}\nabla\varphi\cdot\nabla\varphi + gZ\right).$$

The total fluid force and moment acting on a body is in principle obtained by the direct integration of the pressure over the instantaneous wetted surface of the body $S_B^T(t)$ at each time step.

The Fluid Impulse Theory derived by Sclavounos [39] provides a new theoretical framework for analyzing hydrodynamic loads on floating bodies. By virtue of Fluid Impulse Theory, the total fluid forces and moments on floating bodies are reduced into the time rate of change of the fluid impulses, which do not

involve localized time derivatives and spatial gradients of the velocity potential over the panels. That is, the total fluid force is modeled just by a single time rate of change of the impulse of the velocity potential at each time step, which will allow us to approach the nonlinear hydrodynamic wave-body interaction problem in a very efficient and robust manner.

### 2.7.1 Nonlinear Hydrodynamic Force

Again, the fully nonlinear hydrodynamic force is defined by integrating the nonlinear Bernoulli pressure around the exact wetted surface of body $S_B^T(t)$. Following the notations and derivations presented in *Sclavounos* [39], the exact nonlinear hydrodynamic force is expanded as follows.

The nonlinear hydrodynamic force on a floating body is derived into

$$-\rho \int_{S_B^T(t)} \left[ \frac{d\varphi}{dt} + \frac{1}{2}\nabla\varphi\cdot\nabla\varphi + gZ \right] \vec{n}_+ ds \equiv -\rho \frac{d}{dt} \int_{S_B^T(t)} \varphi \vec{n}_+ ds - \rho g \int_{S_B^T(t)} Z \vec{n}_+ ds$$
$$-\rho \frac{d}{dt} \left[ \int_{S_F^T(t)} \varphi \vec{n}_+ ds + \int_{S_F^I(t)} \varphi_I \vec{n}_- ds \right] - \rho g \left[ \int_{S_F^T(t)} Z \vec{n}_+ ds + \int_{S_F^I(t)} Z \vec{n}_- ds \right] \tag{2.57}$$

where $S_B^T(t)$ is the exact wetted surface of the body; $S_F^T(t)$ is the exact wave free-surface; $S_F^I(t)$ is the incident wave free-surface.

Dividing the exact wetted surface of the body $S_B^T(t)$ into the wetted surface of the body under the incident wave free-surface $S_B^I(t)$ and the differential surface $dS$,

$$\begin{aligned} -\rho\frac{d}{dt}\int_{S_B^T(t)}\varphi\vec{n}_+ds &= -\rho\frac{d}{dt}\int_{S_B^I(t)}\varphi\vec{n}_+ds-\rho\frac{d}{dt}\int_{dS}\varphi\vec{n}_+ds \\ -\rho g\int_{S_B^T(t)}Z\vec{n}_+ds &= -\rho g\int_{S_B^I(t)}Z\vec{n}_+ds-\rho g\int_{dS}Z\vec{n}_+ds \end{aligned} \tag{2.58}$$

where $dS = S_B^T(t) - S_B^I(t)$.

Taking the intersectional surface $S_W^I(t)$ out of the total incident wave surface $S_F^I(t)$,

$$-\rho\frac{d}{dt}\left[\int_{S_F^T(t)}\varphi\vec{n}_+ds+\int_{S_F^I(t)}\varphi_I\vec{n}\_ds\right] = -\rho\frac{d}{dt}\int_{S_W^I(t)}\varphi_I\vec{n}\_ds-\rho\frac{d}{dt}\left[\int_{S_F^T(t)}\varphi\vec{n}_+ds+\int_{S_E^I(t)}\varphi_I\vec{n}\_ds\right]$$

$$-\rho g\left[\int_{S_F^T(t)}Z\vec{n}_+ds+\int_{S_F^I(t)}Z\vec{n}\_ds\right] = -\rho g\int_{S_W^I(t)}Z\vec{n}\_ds-\rho g\left[\int_{S_F^T(t)}Z\vec{n}_+ds+\int_{S_E^I(t)}Z\vec{n}\_ds\right] \tag{2.59}$$

Rewriting the equations of fully nonlinear momentum force accordingly,

$$\begin{aligned} -\rho\int_{S_B^T(t)}\left[\frac{d\varphi}{dt}+\frac{1}{2}\nabla\varphi\cdot\nabla\varphi+gZ\right]\vec{n}_+ds \equiv\ & -\rho\frac{d}{dt}\int_{S_B^I(t)}\varphi\vec{n}_+ds-\rho\frac{d}{dt}\int_{dS}\varphi\vec{n}_+ds \\ & -\rho g\int_{S_B^I(t)}Z\vec{n}_+ds-\rho g\int_{dS}Z\vec{n}_+ds \\ & -\rho\frac{d}{dt}\int_{S_W^I(t)}\varphi_I\vec{n}\_ds-\rho\frac{d}{dt}\left[\int_{S_F^T(t)}\varphi\vec{n}_+ds+\int_{S_E^I(t)}\varphi_I\vec{n}\_ds\right] \\ & -\rho g\int_{S_W^I(t)}Z\vec{n}\_ds-\rho g\left[\int_{S_F^T(t)}Z\vec{n}_+ds+\int_{S_E^I(t)}Z\vec{n}\_ds\right] \end{aligned}$$

(2.60)

Recall that the total velocity potential can be decomposed into the incident and disturbance potential.

$$\varphi = \varphi_I + \varphi_D$$

Rearranging the terms on the right-hand side,

$$-\rho \int_{S_B^T(t)} \left[ \frac{d\varphi}{dt} + \frac{1}{2} \nabla\varphi \cdot \nabla\varphi + gZ \right] \vec{n} ds \equiv$$

$$-\rho \frac{d}{dt} \int_{S_B^I(t)} \varphi_I \vec{n}_+ ds - \rho \frac{d}{dt} \int_{S_W^I(t)} \varphi_I \vec{n}_- ds - \rho \frac{d}{dt} \int_{S_B^I(t)} \varphi_D \vec{n}_+ ds - \rho g \int_{S_B^I(t)} Z \vec{n}_+ ds - \rho g \int_{S_W^I(t)} Z \vec{n}_- ds$$

$$-\rho \frac{d}{dt} \left[ \int_{S_F^T(t)+dS} (\varphi_I + \varphi_D) \vec{n}_+ ds + \int_{S_E^I(t)} \varphi_I \vec{n}_- ds \right] - \rho g \left[ \int_{S_F^T(t)+dS} Z \vec{n}_+ ds + \int_{S_E^I(t)} Z \vec{n}_- ds \right]$$

(2.61)

where $S_B^T(t)$ is the exact wetted surface of the body; $S_B^I(t)$ is the wetted surface of the body under the incident wave free-surface; $S_F^T(t)$ is the exact wave free-surface; $S_F^I(t)$ is the incident wave free-surface

The first five terms in the right-hand side of the equation above account for the body surface contribution and the last terms account for the free-surface contribution, all of which will be demonstrated in various wave conditions in the subsequent chapters.

## 2.7.2 Nonlinear Froude-Krylov Force

The first and second terms in the right hand side of Eq. (2.61) represent the nonlinear Froude-Krylov force and the impulse.

$$-\rho\frac{d}{dt}\int_{S_B^I(t)}\varphi_I\vec{n}_+ds-\rho\frac{d}{dt}\int_{S_W^I(t)}\varphi_I\vec{n}_-ds \tag{2.62}$$

Redefining the normal vector $\vec{n}$ as pointing out of the control surface, consisting of the body wetted surface under the ambient incident wave surface and its wetted surface, the nonlinear Froude-Krylov force and the impulse are represented as follows:

$$\begin{aligned}\vec{F}_{FK} &= -\rho\frac{d}{dt}\oint_{S_B^I(t)}\varphi_I\vec{n}ds\\ \vec{I}_{FK} &= -\rho\oint_{S_B^I(t)}\varphi_I\vec{n}ds\end{aligned} \tag{2.63}$$

## 2.7.3 Nonlinear Disturbance Force

The third term in the right hand side of Eq. (2.61) represents the total disturbance force which comes from the body radiation and diffraction contributions.

$$-\rho \frac{d}{dt} \int_{S_B^I(t)} \varphi_D \vec{n}_+ ds$$

Redefining the normal vector $\vec{n}$ as pointing out of the control surface consisting of the body wetted surface under the ambient incident wave surface and its wetted surface, the nonlinear disturbance force and the impulse are represented as follows:

$$\begin{aligned} \vec{F}_D &= -\rho \frac{d}{dt} \int_{S_B^I(t)} \varphi_D \vec{n} ds \\ \vec{I}_D &= -\rho \int_{S_B^I(t)} \varphi_D \vec{n} ds \end{aligned} \tag{2.64}$$

## 2.7.4 Nonlinear Hydrostatic Force

The fourth and fifth terms in the right hand side of Eq. (2.61) represent the nonlinear buoyancy force.

$$-\rho g \int_{S_B^I(t)} Z \vec{n}_+ ds - \rho g \int_{S_W^I(t)} Z \vec{n}\_ds$$

Redefining the normal vector $\vec{n}$ as pointing out of the control surface consisting of the body wetted surface under the ambient incident wave surface and its wetted surface, the nonlinear hydrostatic force is represented as follows.

$$\overline{F}_H = -\rho g \oint_{S_B^I(t)} Z\vec{n} ds \tag{2.65}$$

### 2.7.5 Nonlinear Free Surface Impulse Force

The rest of the terms in the right hand side of Eq. (2.61) represent the nonlinear free surface impulse force

$$\overline{F}_{FS} = -\rho \frac{d}{dt}\left[ \int_{S_F^T(t)+dS} (\varphi_I + \varphi_D)\vec{n}_+ ds + \int_{S_E^I(t)} \varphi_I \vec{n}_- ds \right] - \rho g \left[ \int_{S_F^T(t)+dS} Z\vec{n}_+ ds + \int_{S_E^I(t)} Z\vec{n}_- ds \right] \tag{2.66}$$

Under the weak-scatterer condition, the disturbance on the ambient wave surface can be assumed small and therefore the exact free surface will not deviate significantly from the incident wave free-surface. This allows us to linearize the disturbance from the incident wave surface elevation employing a perturbation theory in the following chapter.

## 2.8 Free Surface Impulse Force

Ambient waves are assumed to have an amplitude A of $O(1)$ comparable to the body dimension $d$. The ambient wave steepness kA is assumed to be small and the magnitude of the ambient wave $(\varphi_I, \zeta_I)$ becomes $O(kA) = O(\delta)$ where $\delta \sim 0.1$. In the wave-body interaction for ambient waves which have a wave length longer than the body diameter, the magnitude of the wave disturbance from the body $(\varphi_D, \zeta_D)$ becomes $O(kd) = O(\varepsilon)$ where typically $\varepsilon < 0.1$ in our design sea states. These order of magnitude estimates justify the linearization of the body wave disturbance about the ambient wave surface.

Rearranging the nonlinear free-surface force formula by adding and subtracting $\varphi_D$ the disturbance velocity potential,

$$\vec{F}_{FS} = +\rho \frac{d}{dt} \int_{S_E^I(t)} \varphi_D \vec{n}_- ds - \rho \frac{d}{dt} \left[ \int_{S_F^T(t)+dS} (\varphi_I + \varphi_D) \vec{n}_+ ds + \int_{S_E^I(t)} (\varphi_I + \varphi_D) \vec{n}_- ds \right]$$
$$- \rho g \left[ \int_{S_F^T(t)+dS} Z \vec{n}_+ ds + \int_{S_E^I(t)} Z \vec{n}_- ds \right] \tag{2.67}$$

The integration in the second and third terms in the right hand side is over a closed differential surface bounded by the nonlinear free surface, the ambient wave surface and the differential surface around the body waterline. The unit normal vector over this closed surface points outside the enclosed volume when the total wave elevation is larger than the ambient wave elevation and points inside the differential volume otherwise. The second and third terms may be reduced by an

application of Gauss' theorem over the volume bounded by the closed differential surface defined above. Denoting by $\zeta_D$ the disturbance wave elevation assumed to be a signed quantity, the unit normal vectors over the differential surface point outside the differential volume when $\zeta_D>0$ and inside the volume when $\zeta_D<0$. Applying Gauss' theorem we obtain

$$\vec{F}_{FS} = -\rho \frac{d}{dt} \int_{S_E^I(t)} \varphi_D \vec{n}_+ ds - \rho \frac{d}{dt} \left[ \iiint_{v(t)} (\nabla \varphi_I + \nabla \varphi_D) dv \right] \mathrm{sgn}(\zeta_D) - \rho g \vec{k} v(t) \mathrm{sgn}(\zeta_D) \tag{2.68}$$

The second and third terms in the right-hand side of the equation above can be expressed as integrals over the ambient wave free-surface exterior to the body applying a Taylor's series expansion as follows.

$$\vec{F}_{FS} = -\rho \frac{d}{dt} \int_{S_E^I(t)} \varphi_D \vec{n}_+ ds - \rho \frac{d}{dt} \int_{S_E^I(t)} \left[ \zeta_D \nabla(\varphi_I + \varphi_D) + \frac{1}{2} \zeta_D{}^2 \frac{\partial}{\partial Z} \nabla(\varphi_I + \varphi_D) + H.O.T. \right] ds - \rho g \vec{k} \int_{S_E^I(t)} \zeta_D ds \tag{2.69}$$

The unit normal vectors of the ambient wave surface and the exact wave surface can be expressed as

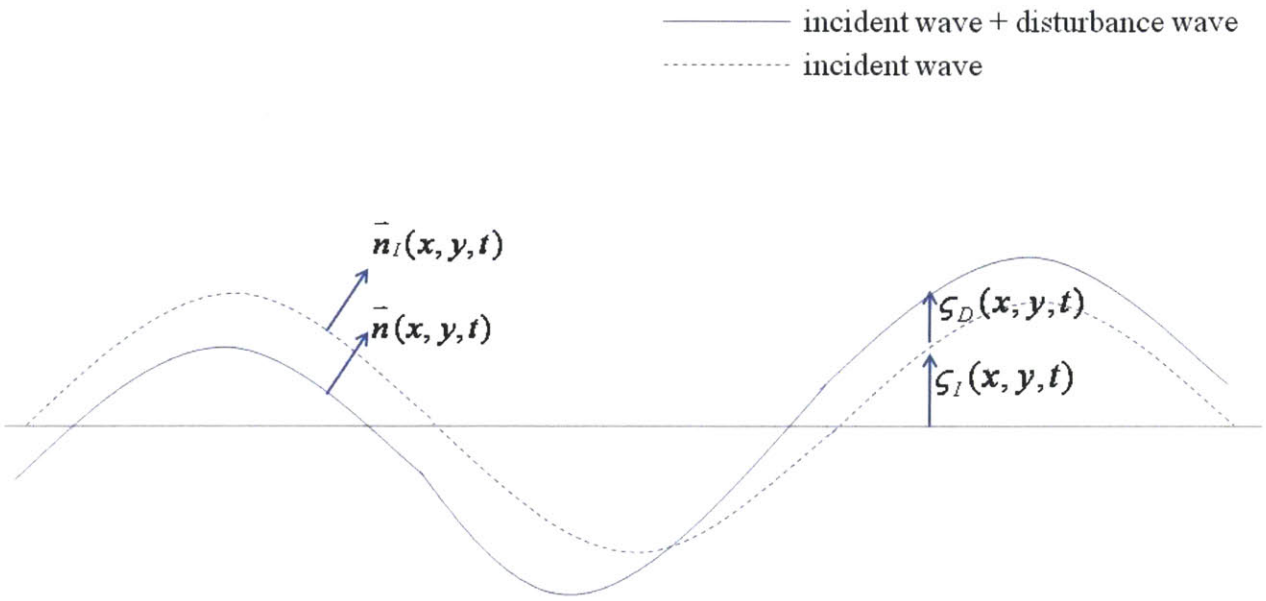


$\vec{n}_I(x,y,t)$ : The unit normal vector of the incident wave surface at (x,y) at time t

$\vec{n}(x,y,t)$ : The unit normal vector of the exact wave surface at (x,y) at time t

$\varsigma_I(x,y,t)$ : The incident wave elevation from z=0 plane at (x,y) at time t

$\varsigma_D(x,y,t)$ : The disturbance wave elevation from $\varsigma_I(x,y,t)$ at (x,y) at time t

Over the exact wave free-surface which is the sum of incident wave and disturbance waves,

$$F(x,y,z,t)=0$$

where $F(x,y,z,t) \triangleq z-\varsigma_I(x,y,t)-\varsigma_D(x,y,t)$

The unit normal vector of the exact free-surface at (x,y) at time t, $\vec{n}(x,y,t)$, is defined as follows.

$$\begin{aligned}\vec{n} &= \frac{\nabla F}{|\nabla F|} \\ &= \frac{\left(\frac{\partial F}{\partial x}, \frac{\partial F}{\partial y}, \frac{\partial F}{\partial z}\right)}{|\nabla F|} \\ &= \frac{\left(-\varsigma_{I_x} - \varsigma_{D_x}, -\varsigma_{I_y} - \varsigma_{D_y}, 1\right)}{|\nabla F|}\end{aligned} \tag{2.70}$$

Thus the unit normal vector of the exact wave surface at (x,y) at time t can be obtained as follows.

$$\begin{aligned}\vec{n} &= (n_1, n_2, n_3) \\ n_1 &= \frac{-\varsigma_{I_x} - \varsigma_{D_x}}{\left[(\varsigma_{I_x} + \varsigma_{D_x})^2 + (\varsigma_{I_y} + \varsigma_{D_y})^2 + 1\right]^{1/2}} \\ n_2 &= \frac{-\varsigma_{I_y} - \varsigma_{D_y}}{\left[(\varsigma_{I_x} + \varsigma_{D_x})^2 + (\varsigma_{I_y} + \varsigma_{D_y})^2 + 1\right]^{1/2}} \\ n_3 &= \frac{1}{\left[(\varsigma_{I_x} + \varsigma_{D_x})^2 + (\varsigma_{I_y} + \varsigma_{D_y})^2 + 1\right]^{1/2}}\end{aligned} \tag{2.71}$$

The unit normal vector of incident wave surface at (x,y) at time t, $\vec{n}_I(x,y,t)$, is defined as follows.

$$
\begin{aligned}
\bar{n}_I &= (n_{I_1}, n_{I_2}, n_{I_3}) \\
n_{I_1} &= \frac{-\varsigma_{I_x}}{\left[\varsigma_{I_x}{}^2 + \varsigma_{I_y}{}^2 + 1\right]^{1/2}} \\
n_{I_2} &= \frac{-\varsigma_{I_y}}{\left[\varsigma_{I_x}{}^2 + \varsigma_{I_y}{}^2 + 1\right]^{1/2}} \\
n_{I_3} &= \frac{1}{\left[\varsigma_{I_x}{}^2 + \varsigma_{I_y}{}^2 + 1\right]^{1/2}}
\end{aligned}
\tag{2.72}
$$

For a monochromatic incident wave propagating in x-direction, the spatial derivative of the surface elevation with respect to y becomes zero.

$$\varsigma_{I_y} = 0$$

Rewriting the unit normal vectors of the exact wave surface at (x,y) at time t,

$$
\begin{aligned}
\bar{n} &= (n_1, n_2, n_3) \\
n_1 &= \frac{-\varsigma_{I_x} - \varsigma_x}{\left[(\varsigma_{I_x} + \varsigma_x)^2 + (\varsigma_y)^2 + 1\right]^{1/2}} \\
n_2 &= \frac{-\varsigma_y}{\left[(\varsigma_{I_x} + \varsigma_x)^2 + (\varsigma_y)^2 + 1\right]^{1/2}} \\
n_3 &= \frac{1}{\left[(\varsigma_{I_x} + \varsigma_x)^2 + (\varsigma_y)^2 + 1\right]^{1/2}}
\end{aligned}
\tag{2.73}
$$

Rewriting the unit normal vectors of the incident wave surface at (x,y) at time t,

$$
\begin{aligned}
&\vec{n}_I = (n_{I_1}, n_{I_2}, n_{I_3}) \\
&n_{I_1} = \frac{-\varsigma_{I_x}}{\left[\varsigma_{I_x}{}^2 + 1\right]^{1/2}} = -\varsigma_{I_x}[1 + O(\delta^2)] \\
&n_{I_2} = 0 \\
&n_{I_3} = \frac{1}{\left[\varsigma_{I_x}{}^2 + 1\right]^{1/2}} = [1 + O(\delta^2)]
\end{aligned}
\tag{2.74}
$$

It follows from Eq. (2.69) that the horizontal component of the free-surface force takes the form

$$
F_{X\text{-}FS} = -\rho \frac{d}{dt} \int_{S_E^I(t)} \varphi_D n_x ds - \rho \frac{d}{dt} \int_{S_E^I(t)} \left[ \zeta_D \frac{\partial}{\partial X}(\varphi_I + \varphi_D) + \frac{1}{2} \zeta_D{}^2 \frac{\partial}{\partial Z} \frac{\partial}{\partial X}(\varphi_I + \varphi_D) + H.O.T. \right] ds
\tag{2.75}
$$

The horizontal component of the unit normal vector on the ambient wave is given from the expression in Eq. (2.74). Substituting it in Eq. (2.75) and with errors of $O(\delta^2, \delta\varepsilon^2)$, it can be reduced to

$$
F_{X\text{-}FS} = \rho \frac{d}{dt} \int_{S_E^I(t)} \left[ \varphi_D \frac{\partial \zeta_I}{\partial X} - \zeta_D \frac{\partial}{\partial X}(\varphi_I + \varphi_D) \right] ds
\tag{2.76}
$$

It follows from Eq. (2.69) that the vertical component of the free-surface force takes the form

$$
F_{Z\text{-}FS} = -\rho \frac{d}{dt} \int_{S_E^I(t)} \varphi_D n_Z ds - \rho \frac{d}{dt} \int_{S_E^I(t)} \left[ \zeta_D \frac{\partial}{\partial Z}(\varphi_I + \varphi_D) + \frac{1}{2} \zeta_D{}^2 \frac{\partial^2}{\partial Z^2}(\varphi_I + \varphi_D) + H.O.T. \right] ds - \rho g \int_{S_E^I(t)} \zeta_D ds
\tag{2.77}
$$

The vertical component of the unit normal vector on the ambient wave is given from the expression in Eq. (2.74). Substituting it in Eq. (2.77) and with errors of $O(\varepsilon\delta^2)$, it can be reduced to

$$\begin{aligned} F_{Z-FS} &= -\rho \frac{d}{dt} \int_{S_E^I(t)} \left[ \varphi_D + \zeta_D \frac{\partial \varphi_I}{\partial Z} \right] ds - \rho g \int_{S_E^I(t)} \zeta_D ds \\ &= -\rho \int_{S_E^I(t)} \left[ \frac{\partial \varphi_D}{\partial t} + g\zeta_D + \frac{\partial \zeta_I}{\partial t} \frac{\partial \varphi_D}{\partial Z} + \zeta_D \frac{\partial^2 \varphi_I}{\partial Z \partial t} \right] ds \end{aligned} \tag{2.78}$$

This order of magnitude analysis reveals that the free-surface contributions are small compared to the body surface contributions addressed in previous chapters. Again, the relative significance of those free-surface contributions on the hydrodynamic force on floating bodies will depend on the ambient wave steepness $kA$ and the relative body dimension $kd$. In the weak-scatterer condition where the $kA$ and $kd$ are defined as sufficiently small, the hydrodynamic force on floating bodies will be dominated by the body surface contribution obtained by the nonlinear Froude-Krylov force, the nonlinear disturbance force and the nonlinear hydrostatic force. This will introduce a new way of modeling the hydrodynamic force on floating bodies that is efficient and accurate.

# Chapter 3

# Numerical Analysis and Results

## 3.1 A Quadrilateral Constant-Strength Source Panel Element

A quadrilateral constant-strength source element is presently taken as the 3D Panel element to represent the floating body boundary in order to model its hydrodynamic interaction with surface waves. At each quadrilateral element the singularity strength is uniformly distributed over each element. The strength of this element is the primary unknown and a panel code using N elements can be constructed to solve for those N constants based on the body boundary condition presented in the previous and subsequent chapters.

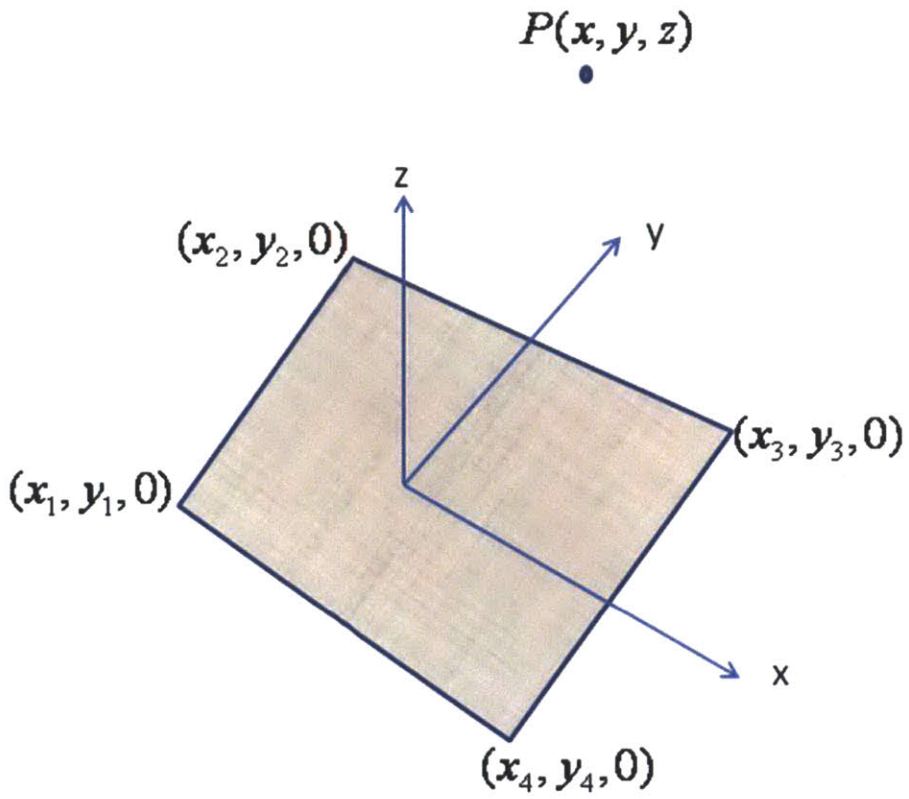


Figure 3-1: A 3D Quadrilateral constant-strength source element

Let's consider a surface element with a constant-strength source distribution $\sigma$ per area bounded by 4 lines. Given the four points denoted as $(x_1, y_1, 0), \ldots, (x_4, y_4, 0)$, the velocity potential at a point P (x,y,z) due to this element is

$$\varphi(x,y,z) = \frac{-\sigma}{4\pi} \int_S \frac{ds}{\sqrt{(x-x_o)^2 + (y-y_o)^2 + z^2}}$$

$$\nabla\varphi = \left( \frac{\partial\varphi}{\partial x}, \frac{\partial\varphi}{\partial y}, \frac{\partial\varphi}{\partial z} \right)$$

(3.1)

The closed form solution of the velocity potential and velocity components in x,y and z due to the quadrilateral constant-strength source element is taken from the Eq. (10.89) and (10.95) from Katz [14].

When the point P is sufficiently far from the center of the element (xo,yo,0), the quadrilateral source element of an area A can be approximated by an equivalent point source and this will help to increase the computational efficiency and lower the computational cost. When the point is far from the element, the velocity potential can be approximated as follows.

$$\varphi(x,y,z) = \frac{-\sigma A}{4\pi\sqrt{(x-x_o)^2+(y-y_o)^2+z^2}} \tag{3.2}$$

The velocity components can also be approximated as follows.

$$\begin{aligned} u(x,y,z) &= \frac{\sigma A(x-x_o)}{4\pi\left[(x-x_o)^2+(y-y_o)^2+z^2\right]^{3/2}} \\ v(x,y,z) &= \frac{\sigma A(y-y_o)}{4\pi\left[(x-x_o)^2+(y-y_o)^2+z^2\right]^{3/2}} \\ w(x,y,z) &= \frac{\sigma A(z-z_o)}{4\pi\left[(x-x_o)^2+(y-y_o)^2+z^2\right]^{3/2}} \end{aligned} \tag{3.3}$$

To determine the range of distance over which this far-field approximation method is applicable, a comparison of near- and far-field formulas has been studied in terms of the induced velocities versus the distance from element in a vertical or horizontal direction. The results are plotted below.

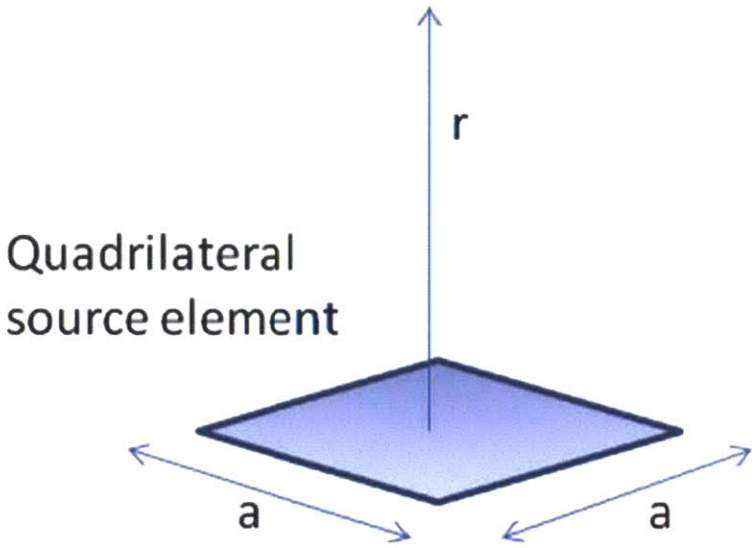


Figure 3-2: The vertical distance versus the applicability of far-field approximation

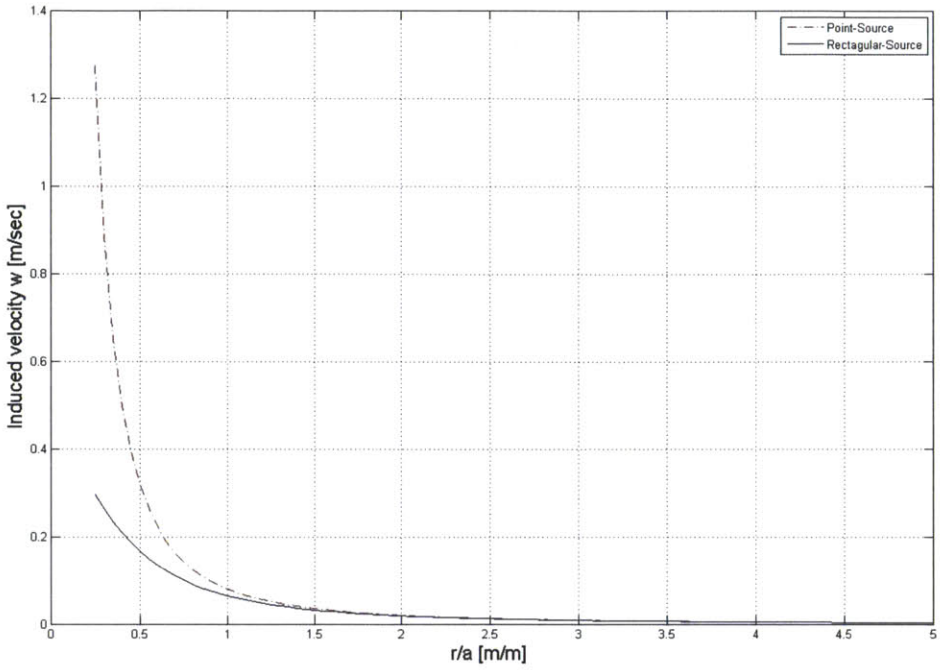


Figure 3-3: Comparison between a quadrilateral source element and an equivalent point source over the vertical distance r.

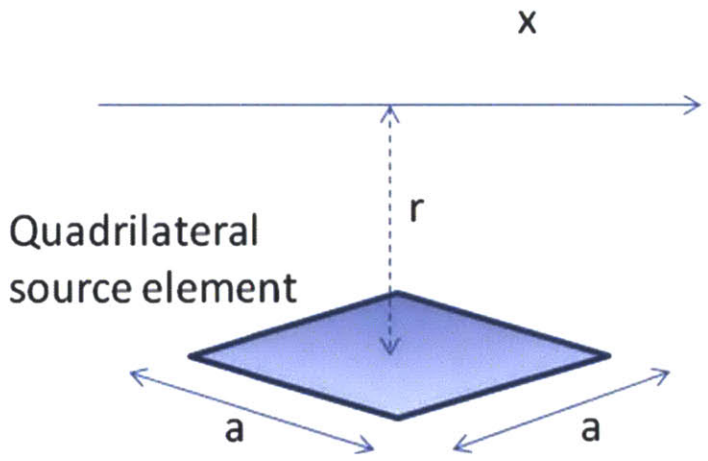


Figure 3-4: The horizontal distance versus the applicability of far-field approximation

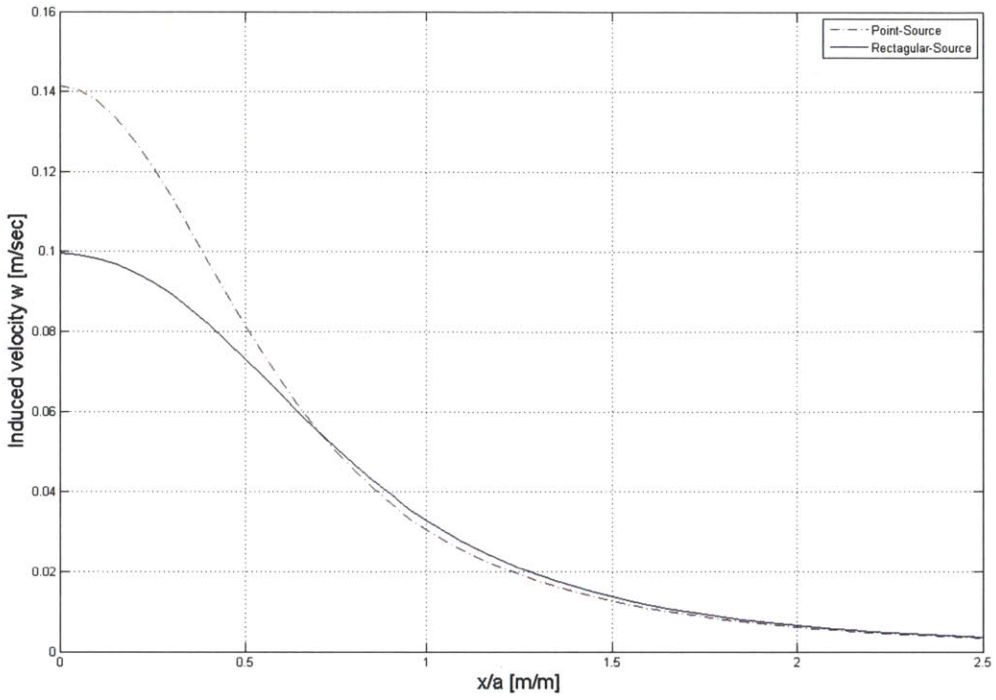


Figure 3-5: Comparison between a quadrilateral source element and an equivalent point source over the horizontal survey line in x direction.

As seen in the plots, an equivalent point source approximation is clearly valid if the distance is more than approximately 1 panel diameter either in horizontal or vertical direction. Out of this sensitivity study, the validity of a 3D quadrilateral source element approximation with an equivalent point source has been successfully demonstrated and is presently implemented into my panel code that helps to minimize the computational cost significantly.

As revealed in the above analysis, when the distance is less than 1 panel diameter then an accurate evaluation of the influence due to the quadrilateral source element is critical to the successful computation of velocity potential and induced velocities. Particularly when the point of interest is located at the center of the source element, to compute the velocity potential is numerically challenging. To improve the computational efficiency by illuminating the numerical complexity associated with the singularity, an alternative numerical treatment is suggested in the present study.

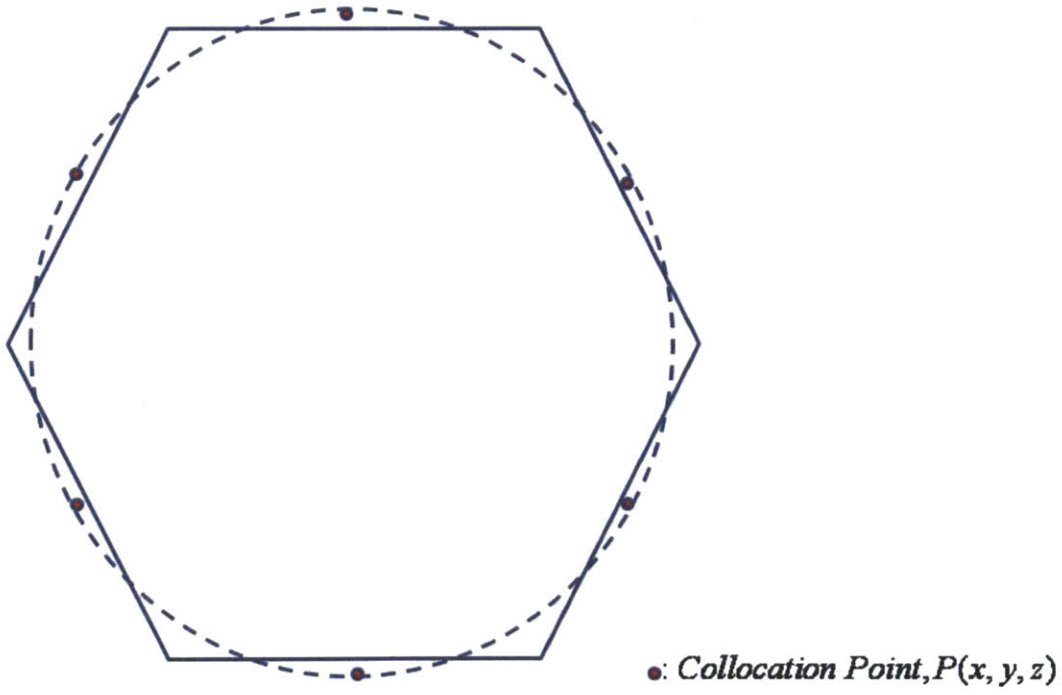


Figure 3-6: Top view of a cylindrical body and numerical panel elements surrounding the body surface (Simplified in terms of the number of panel elements)

The body boundary condition is imposed on field points on the exact body surface, which is often referred to as collocation points. An accurate evaluation of influence coefficients between source points and field points is required to determine strengths of source panel-elements upon the body boundary condition. The evaluation of influence coefficient becomes tricky when the field point is in the proximity of or identical with the source point. To prevent a singularity in the numerical computation, a source point is designed to be located a little off a field point as illustrated in the figure below. This method enhances the computational stability and provides an accurate solution.

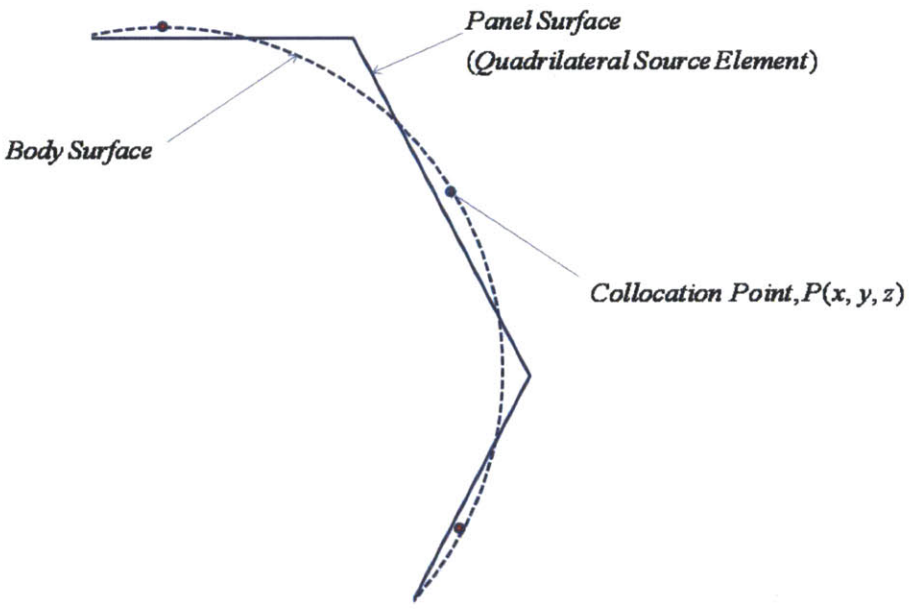


Figure 3-7: The field point at the exact body surface, and the source point at the panel element.

## 3.2 Convergence Tests

Convergence tests were carried out by varying the number of panels on the body surface under the waterline.

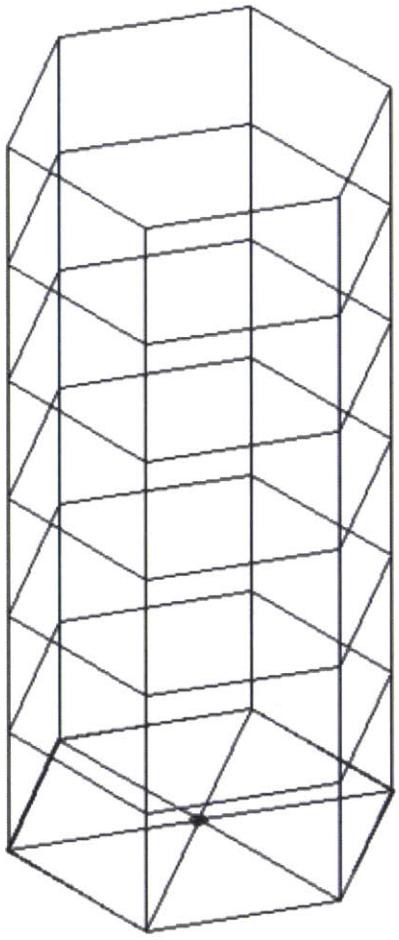

Figure 3-8: 90 Panels (uniform distribution)

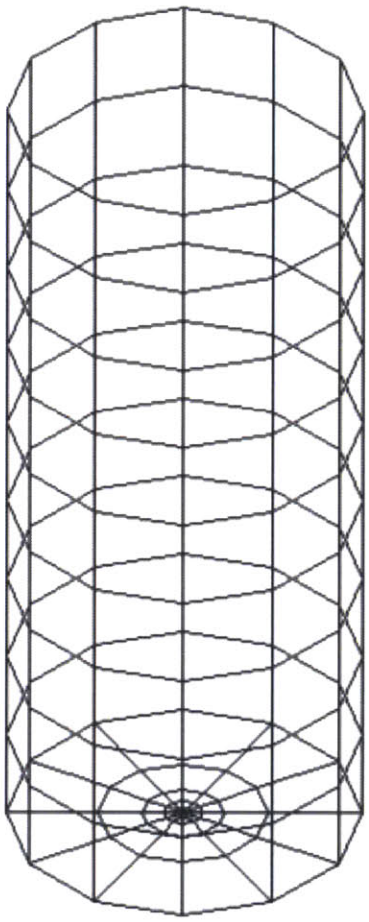

Figure 3-9: 216 Panels (uniform distribution)

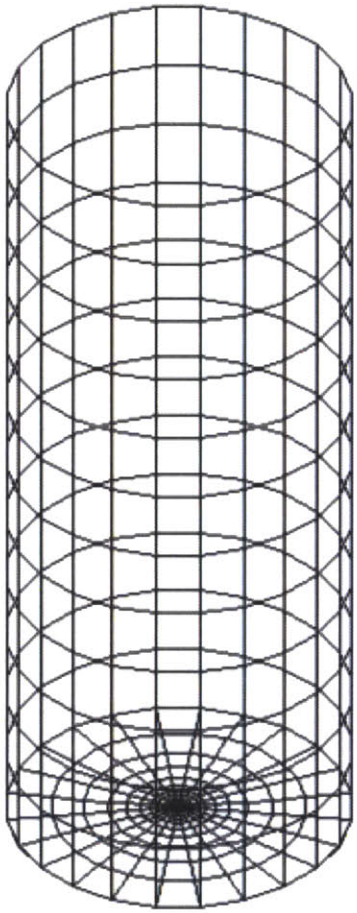

Figure 3-10: 384 Panels (uniform distribution)

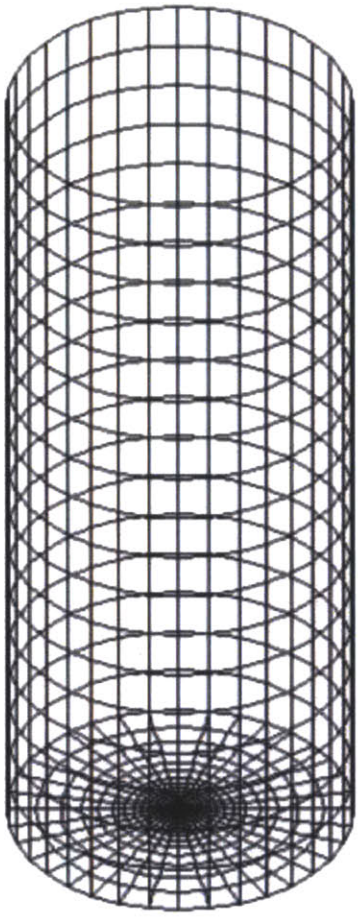

Figure 3-11: 972 Panels (uniform distribution)

Using the nonlinear wave load model based on the Fluid Impulse Theory, the simulation of a nonlinear diffraction problem is carried out by varying the number of panels on the body surface under the waterline.

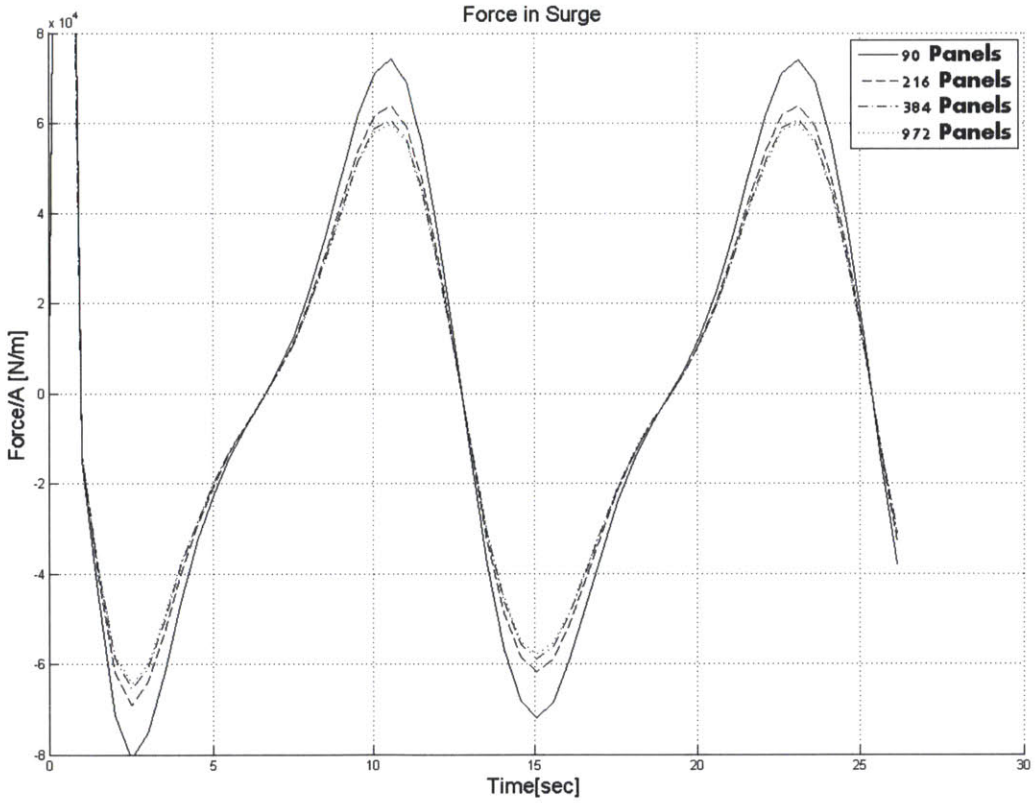


Figure 3-12: Convergence tests for the number of panels on the body surface in a nonlinear diffraction problem

## 3.3 Computational Effort

The majority of the computational cost is dominated by the evaluation of the transient Green function, which involves convolution integrals over time. In the case of linear body- and free-surface problems, the body boundary condition is imposed on numerical panel elements that are uniform over time. Thus in the linear problem, the impulsive Green function influence coefficients need to be evaluated only once and reused for every time step. In addition, the transient Green function coefficients, the so-called memory contribution, can also be obtained in an efficient manner. The number of Green function coefficients needed in the linear problem at every time step is

$$N_p \times N_p$$

where $N_p$ is the number of unknowns which is essentially the number of panels on the body surface.

In the fully nonlinear problem where both the body motions and free surface elevation have large amplitudes, however, the impulsive Green function needs to be computed at every single time step and the transient Green function coefficients can no longer reuse the special variables from prior time steps. The number of Green function coefficients that need to be computed at every time step is

$$N_p \times N_p \times (N_{ct} + 1)$$

where $N_p$ is the number of unknowns which is essentially the number of panels on the body surface; $N_{ct}$ is the current time step.

The total number of computations of Green function coefficients needed during the entire $N_t$ time-steps simulation is:

$$N_p \times N_p \times \left( N_t + \frac{N_t \times (N_t + 1)}{2} \right)$$

where $N_p$ is the number of unknowns which is essentially the number of panels on body surface; $N_t$ is the total number of time steps used.

For the fully nonlinear interaction problem, therefore, the order of magnitude of the total computational effort can be estimated as

$$O\left( \frac{N_p{}^2 \times N_t{}^2}{2} \right)$$

The computational effort on MATLAB in terms of CPU time is addressed by varying the number of panels on the body surface.

| | Number of panels | Total CPU time (hours) | Average CPU time per a time step (min.) |
|---|---|---|---|
| Case1 | 972 | ~ 15.0 | ~18 |
| Case2 | 384 | ~4.0 | ~4.8 |

| | | | |
|---|---|---|---|
| Case3 | 216 | ~1.0 | ~1.2 |
| Case4 | 90 | <0.5 | <0.6 |

Table 3-1: The computational effort on MATLAB in terms of CPU time for different number of panels

## 3.4 Radiation Problem in a Surge-Only Oscillation

The floating wind turbine will be based on a cylindrical platform that is vertically slender. In order to analyze the hydrodynamic memory effect associated with a vertically slender cylindrical buoy, a simple surge-only harmonic oscillation is simulated and presented as a test case in the present chapter. This is a simple radiation problem in a calm water surface with no incident wave potential existent. It is expected that the memory component effect will be small compared to the impulsive component because of the vertical slenderness of the body which will lead to simplified equations of motion in the subsequent chapter.

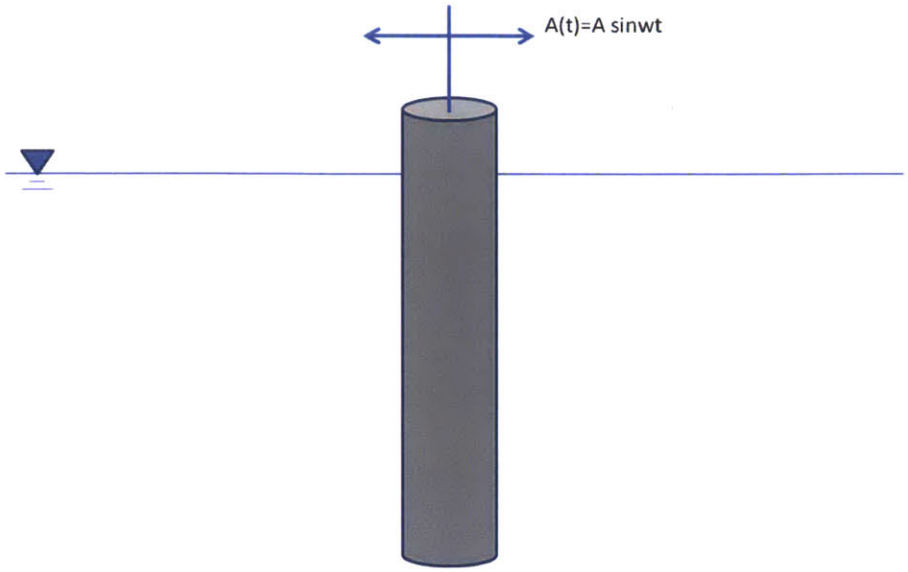


Figure 3-13: Test case - A surge-only forced harmonic oscillation

(Radius=2m; Draft=10m; A=1m)

The exact nonlinear hydrodynamic force on a body is defined by integration of the nonlinear Bernoulli pressure over the body's wetted surface $S_B(t)$ at each time step.

$$\bar{F}(t) = -\rho \int_{S_B^I(t)} \left[ \frac{\partial \varphi}{\partial t} + \frac{1}{2} \nabla \varphi \cdot \nabla \varphi + gZ \right] \bar{n} \, dS \tag{3.4}$$

By taking the hydrodynamic force from the body-impulse contribution as presented in Chapter 2, the nonlinear wave load on a floating body is obtained by

$$\bar{F}(t) = -\rho \frac{d}{dt} \oint_{S_B^I(t)} \varphi_I \bar{n} ds - \rho \frac{d}{dt} \int_{S_B^I(t)} \varphi_D \bar{n} ds - \rho g \oint_{S_B^I(t)} Z \bar{n} ds \tag{3.5}$$

where $\varphi_D$ is obtained by the time-domain 3D potential-flow simulation based on a transient free-surface Green-function method; $S_B^I(t)$ is the instantaneous body surface under the ambient wave.

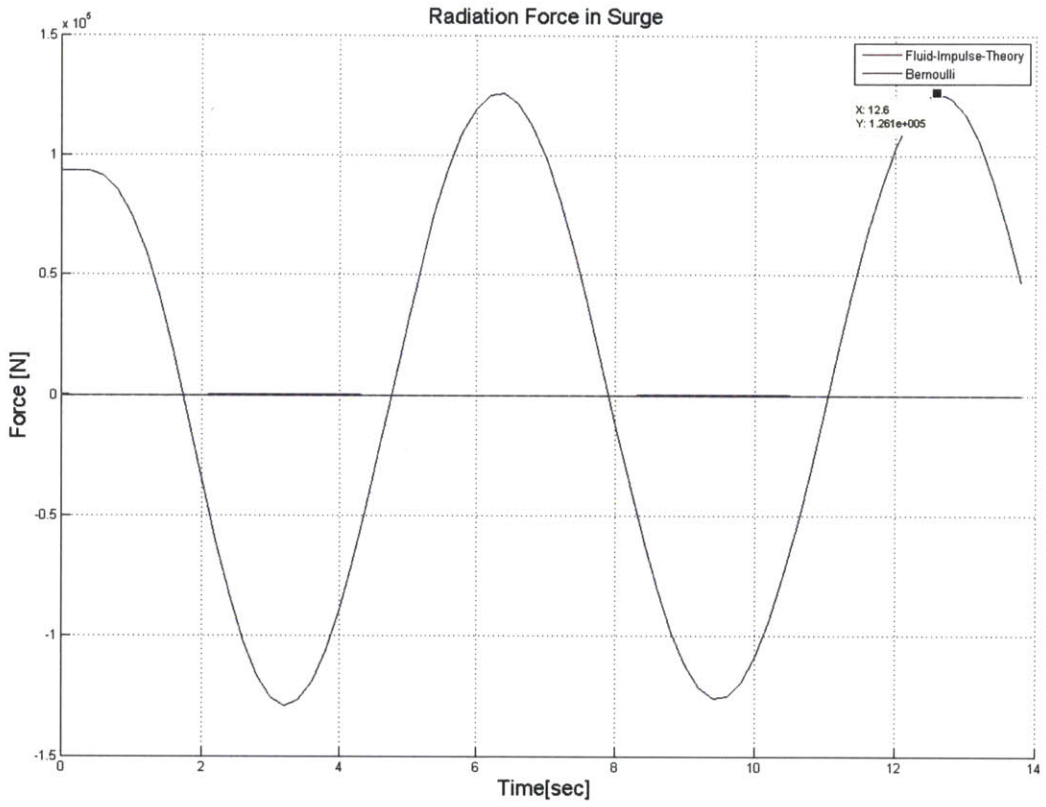


Figure 3-14: The hydrodynamic force in surge (test case: w=1.0 rad/sec)

The added mass and wave damping is obtained from the magnitude and phase of hydrodynamic force acting on the body.

$$F_1(t) = -A_{11}\ddot{\xi}_1(t) - B_{11}\dot{\xi}_1(t) \tag{3.6}$$

where

$$F_1(t) = \mathrm{Re}\left\{\Gamma_1 e^{i\omega t}\right\}$$
$$\xi_1(t) = \mathrm{Re}\left\{\Xi_1 e^{i\omega t}\right\}$$
$$\Gamma_1 = \left[\omega^2 A_{11} - i\omega B_{11}\right]\Xi_1$$

Since it's a forced oscillation of unit amplitude,

$$\Xi_1 = 1$$

The phase of the force is defined as follows.

$$\left|\Gamma_1\right| = \left|\omega^2 A_{11} - i\omega B_{11}\right|$$
$$\measuredangle\Gamma_1 = \tan^{-1}\left[-\frac{B_{11}}{\omega A_{11}}\right] \tag{3.7}$$

By comparing the added mass and wave damping obtained by this method with those obtained from WAMIT, the numerical implementation of the three-dimensional source element method has been validated as shown below.

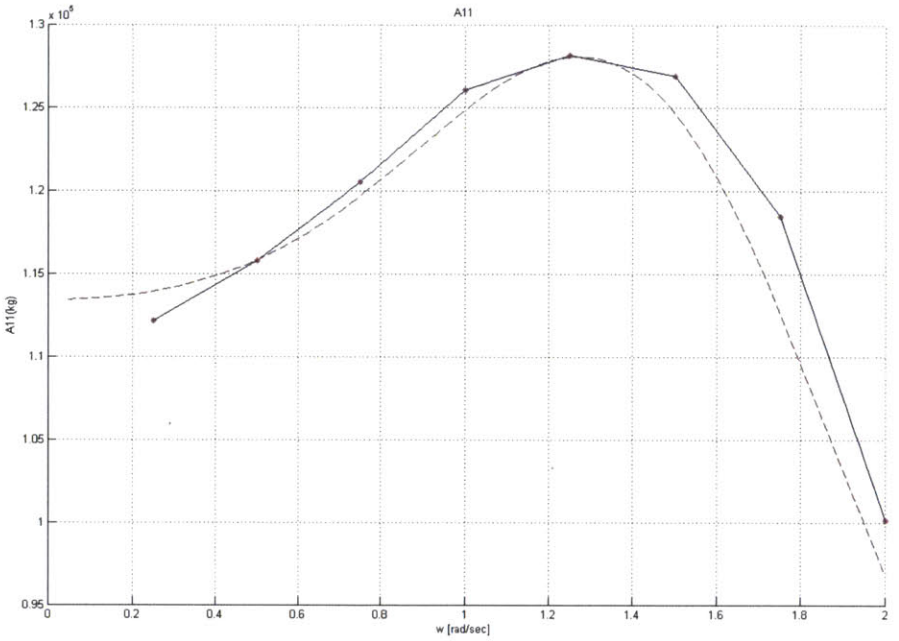


Figure 3-15: Added mass in surge, $A_{11}(\omega)$ compared with WAMIT

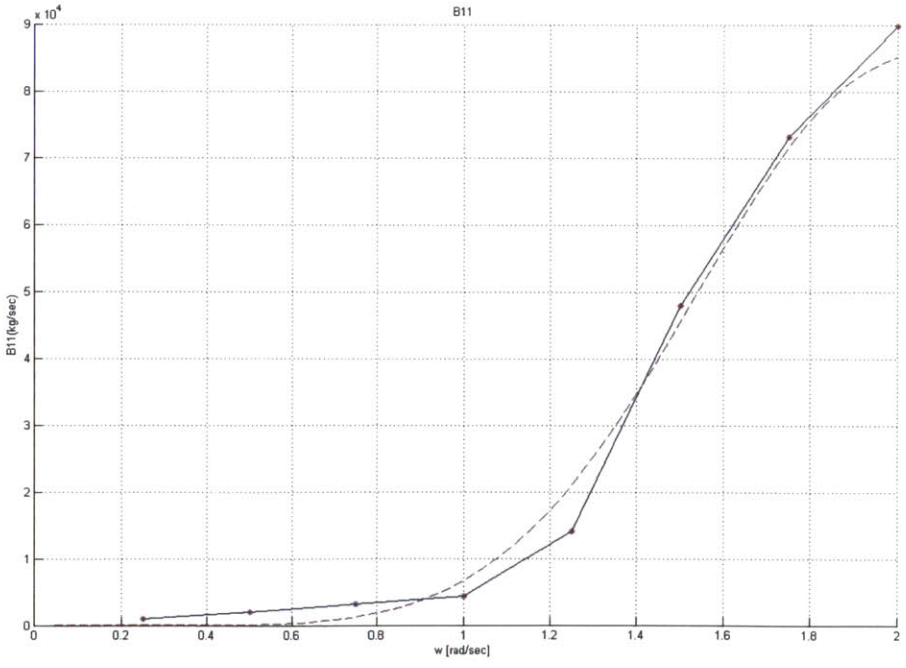


Figure 3-16: Wave damping in surge, $B_{11}(\omega)$ compared with WAMIT

## 3.5 Radiation Problem in a Heave-Only Oscillation

A heave-only forced harmonic oscillation is simulated and presented as a test case in this chapter. This is a simple radiation problem in calm water with no incident wave potential present.

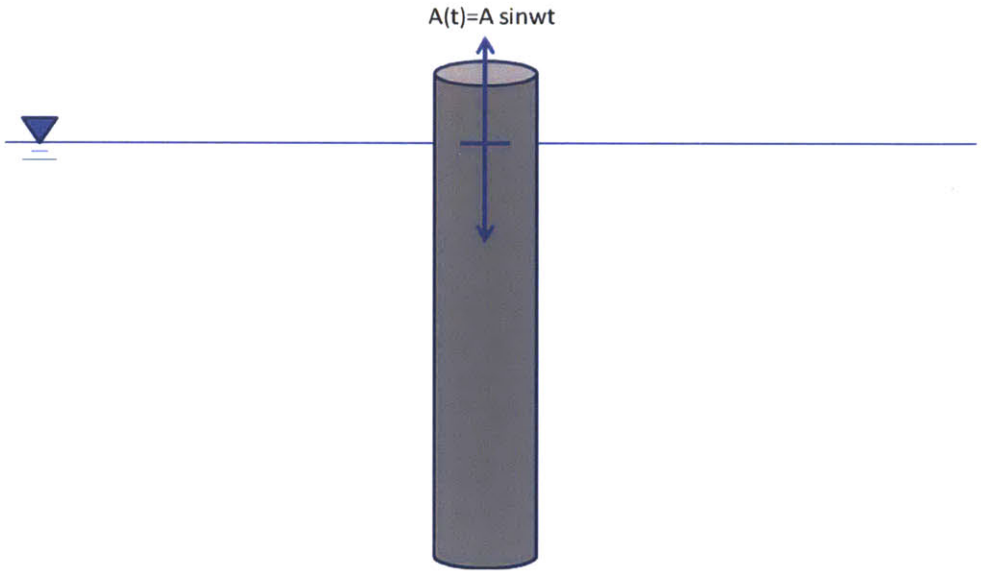


Figure 3-17: Test case - A heave-only forced harmonic oscillation
(Radius=2m; Draft=10m; A=1m)

$$\overline{F}(t) = -\rho \frac{d}{dt} \oint_{S_B^I(t)} \varphi_I \bar{n} ds - \rho \frac{d}{dt} \int_{S_B^I(t)} \varphi_D \bar{n} ds - \rho g \oint_{S_B^I(t)} Z \bar{n} ds$$

where $\varphi_D$ is obtained by the time-domain 3D potential-flow simulation based on a transient free-surface Green-function method; $S_B^I(t)$ is the instantaneous body surface under the ambient wave.

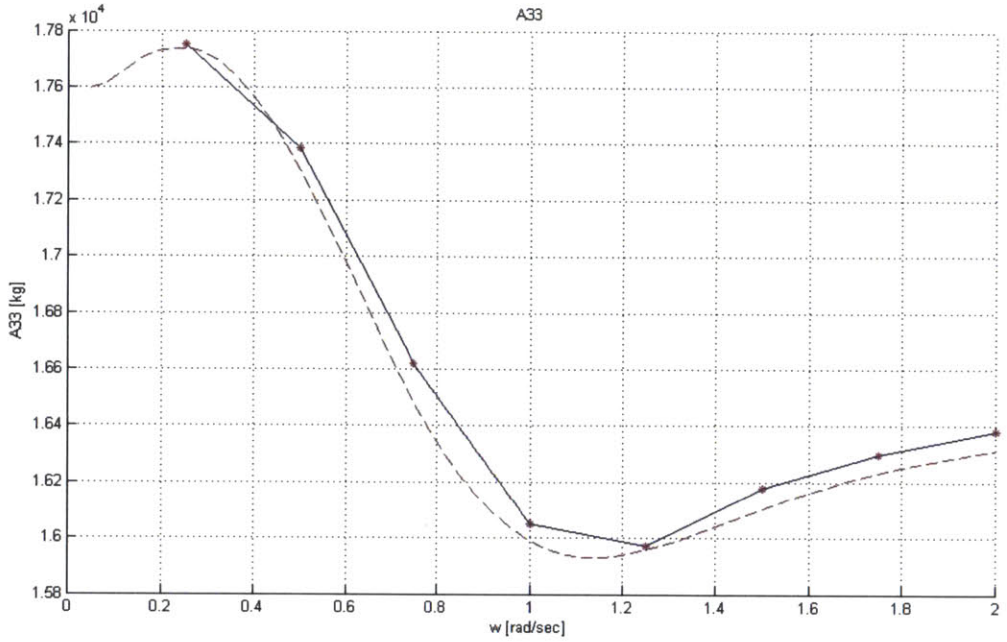


Figure 3-18: Added mass in heave, $A_{33}(\omega)$ compared with WAMIT

## 3.6 Diffraction Problem in a Monochromatic Incident Wave

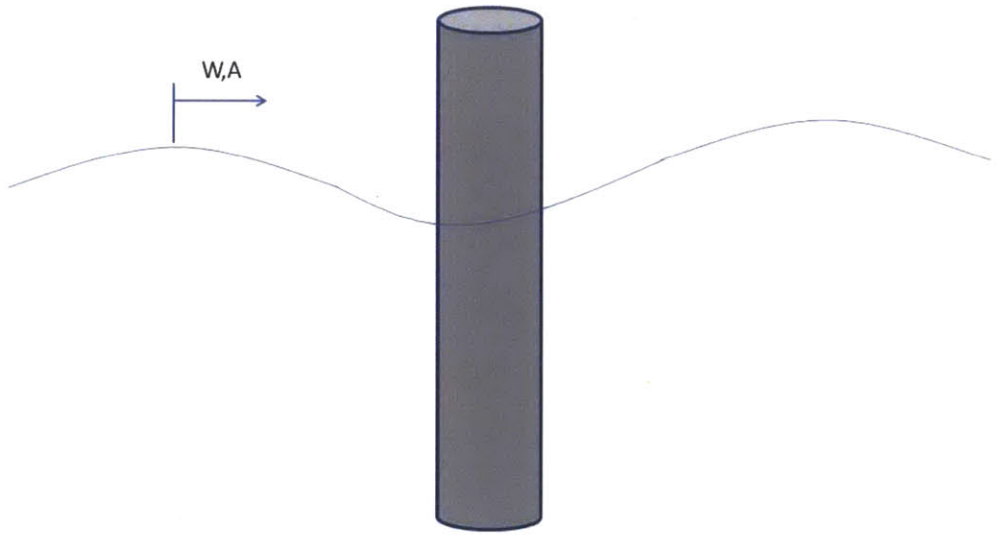


Figure 3-19: Test case - Diffraction problem in a monochromatic incident wave (Radius=2m; Draft=10m; A=1m)

$$\vec{F}(t) = -\rho \frac{d}{dt} \oint_{S_B^I(t)} \varphi_I \vec{n} ds - \rho \frac{d}{dt} \int_{S_B^I(t)} \varphi_D \vec{n} ds - \rho g \oint_{S_B^I(t)} Z \vec{n} ds$$

where $\varphi_D$ is obtained by the time-domain 3D potential-flow simulation based on a transient free-surface Green-function method; $S_B^I(t)$ is the instantaneous body surface under the ambient wave.

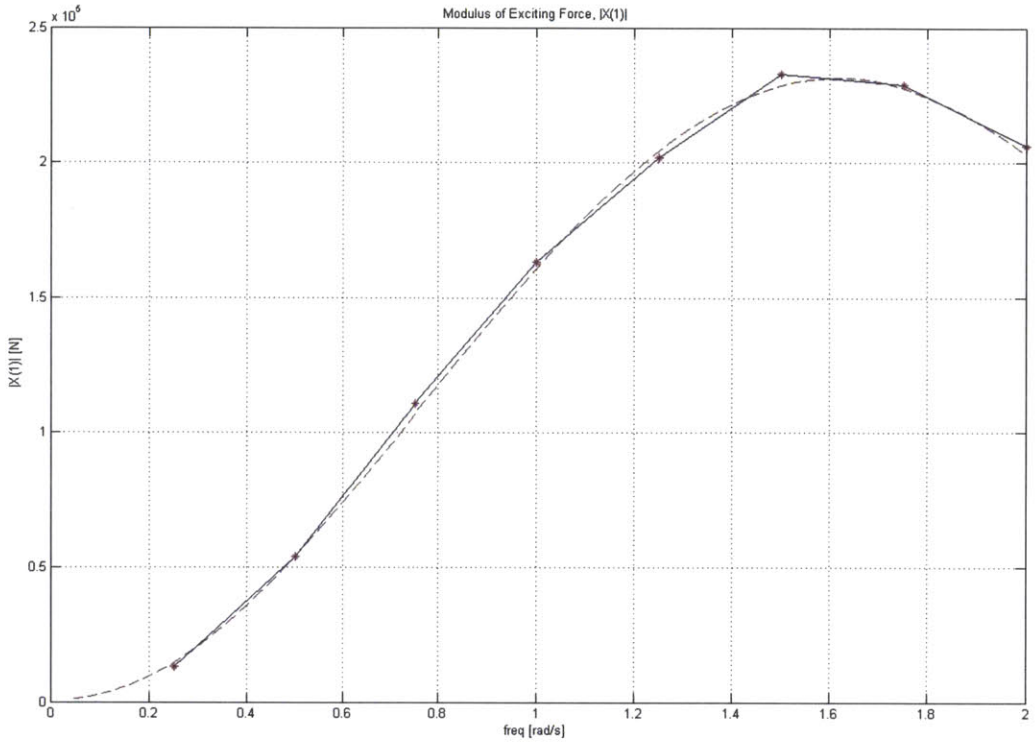


Figure 3-20: Wave exciting force in surge, $X_1(\omega)$ compared with WAMIT

## 3.7 Diffraction Problem in a Nonlinear Large Amplitude Incident Wave

Based on the numerical treatment of the nonlinear free-surface condition and the Weak-Scatterer hypothesis, all of which are addressed in Chapter 2, a nonlinear large amplitude wave-body interaction problem is simulated to obtain the disturbance velocity potential and the disturbance free-surface elevation which by definition satisfies the linear free-surface condition on the incident wave free-surface at z= $\zeta(t)$ . The numerical scheme has been partially vectorized and optimized to provide accurate solutions in an efficient manner from the computational perspective. Case simulations are presented for a fixed body in large amplitude incident waves defined as a nonlinear diffraction problem. It is also compared with the linear wave analysis method which is based on the linear free-surface conditions on the z=0 plane for unit wave amplitude.

$$\vec{F}(t) = -\rho \frac{d}{dt} \oint_{S_B^I(t)} \varphi_I \vec{n} ds - \rho \frac{d}{dt} \int_{S_B^I(t)} \varphi_D \vec{n} ds - \rho g \oint_{S_B^I(t)} Z \vec{n} ds \tag{3.8}$$

where $\varphi_D$ is obtained by the time-domain 3D potential-flow simulation based on a transient free-surface Green-function method; $S_B^I(t)$ is the instantaneous body surface under the ambient wave.

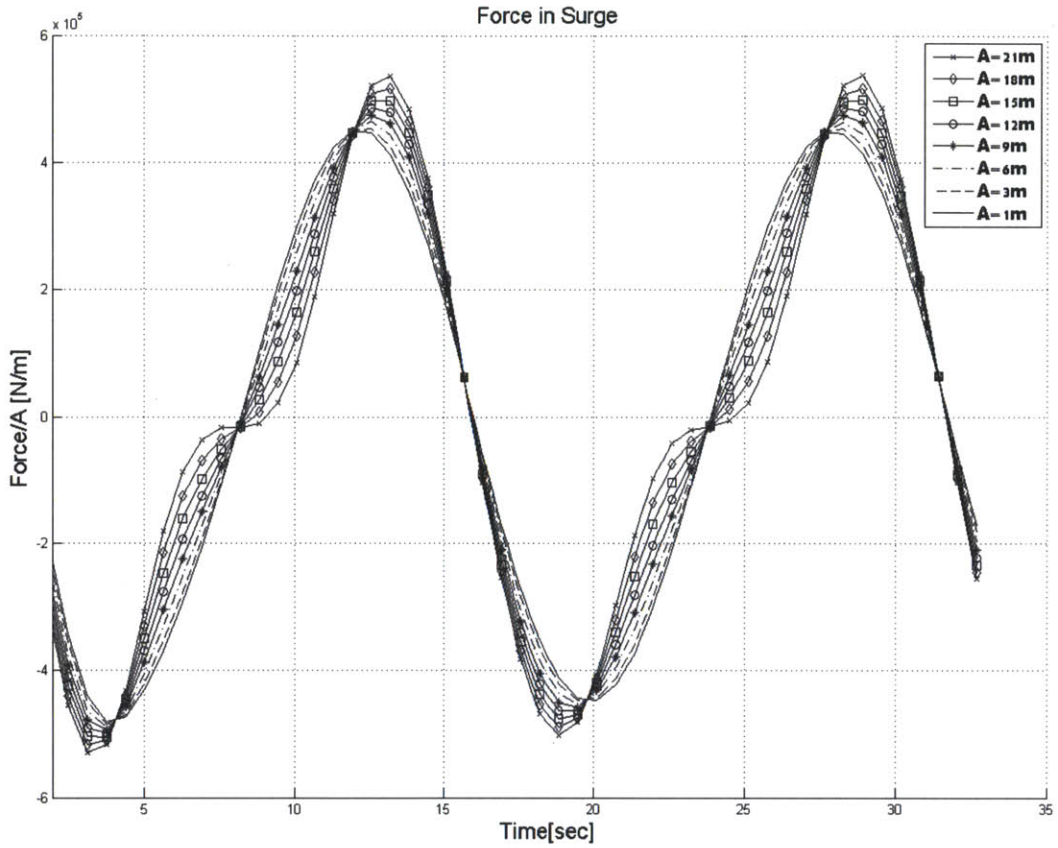


Figure 3-21: Case simulations for a fixed body in large amplitude incident waves (nonlinear diffraction problem)

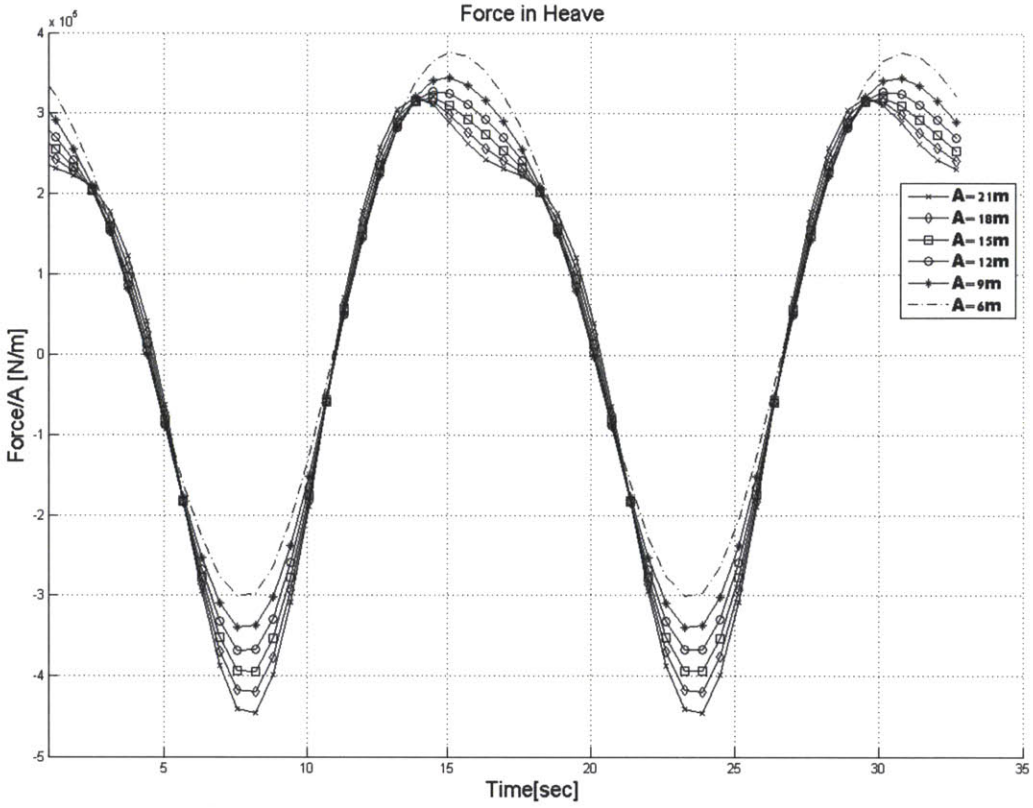


Figure 3-22: Case simulation for a fixed body in large amplitude incident waves (nonlinear diffraction problem)

## 3.8 Weak-Scatterer Condition Study

As addressed in the order-of-magnitude analysis in section 2.6, the free-surface contributions are small compared to the body-surface contributions. Again, the relative significance of those free-surface contributions on the hydrodynamic force on floating bodies will depend on the ambient wave steepness $kA$ and the relative body dimension $kd$.

In the weak-scatterer condition where the $kA$ and $kd$ are defined as sufficiently small, the hydrodynamic force on floating bodies will be dominated by the body surface contribution obtained by the nonlinear Froude-Krylov force, the nonlinear disturbance force and the nonlinear hydrostatic force. This will introduce a new way of modeling the hydrodynamic force on floating bodies that is efficient and accurate.

Under the weak-scatterer condition, the hydrodynamic force on a floating body is obtained by taking the time rate of change of the impulse of velocity potential around the body. The total fluid force on the body takes the form

$$-\rho\frac{d}{dt}\oint_{S_B^I(t)}\varphi_I\bar{n}ds-\rho\frac{d}{dt}\int_{S_B^I(t)}\varphi_D\bar{n}ds-\rho g\oint_{S_B^I(t)}Z\bar{n}ds \tag{3.9}$$

where $\varphi_D$ is obtained by the time-domain 3D potential-flow simulation based on a transient free-surface Green-function method; $S_B^I(t)$ is the instantaneous body surface under the ambient wave.

Recalling the derivation presented in Chapter 2, the horizontal and vertical free-surface impulse force in the x and z directions respectively take the form

$$F_{X-FS} = \rho \frac{d}{dt} \int_{S_E^I(t)} \left[ \varphi_D \frac{\partial \zeta_I}{\partial X} - \zeta_D \frac{\partial}{\partial X}(\varphi_I + \varphi_D) \right] ds$$
$$F_{Z-FS} = -\rho \int_{S_E^I(t)} \left[ \frac{\partial \varphi_D}{\partial t} + g\zeta_D + \frac{\partial \zeta_I}{\partial t} \frac{\partial \varphi_D}{\partial Z} + \zeta_D \frac{\partial^2 \varphi_I}{\partial Z \partial t} \right] ds \tag{3.10}$$

For the purpose of differentiating those two distinct forces during the following weak-scatterer condition study, the approximate force under the weak-scatterer condition in Eq. (3.9) is referred to as the 'Weak-Scatter Force', the free surface force in Eq. (3.10) is referred to as the 'Residual Force', and the exact total force which is defined by the sum of those two forces is referred to as the 'Total Force'.

### 3.8.1 Case Studies for Wave Steepness ($kA$) and Body Dimension ($kd$)

The nonlinear wave-body interaction simulation is carried out to demonstrate the relative significance of the free-surface impulse from the body surface impulse for various wave conditions in terms of wave steepness $kA$'s and the body dimensions $kd$'s.

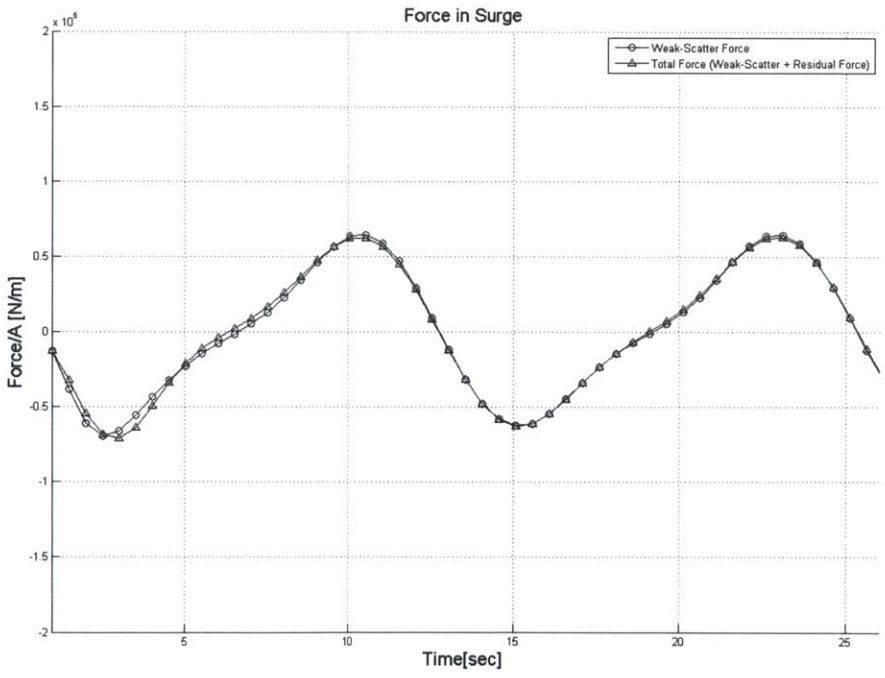


Figure 3-23: Nonlinear diffraction force in surge for an incident wave ($kA$=0.1; $kd$=0.1)

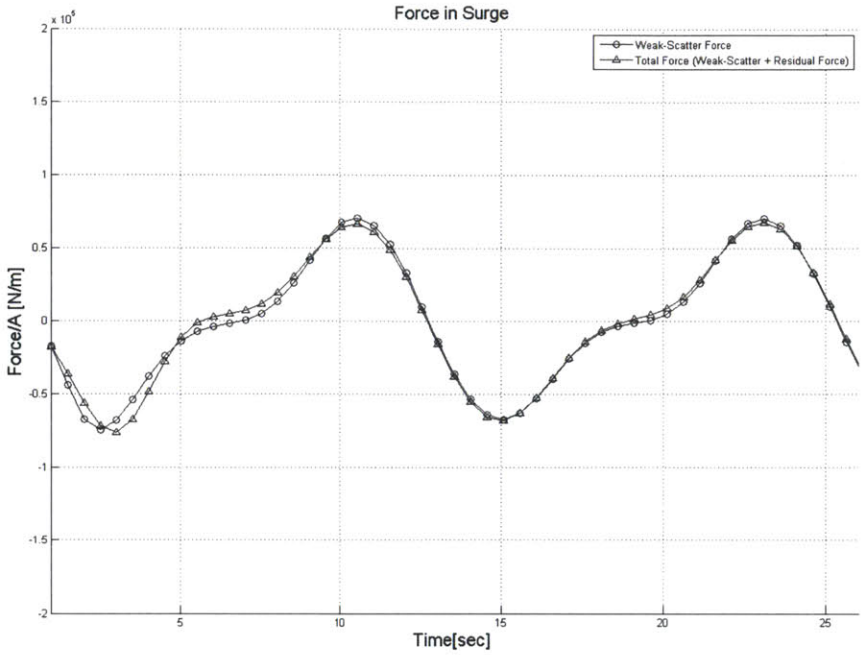


Figure 3-24: Nonlinear diffraction force in surge for an incident wave ( $kA$ =0.15; $kd$ =0.1) ( ○ Weak-Scatter Force; △ Total Force)

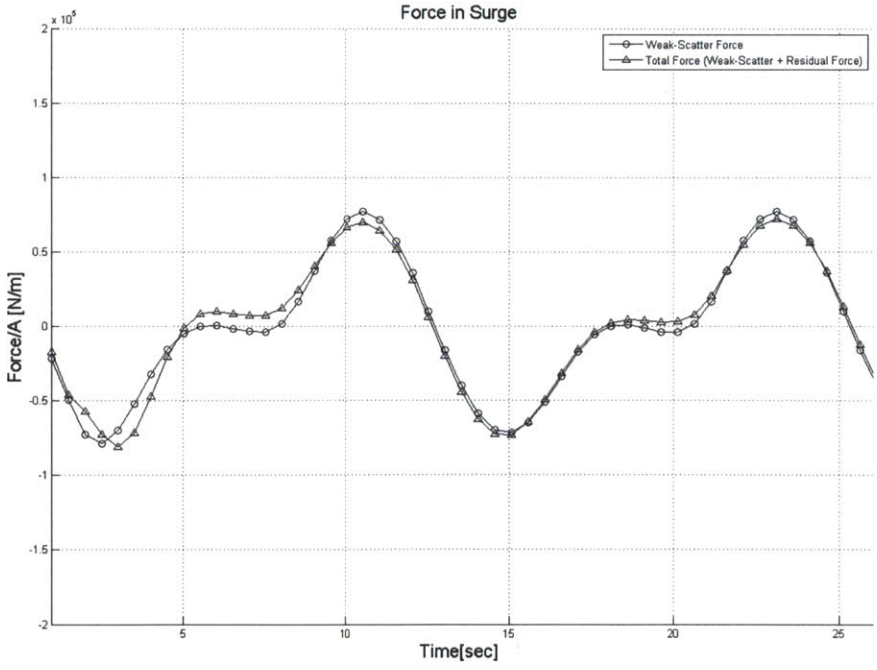


Figure 3-25: Nonlinear diffraction force in surge for an incident wave ( $kA$ =0.2; $kd$ =0.1)

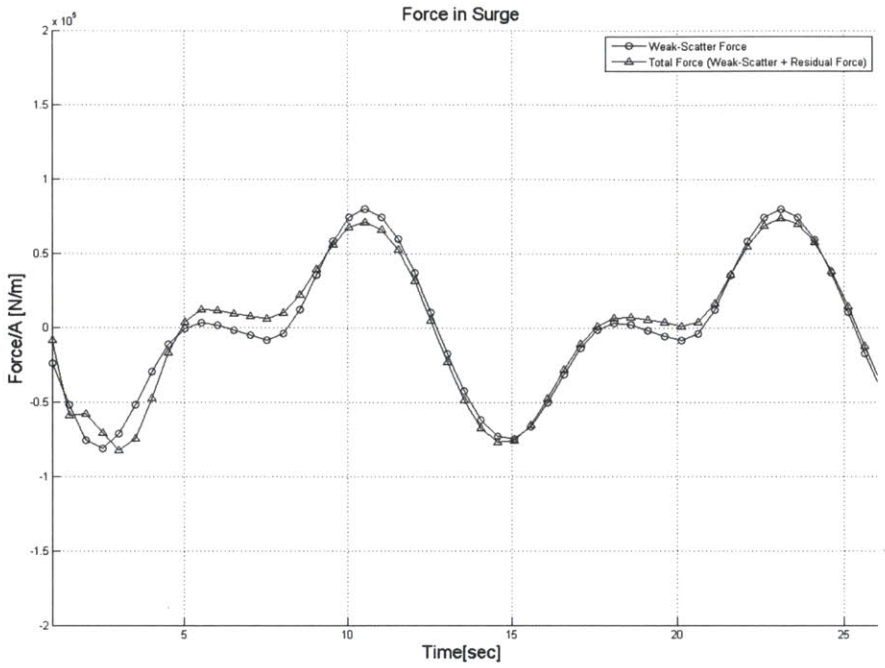


Figure 3-26: Nonlinear diffraction force in surge for an incident wave ( $kA$ =0.225; $kd$ =0.1) ( ○ Weak-Scatter Force; △ Total Force)

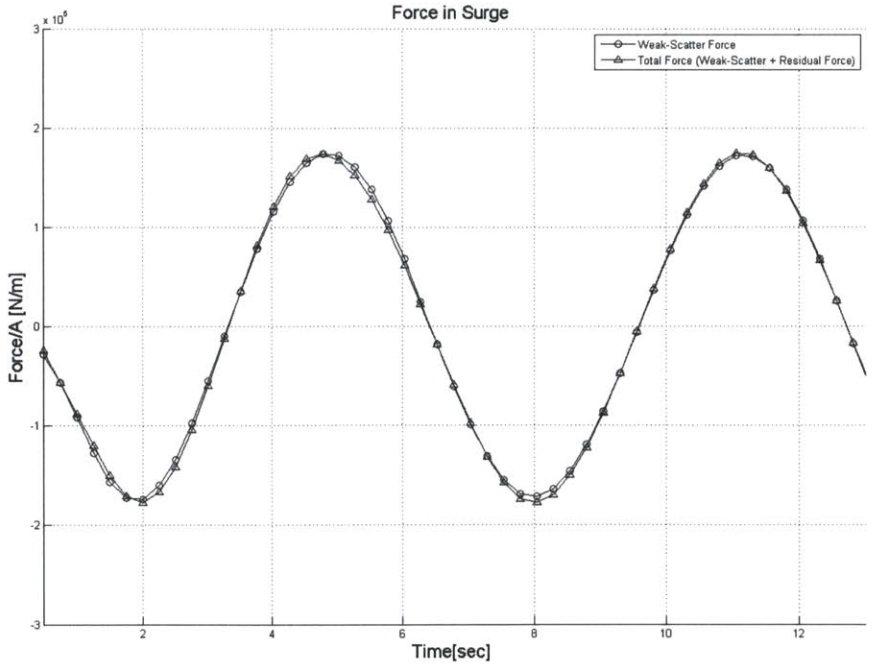


Figure 3-27: Nonlinear diffraction force in surge for an incident wave ( $kA$ =0.05; $kd$ =0.4)

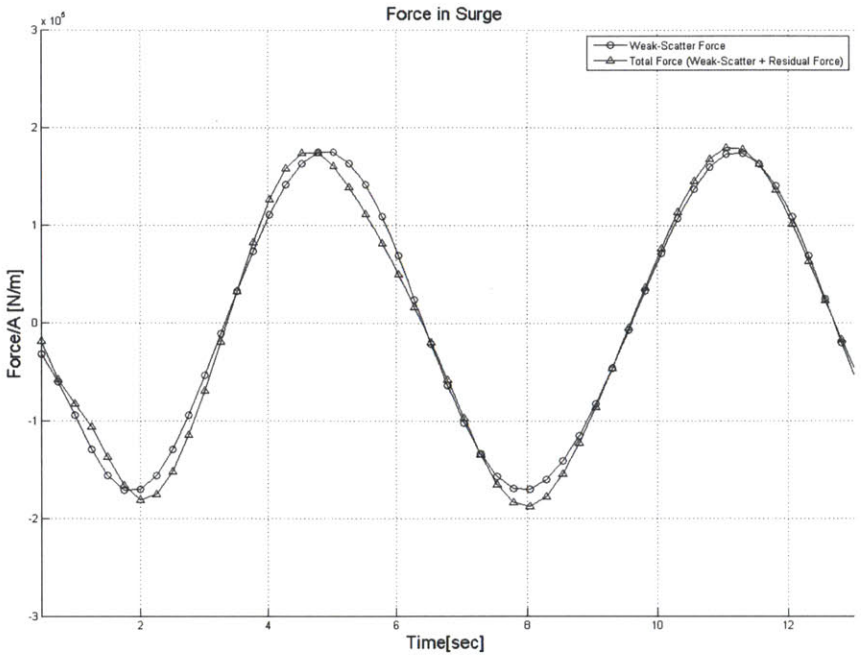


Figure 3-28: Nonlinear diffraction force in surge for an incident wave ( $kA$ =0.15; $kd$ =0.4)

( ○ Weak-Scatter Force; △ Total Force)

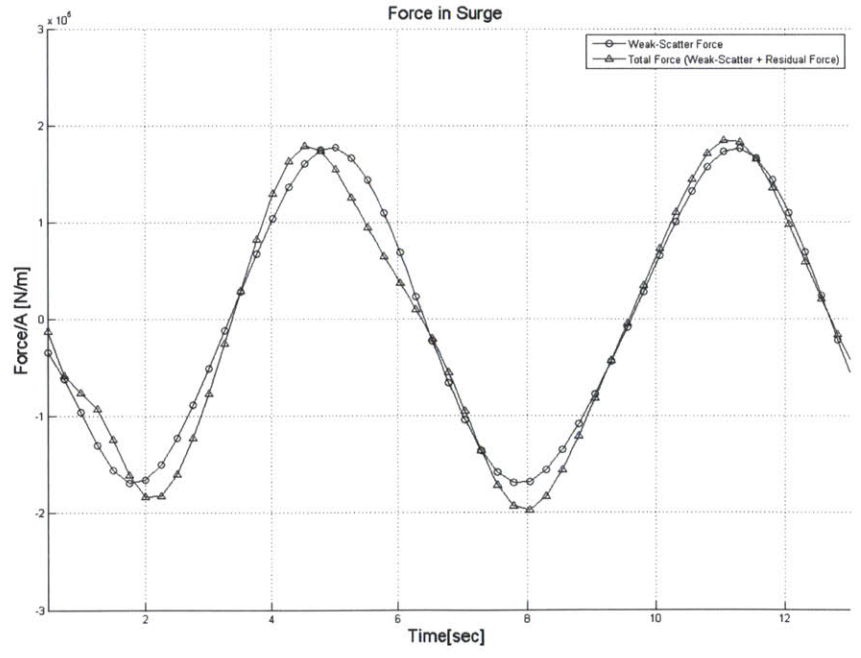


Figure 3-29: Nonlinear diffraction force in surge for an incident wave ( $kA$ =0.25; $kd$ =0.4)

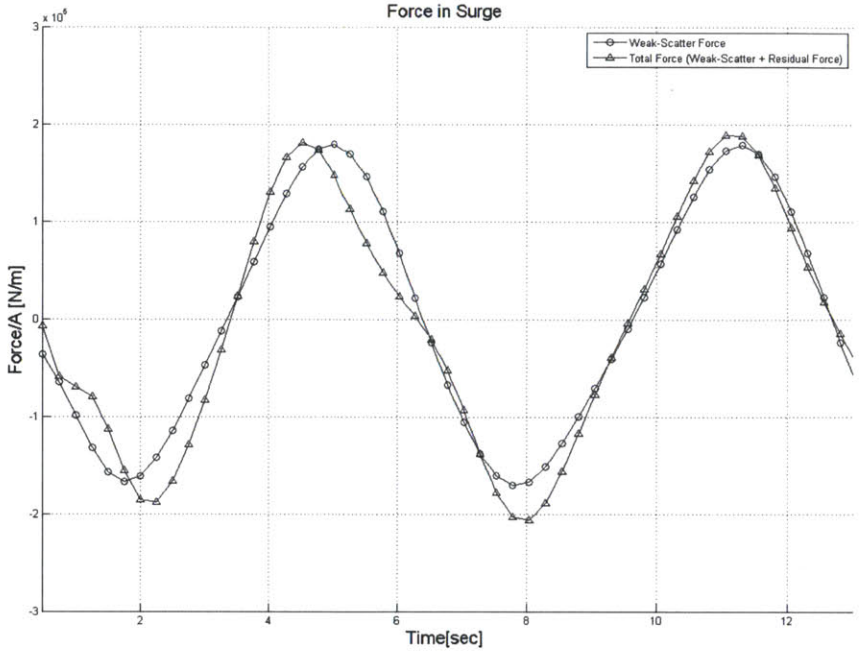


Figure 3-30: Nonlinear diffraction force in surge for an incident wave ( $kA$ =0.35; $kd$ =0.4)

( ○ Weak-Scatter Force; △ Total Force)

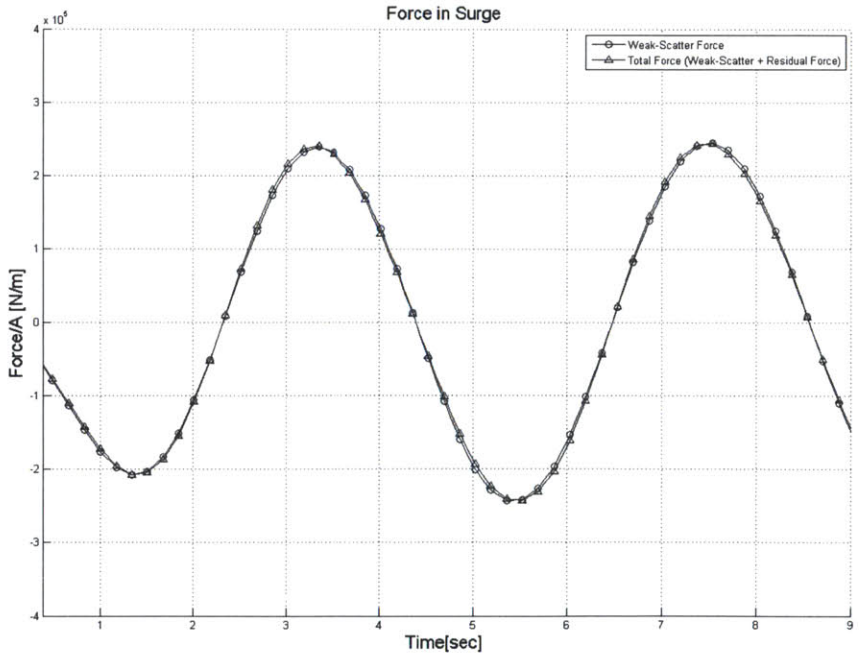


Figure 3-31: Nonlinear diffraction force in surge for an incident wave ( $kA$ =0.05; $kd$ =0.9)

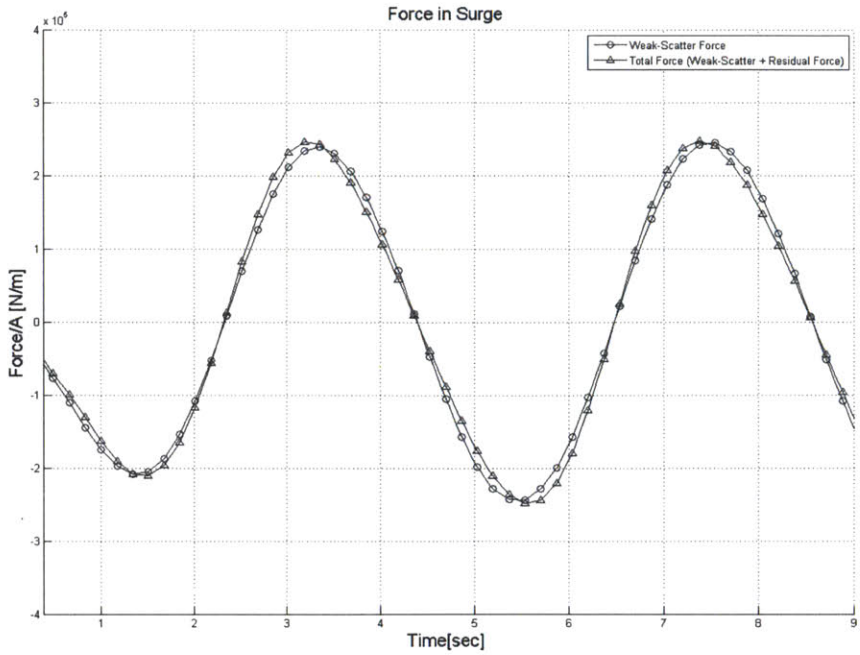


Figure 3-32: Nonlinear diffraction force in surge for an incident wave ( $kA$ =0.15; $kd$ =0.9)

( ○ Weak-Scatter Force; △ Total Force)

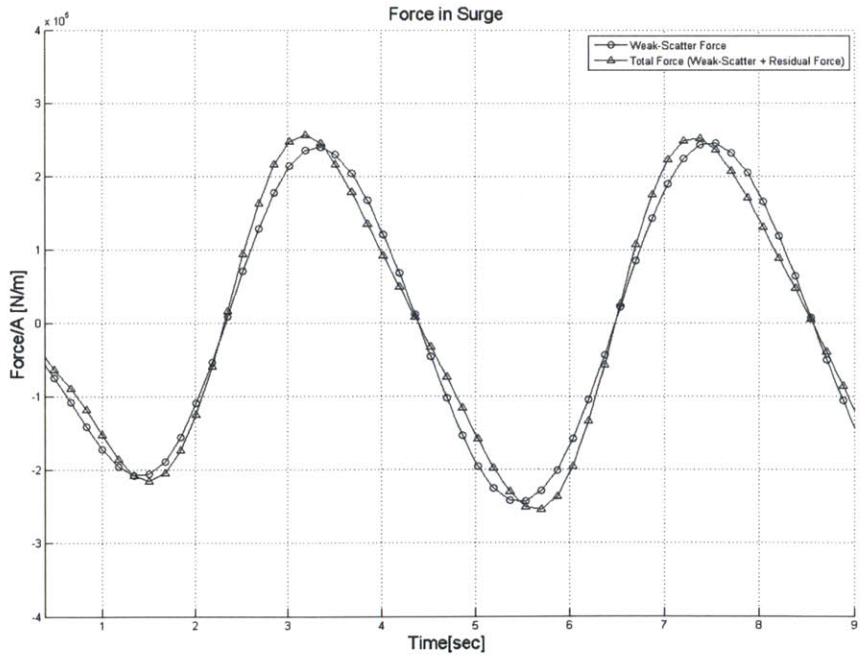


Figure 3-33: Nonlinear diffraction force in surge for an incident wave ( $kA$ =0.25; $kd$ =0.9)

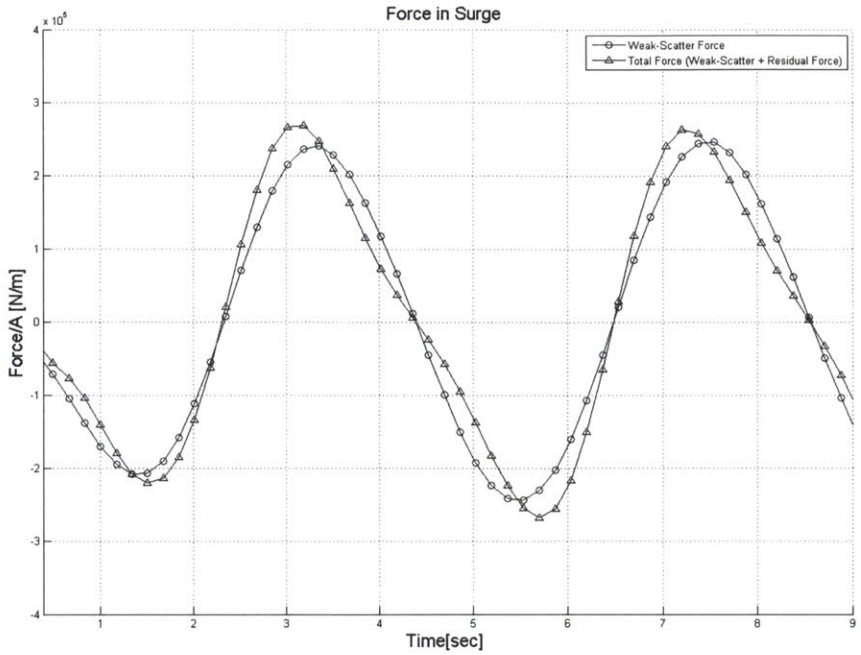


Figure 3-34: Nonlinear diffraction force in surge for an incident wave

($kA$=0.35; $kd$=0.9)

(○ Weak-Scatter Force; △ Total Force)

### 3.8.2 Global Study for Weak-Scatterer Condition

The weak-scatterer condition has been explored over a wide range of wave steepnesses, $kA$'s, and the relative body dimensions, $kd$'s. The mean error is defined by the mean value of the fractional difference from the Total Force as follows.

$$\bar{e} \triangleq \int_{T}^{2T} \left| \frac{g(t) - f(t)}{f(t)} \right| dt \Big/ T \tag{3.11}$$

where $\bar{e}$ is the mean error between the Weak-Scatter Force and the Total Force; $g(t)$ is the Weak-Scatter Force; $f(t)$ is the Total Force

The mean value of the fractional difference from the Total Force is a good indicator for the accuracy of the weak-scatterer condition in a nonlinear wave-body interaction problem. A small fractional error indicates that the body-impulse contribution dominates the wave force on the body, whereas a larger fractional error indicates that the free-surface contribution may need to be taken into account in the wave force calculation.

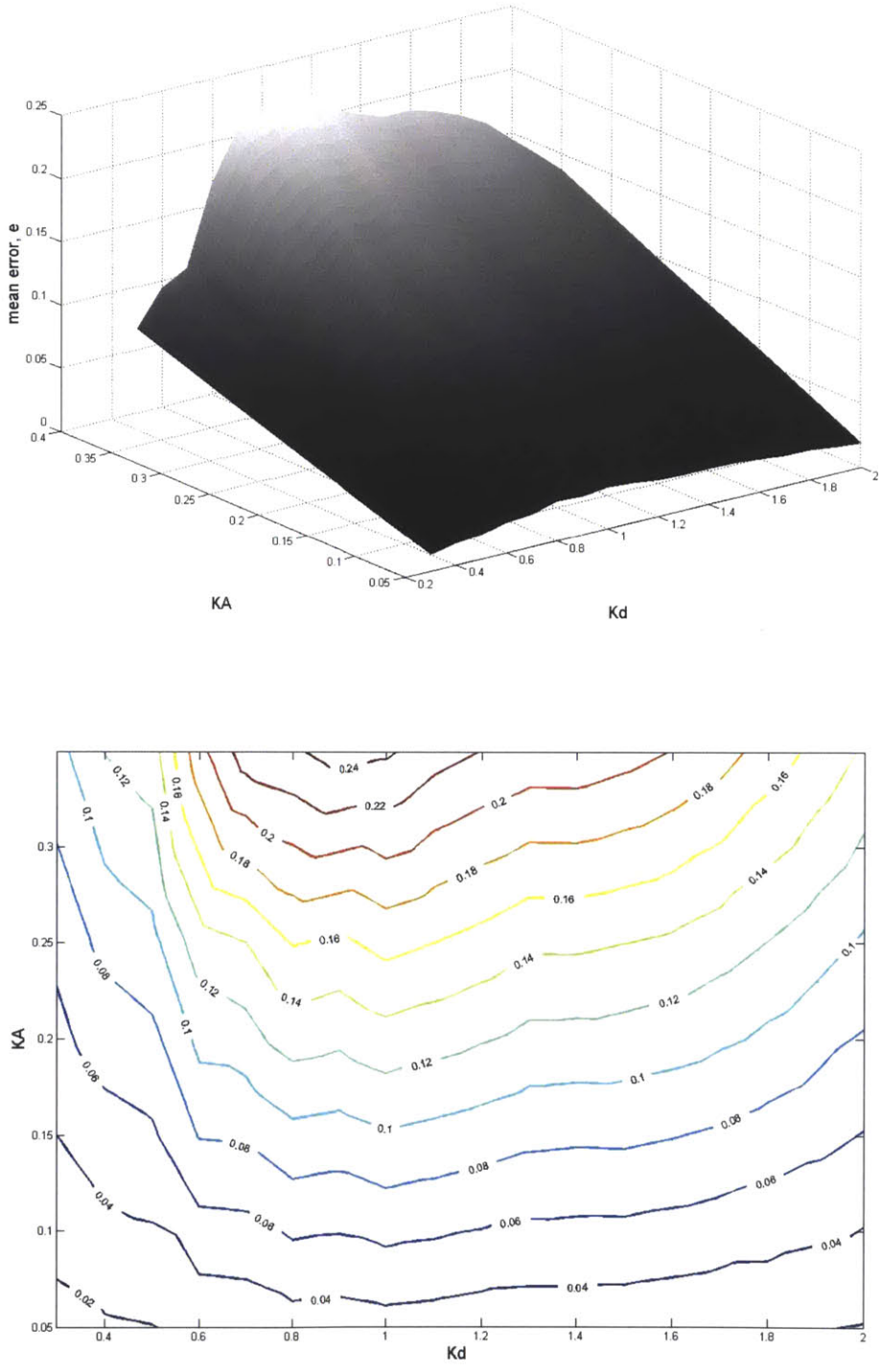


Figure 3-35: Mean error $\bar{e}$ between the Weak-Scatter Force and the Total Force in a nonlinear diffraction problem over various wave conditions ( $kA$ , $kd$ )

## 3.9 Time-Domain Simulation of Floating Wind Turbines for Extreme Wave Events

### 3.9.1 Numerical Time Marching of Equations of Motion

The time integration of equations of motion in the time domain requires an accurate, efficient and robust time-marching scheme to obtain the system response at each time step. It can be carried out by a variety of standard schemes including Euler's method, Runge-Kutta methods, multi-step predictor corrector methods of the Adams type etc. Because of its robustness to the time step uniformity, Runge-Kutta methods have been taken as the time marching scheme for the present work.

Runge-Kutta methods achieve the accuracy of a Taylor series approach without requiring the calculation of higher derivatives. Many variations exist but all can be cast in the generalized form as follows.

$$y_{i+1} = y_i + S(x_i, y_i, h)h$$

where $S$ is an increment function, which can be interpreted as a representative slope over the interval.

The increment function can be written in general form as follows:

$$S = a_1 k_1 + a_2 k_2 + ... + a_n k_n$$

where the $a$'s are constants and the $k$'s are

$$k_1 = f(x_i, y_i)$$
$$k_2 = f(x_i + p_1 h, y_i + q_{11} k_1 h)$$
$$k_3 = f(x_i + p_2 h, y_i + q_{21} k_1 h + q_{22} k_2 h)$$
$$\cdot$$
$$\cdot$$
$$k_n = f(x_i + p_{n-1} h, y_i + q_{n-1,1} k_1 h + q_{n-1,2} k_2 h + ... + q_{n-1,n-1} k_{n-1} h)$$

where the $p$'s and $q$'s are constants. The $k$'s are recurrence relationships. That is, $k_1$ appears in the equation for $k_2$, which appears in the equation for $k_3$, and so forth.

Various types of Runge-Kutta methods can be devised by employing different numbers of terms in the increment function as specified by n. The first order Runge-Kutta method with n=1 is in fact Euler's method. Once n is chosen, values for the a's and p's and q's are evaluated properly and used to compute the increment function thereafter.

In a nonlinear wave-body hydrodynamic interaction problem in the time domain, the computation of wave force on the body involves convolution integrals which are imposing a significant computational cost. For this, it is not desired to use too small a time step size or a higher order method. In our experience from numerous test simulations, second order method is sufficient and a higher order method is offset by the additional computational effort and complexity.

The second order Runge-Kutta method is adopted as the time marching scheme in the present analysis and simulation. It is actually equivalent to Heun's Method with a single corrector (a2=1/2). With a2 assumed to be ½, it yields

$$y_{i+1} = y_i + (\frac{1}{2}k_1 + \frac{1}{2}k_2)h \tag{3.12}$$

where

$$k_1 = f(x_i, y_i)$$
$$k_2 = f(x_i + h, y_i + k_1 h)$$

For a free motion response simulation in a fully nonlinear hydrodynamic wave-body interaction problem, the wave forces on the floating body are implicitly coupled with the time history of body boundary conditions. In other words, the external force on the right hand side of the equations of motion is a function of its solutions. Numerical errors on the discrete time derivative of the fluid impulse, which may get amplified and grow over time. A very small time-step size may resolve this problem but it's not desired because of the computational burden, which primarily arises from the evaluation of memory effects. The present work adopts a curve-fitting approach to smooth the impulse of the velocity potential over a certain time period. A polynomial curve fitting is employed at each time step to fit the velocity-potential-impulse data-points over the five prior time-steps backward from the current time-step.

The floater is stationary with zero initial conditions to minimize the transient responses for the early time period in particular.

$$\xi_1(t) = 0$$
$$\dot{\xi}_1(t) = 0 \text{, at t=0}$$
$$\ddot{\xi}_1(t) = 0$$

The initial transients are found to produce a large oscillatory hydrodynamic force over the initial time period, which dies down thereafter. These oscillations may be reduced by a ramp function used for the incident wave potential over the initial time period which is equivalent to introducing the incident ambient wave gradually in the fluid domain. The long-term steady state result however may not be influenced by this ramp function regardless of its type and application time-period. The incident ambient wave field is started from a state of rest at t=0 and is ramped up to the fully developed state as follows.

$$\begin{aligned} \zeta_I(t) &= (1-\exp(\alpha t))\cdot\zeta_{I_o}(t) \\ \varphi_I(x,y,z,t) &= \left(1-\exp(\alpha t)\right)\cdot\varphi_{I_o}(x,y,z,t) \end{aligned} \text{, for t<T} \qquad (3.13)$$

where $\left(1-\exp(\alpha t)\right)$ is a ramp function with $\alpha = \log(0.02)/T$.

### 3.9.2 Transient Response to Initial Conditions

With the computational ability to evaluate the hydrodynamic forces for large amplitude waves and large amplitude body motions in the time domain, the dynamic responses of motions and line tensions can be obtained by a direct integration of equations of motion as presented in the previous chapter.

To validate the numerical scheme and solver, the transient response simulation is performed by releasing the floating wind turbine from rest with a given initial displacement in $\theta$.

As a test, a separate simulation was performed, referred to as 'Linear Body'. As opposed to the fully nonlinear simulation which allows the underwater body geometry to change as the body moves, the Linear Body method takes a linear free surface condition at mean surface at z=0 and a linear body boundary condition at mean position of the body at x=0. That is, the numerical body geometry remains uniform over time and the body boundary condition is applied on this stationary body panels.

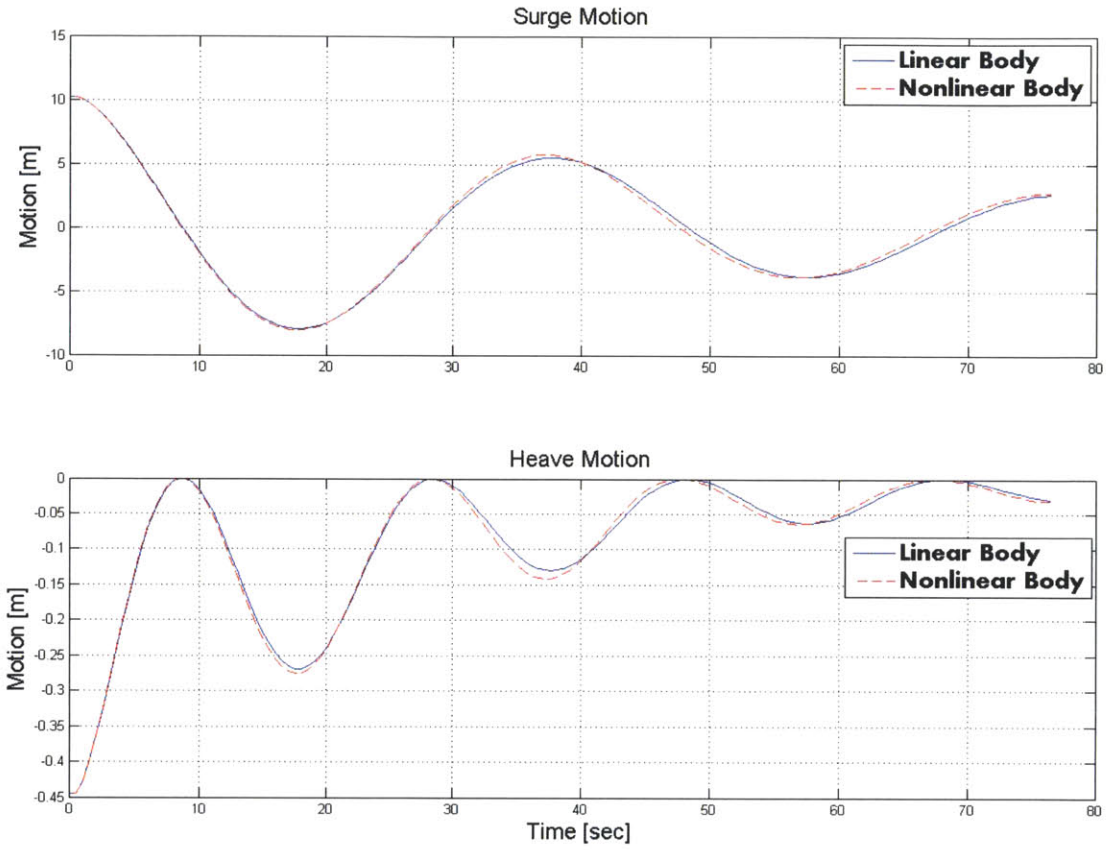


Figure 3-36: Initial condition response for floating wind turbine released from rest with an initial displacement. (—— Linear Body; ·····Nonlinear Body)

The results are indistinguishable. The difference in amplitudes is small overall. However it is interesting to note that the oscillation periods of the nonlinear method are a bit shorter than the linear method's results. This is caused by the competing effects of the increases in added mass and buoyancy force due to large motions in time. A large motion in heave yields larger added masses over time and it increases the oscillation period. It, however, yields larger buoyancy

forces (hydrostatic restoring), which tend to decrease the period of oscillation. Since the effect from the increase in restoring forces is greater in this case, the decrease in natural period is observed. This reveals the importance of nonlinear body geometry effects.

### 3.9.3 Large-Amplitude Wave Loads Response

Simulations are carried out for a large amplitude wave to address the nonlinear hydrodynamic forces and the resultant nonlinear dynamic responses of floater motions, tether tensions and anchor loads. Case runs are carried out for three different incident waves: wave amplitudes A of 1m, 6m and 10m with a frequency of 0.5 rad/sec.

In contrast, I have also included the strip theory predictions which are obtained by the linear equations of motion and the GI-Taylor approximation method as presented in section 2.6

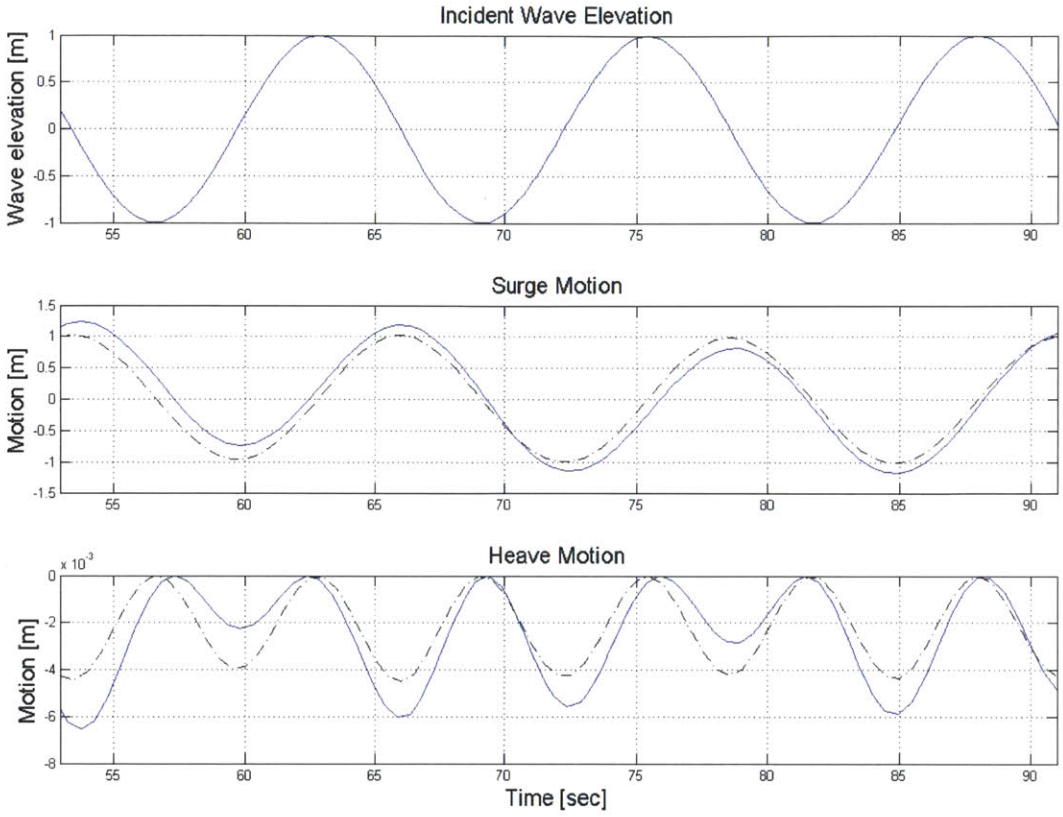


**(Solid line: Nonlinear analysis; Dashed line: Linear analysis)**

Figure 3-37: Incident wave elevation ($\zeta_1$) from the mean waterline; Motion in surge ($\xi_1$); Motion in heave ($\xi_3$) for incident wave of A=1m and w=0.5 rad/sec.

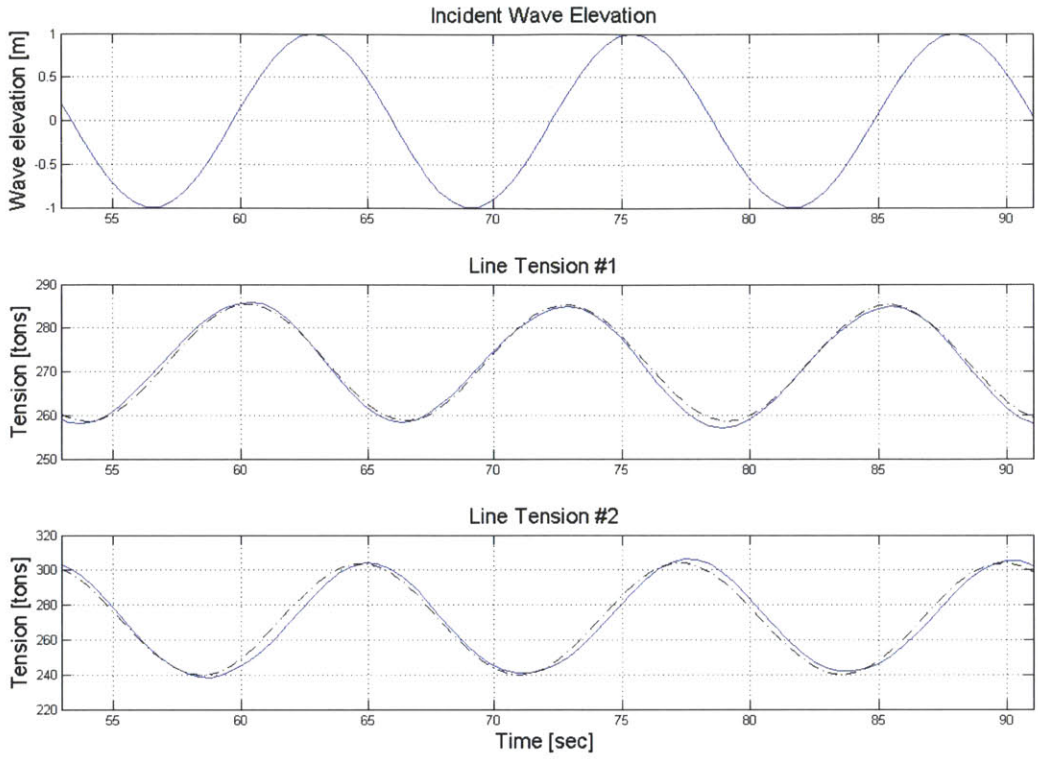


**(Solid line: Nonlinear analysis; Dashed line: Linear analysis)**

Figure 3-38: Incident wave elevation ($\zeta_I$) from the mean waterline; Tension of line#1 ($T_1^*$); Tension of line#2 ($T_2$) for incident wave of A=1m and w=0.5 rad/sec.

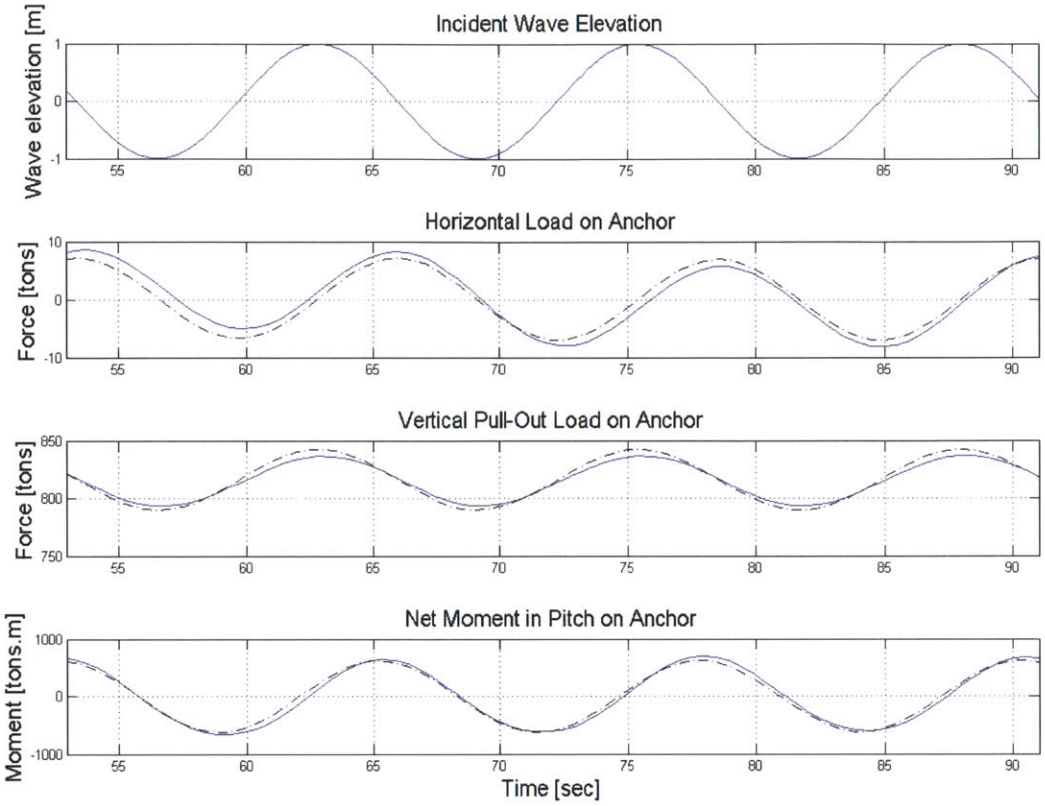


**(Solid line: Nonlinear analysis; Dashed line: Linear analysis)**

Figure 3-39: Incident wave elevation ($\zeta_I$) from the mean waterline; Horizontal load on anchor; Vertical pull-out load on anchor; Net moment in pitch on anchor for incident wave of A=1m and w=0.5 rad/sec.

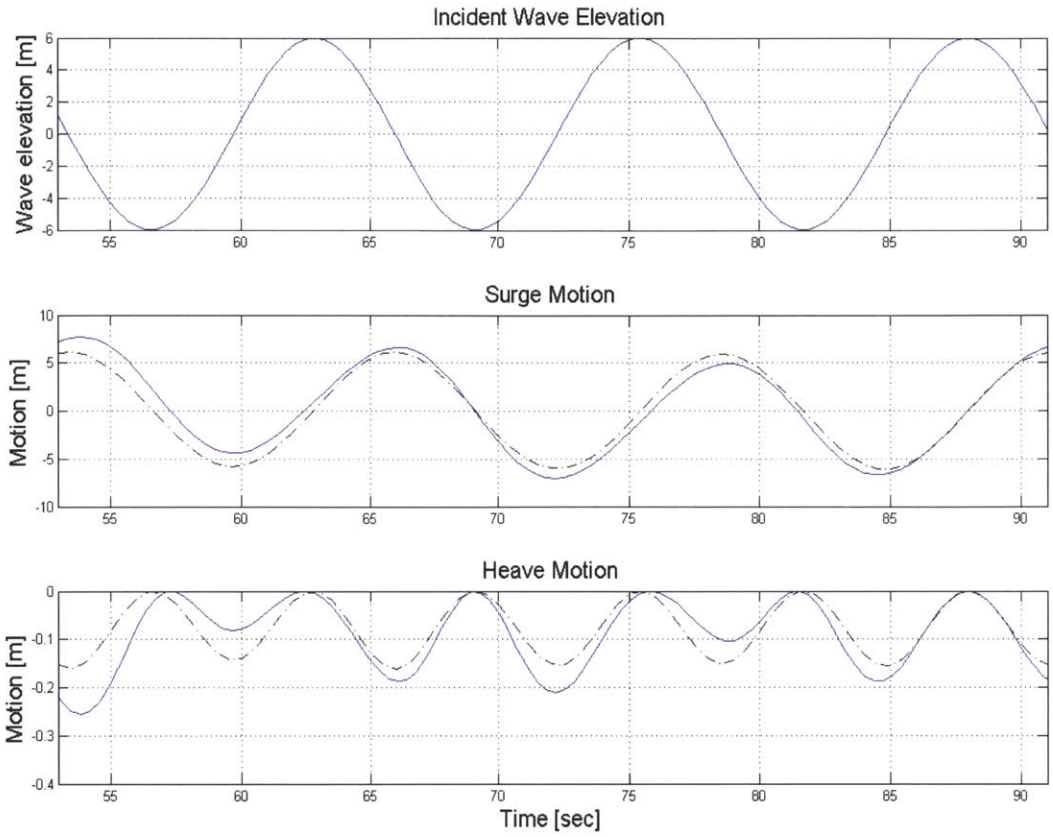


**(Solid line: Nonlinear analysis; Dashed line: Linear analysis)**

Figure 3-40: Incident wave elevation ($\zeta_I$) from the mean waterline; Motion in surge ($\xi_1$); Motion in heave ($\xi_3$) for incident wave of A=6m and w=0.5 rad/sec.

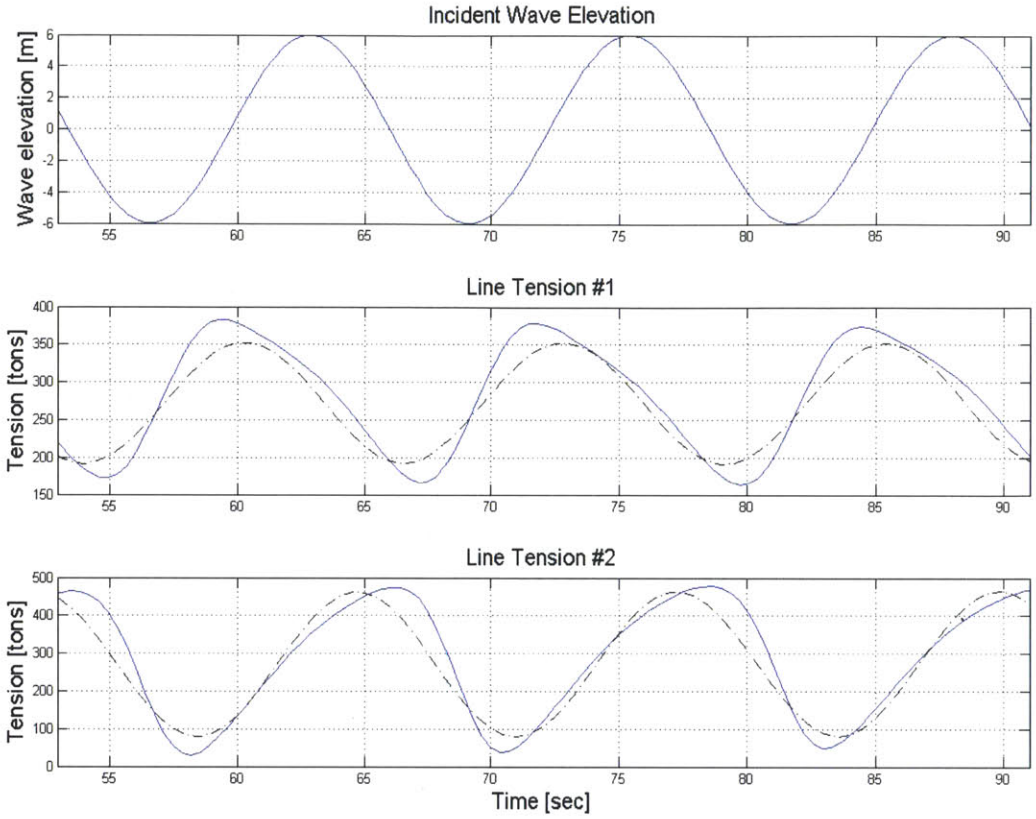


**(Solid line: Nonlinear analysis; Dashed line: Linear analysis)**

Figure 3-41: Incident wave elevation ($\zeta_1$) from the mean waterline; Tension of line#1 ($T_1^*$); Tension of line#2 ($T_2$) for incident wave of A=6m and w=0.5 rad/sec.

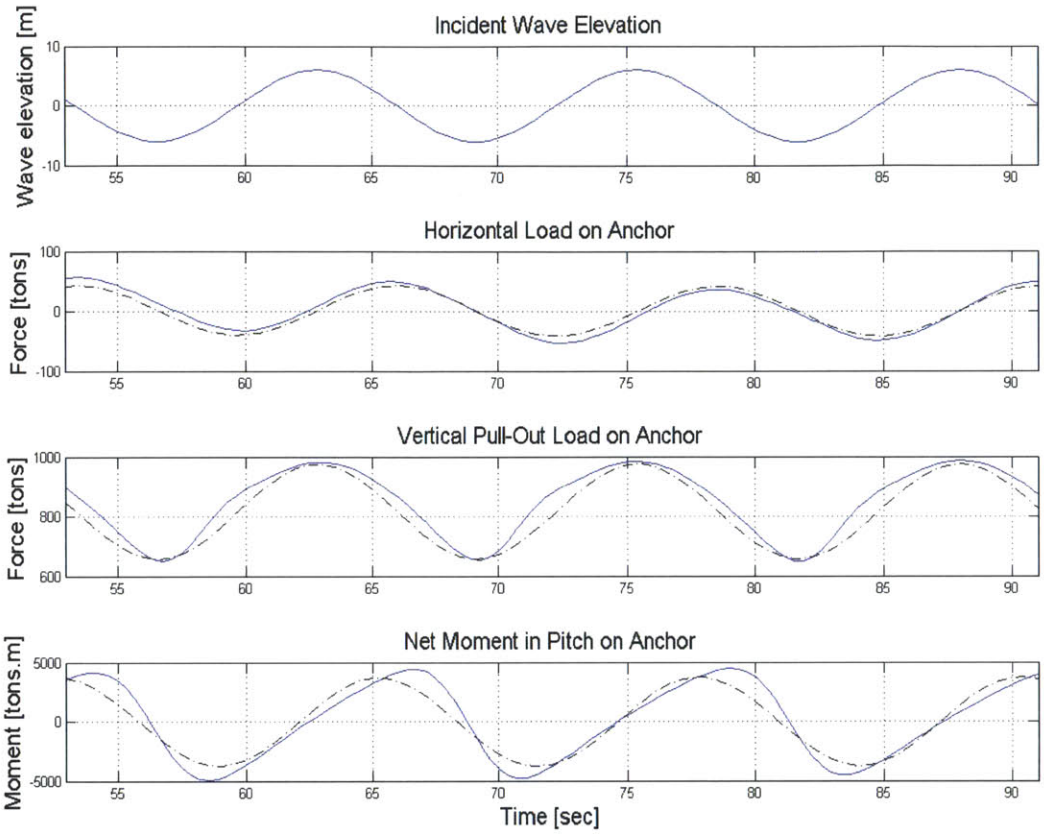


**(Solid line: Nonlinear analysis; Dashed line: Linear analysis)**

Figure 3-42: Incident wave elevation ($\zeta_I$) from the mean waterline; Horizontal load on anchor; Vertical pull-out load on anchor; Net moment in pitch on anchor for incident wave of A=6m and w=0.5 rad/sec.

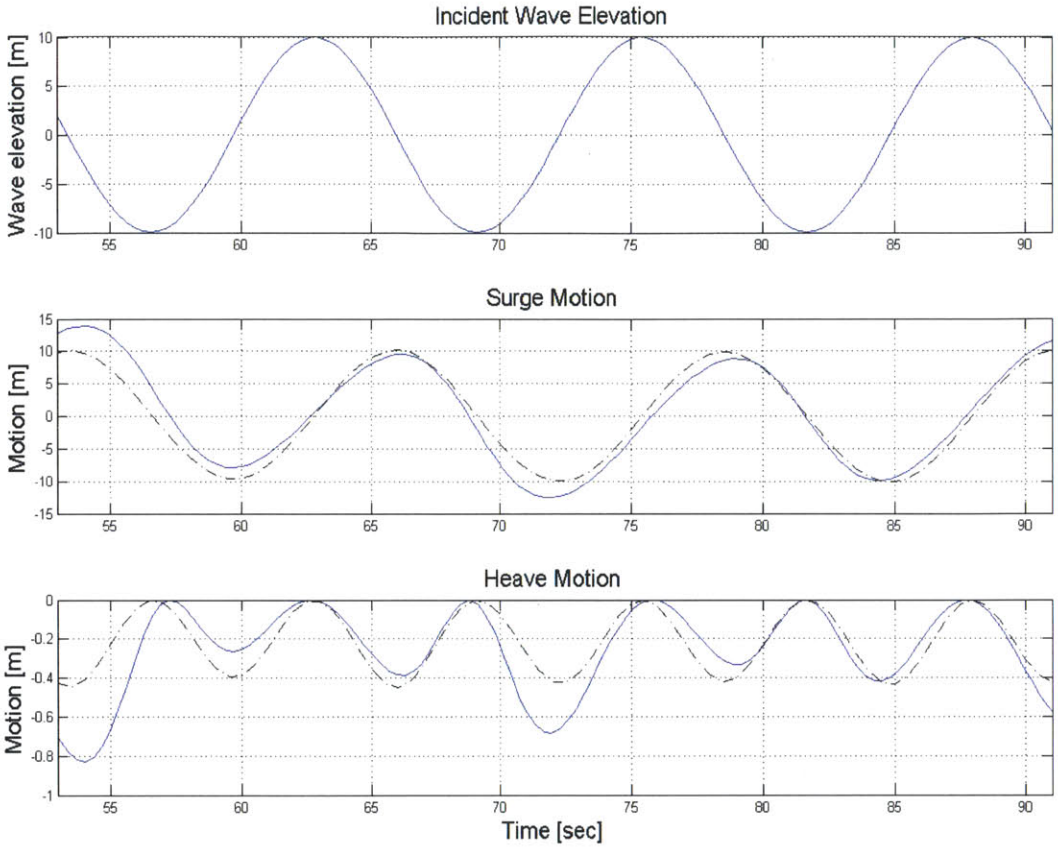


Figure 3-43: Incident wave elevation ($\zeta_I$) from the mean waterline; Motion in surge ($\xi_1$); Motion in heave ($\xi_3$) for incident wave of A=10m and w=0.5 rad/sec.

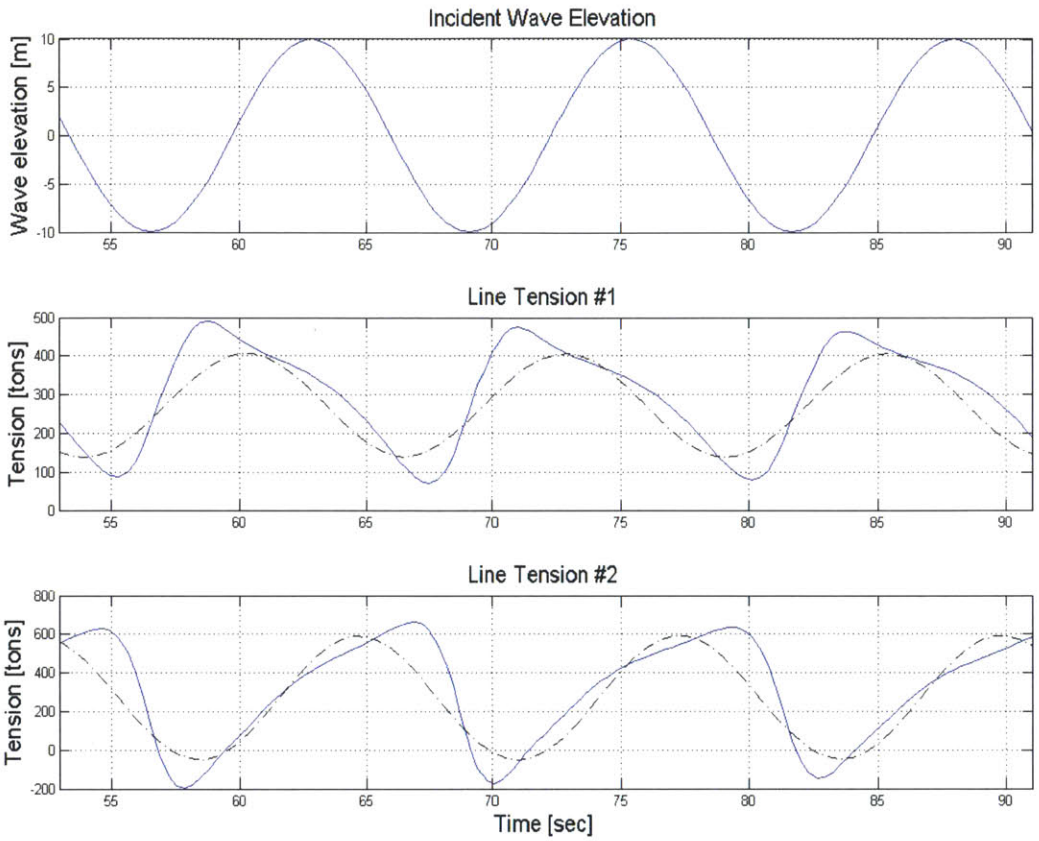


Figure 3-44: Incident wave elevation ($\zeta_1$) from the mean waterline; Tension of line#1 ($T_1^*$); Tension of line#2 ($T_2$) for incident wave of A=10m and w=0.5 rad/sec.

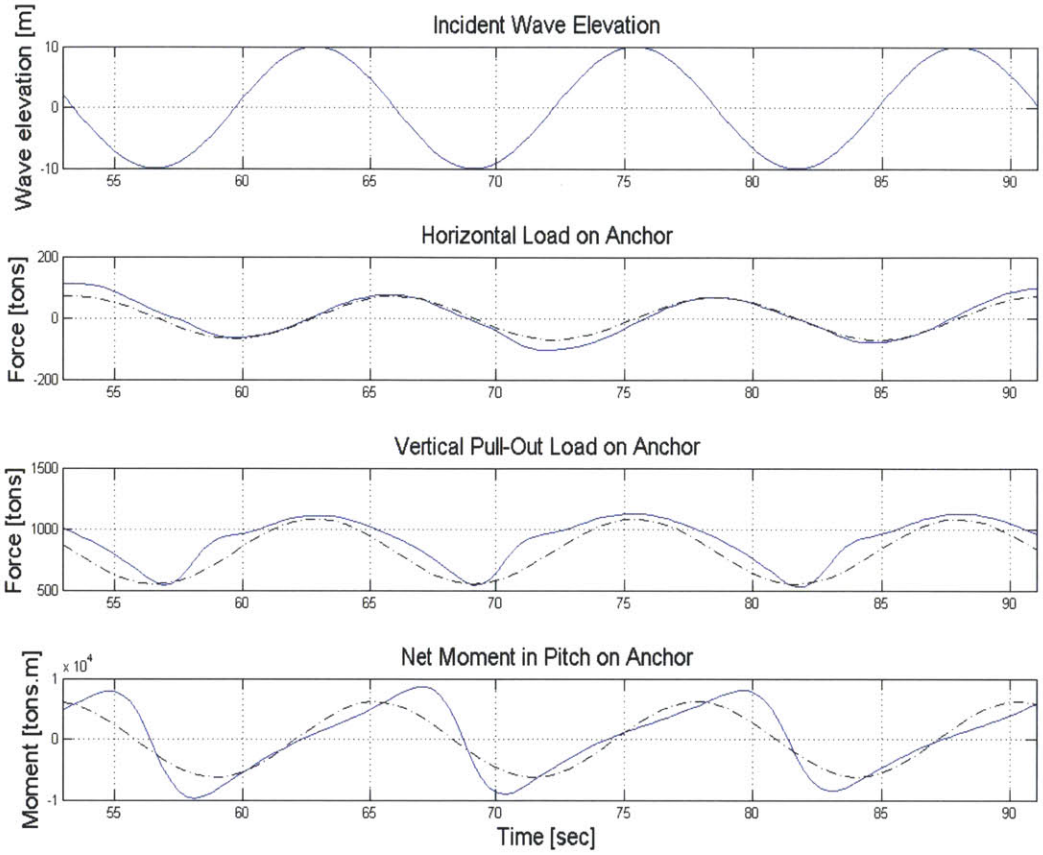


**(Solid line: Nonlinear analysis; Dashed line: Linear analysis)**

Figure 3-45: Incident wave elevation ($\zeta_I$) from the mean waterline; Horizontal load on anchor; Vertical pull-out load on anchor; Net moment in pitch on anchor for incident wave of A=10m and w=0.5 rad/sec.

## 3.10 Power Spectral Density Analysis of Nonlinear Wave Loads in Irregular Seas

In steep and large-amplitude waves, nonlinear wave loads have a significant high-frequency impact on floating structures. This creates ringing loads (Sclavounos [38] and Faltinsen, Newman & Vinje [11]), which may excite the floating wind turbine structure over a range of high frequencies. Since the natural frequency of the wind turbine tower falls around 1.5 rad/sec, this ringing load may have a substantial effect on the fatigue life of the tower and tethers, and thus lead to a system failure.

Most of the structural fatigue analysis and design are based on the frequency domain. The correct representation of the cyclic loading in the frequency domain is an essential component that affects the entire fatigue modeling and analysis.

Power spectral density (PSD) analysis is a useful tool that characterizes the distribution in the frequency domain of the power of $x[n]$, a sequence of random variables defined for every integer $n$ where $n$ is the time index in this work.

Regarding the fundamental principles of PSD, PSD is defined as a Fourier transform of the auto-correlation function $c_{xx}(m)$ of the signal. For a finite length

real-value signal x[n], n=0, 1, ..., L-1, an estimator for the autocorrelation sequence is

$$c_{xx}(m) = \frac{1}{L} \sum_{n=0}^{L-|m|-1} x[n]x[n+|m|] \tag{3.14}$$

where $|m|$ <L.

As an estimate of PSD, the periodogram method is employed and it takes the Fourier transform of the biased autocorrelation estimate, $c_{xx}(m)$ as follows.

$$I_L(w) = \sum_{m=-(L-1)}^{L-1} c_{xx}(m)e^{-jwm} \tag{3.15}$$

The Fourier transform can be obtained by using the fast Fourier transform (FFT), an algorithm that enables a faster computation of discrete Fourier transform (DFT) for the sequences of length n= $2^k$, where k is an integer. In this work, MATLAB provides PSD estimation functions ([34]) based on the FFT scheme, which includes PSD estimation schemes with a windowing-method and a samples-averaging method.

A power spectral density of the wave elevation $S_\zeta$ is defined by the ITTC (Bretschneider) sea spectrum, given a sea state ($H_s$, $T_m$):

$$S_\zeta(w) = H_s^{\,2} \cdot T_m \cdot \frac{0.11}{2\pi} \cdot \left(\frac{wT_m}{2\pi}\right)^{-5} \cdot \exp\left(-0.44 \cdot \left(\frac{wT_m}{2\pi}\right)^{-4}\right) \tag{3.16}$$

where $H_s$ is the significant wave height defined as the mean of the 1/3 highest waves; $T_m$ is the mean wave period in the wave record represented by the above spectral density.

The corresponding time signals of the wave elevation and the ambient wave velocity potential in deep water are obtained as follows.

$$\begin{aligned} \varsigma(x,t) &= \mathrm{Re}\left\{\sum_{n=1}^{N} A_n \exp(-ik_n x + iw_n t + i\varphi_n)\right\} \\ \phi_I(x,z,t) &= \mathrm{Re}\left\{\sum_{n=1}^{N} \frac{igA_n}{w_n} \exp(k_n z - ik_n x + iw_n t + i\varphi_n)\right\} \end{aligned} \tag{3.17}$$

where the $A_n = \sqrt{2 \cdot S_\varsigma(w_n) \cdot \Delta w_n}$ ; $\varphi_n$ is independent random phase, uniformly distributed $[-\pi, \pi]$; $\Delta w_n$ is set to be constant, $\Delta w$, at each frequency band $w_n$.

A nonlinear diffraction problem is simulated for these irregular waves defined by the wave spectra. The nonlinear wave load $\vec{F}_{Hydro}(t)$ is obtained by the Fluid Impulse Theory, which contains a nonlinear Froude-Krylov force, a nonlinear disturbance force and a nonlinear hydrostatic force as presented in section 2.7.

$$\vec{F}_{Hydro}^{DIF}(t) = -\rho \frac{d}{dt} \oint_{S_B^I(t)} \varphi_I \vec{n} ds - \rho \frac{d}{dt} \int_{S_B^I(t)} \varphi_D \vec{n} ds - \rho g \oint_{S_B^I(t)} Z \vec{n} ds \tag{3.18}$$

where $\varphi_D$ is obtained by the time-domain 3D potential-flow simulation based on a transient free-surface Green-function method; $S_B^I(t)$ is the instantaneous body surface under the ambient wave.

The nonlinear equations of motion of the floating wind turbine are re-formulated as follows.

$$
\begin{aligned}
&(M + A_{11}(t))l\left[-sin\theta(t)\cdot\dot{\theta}(t)^2 + \cos\theta(t)\cdot\ddot{\theta}(t)\right] + B_{v11}(l\cos\theta(t)\dot{\theta}(t))\left|(l\cos\theta(t)\dot{\theta}(t))\right| \\
&= \vec{F}_{Hydro}^{DIF}(t)\cdot\vec{e}_1 - T_2(t)sin\theta(t) - T_1^*(t)\sin\theta(t)
\end{aligned}
$$

$$
\begin{aligned}
&(M + A_{33})l\left[-\cos\theta(t)\cdot\dot{\theta}(t)^2 - \sin\theta(t)\cdot\ddot{\theta}(t)\right] + B_{v33}(-l\sin\theta(t)\dot{\theta}(t))\left|(-l\sin\theta(t)\dot{\theta}(t))\right| \\
&= \vec{F}_{Hydro}^{DIF}(t)\cdot\vec{e}_3 - T_2(t)\cos\theta(t) - T_1^*(t)\cos\theta(t) - W_3
\end{aligned}
$$

$$
\begin{aligned}
&(MZ_{CG} + A_{11}(t)Z_{CB}(t))l\left[-sin\theta(t)\cdot\dot{\theta}(t)^2 + \cos\theta(t)\cdot\ddot{\theta}(t)\right] + +B_{v11}Z_{CB}(t)(l\cos\theta(t)\dot{\theta}(t))\left|(l\cos\theta(t)\dot{\theta}(t))\right| \\
&= \vec{M}_{O'_{Hydro}}^{DIF}(t)\cdot\vec{e}_2 - T_2(t)f\cos\theta(t) + T_1^*(t)\frac{f}{2}\cos\theta(t)
\end{aligned}
\tag{3.19}
$$

where $A_{11}(t)$ is the time-varying impulsive added-mass in surge; $Z_{CB}(t)$ is the time-varying center of buoyancy where $\vec{r}_{O'B} = (0,0,Z_{CB}(t))$.

In a large-amplitude nonlinear wave event, the impulsive added-mass in surge $A_{11}(t)$ and the center of buoyancy $Z_{CB}(t)$ are varying over time depending on the ambient wave elevation at each time step. With this nonlinear wave load model and equations of motion applied to irregular waves, the nonlinear diffraction force

and the tether tension response are obtained in the time domain and studied in the frequency domain with a spectral analysis.

For a validation study, the linear-analysis method is employed to evaluate power spectral densities of the linear wave load and the tether tension. The linear wave exciting force is obtained from a linear wave theory and the tether tension is obtained by using the transfer function from linear equations of motion of the floating wind turbine as presented in Chapter 2.

Time signals of the linear wave exciting force $X_j(t)$ and the tether tension $T_j(t)$ are obtained as follows.

$$
\begin{aligned}
X_1(t) &= \mathrm{Re}\left\{\sum_{n=1}^{N} A_n \cdot \mathrm{X}_1(w_n) \cdot \exp(iw_n t + i\varphi_n)\right\} \\
X_5(t) &= \mathrm{Re}\left\{\sum_{n=1}^{N} A_n \cdot \mathrm{X}_5(w_n) \cdot \exp(iw_n t + i\varphi_n)\right\} \\
T_1(t) &= \mathrm{Re}\left\{\sum_{n=1}^{N} A_n \cdot \mathrm{T}_1(w_n) \cdot \exp(iw_n t + i\varphi_n)\right\} \\
T_2(t) &= \mathrm{Re}\left\{\sum_{n=1}^{N} A_n \cdot \mathrm{T}_2(w_n) \cdot \exp(iw_n t + i\varphi_n)\right\}
\end{aligned}
\tag{3.20}
$$

where $\mathrm{X}_j(w_n)$ is the wave exciting force computed by WAMIT for the frequency $w_n$; $\mathrm{T}_j(w_n)$ is the transfer function of the tether tension for the frequency $w_n$ ;where the $A_n = \sqrt{2 \cdot S_\varsigma(w_n) \cdot \Delta w_n}$ ; $\varphi_n$ is independent random phase, uniformly distributed $[-\pi, \pi]$; $\Delta w_n$ is set to be constant, $\Delta w$, at each frequency band $w_n$.

Power spectral densities of the linear wave exciting force and the tether tension are obtained as follows.

$$S_{X_j}(w_n) = \left|\mathrm{X}_j(w_n)\right|^2 \cdot S_\zeta(w_n)$$
$$S_{T_j}(w_n) = \left|\mathrm{T}_j(w_n)\right|^2 \cdot S_\zeta(w_n) \qquad (3.21)$$

The simulation is carried out for irregular waves of significant wave height $H_s$ of 6.0 m and mean wave period $T_m$ of 11.6 sec.

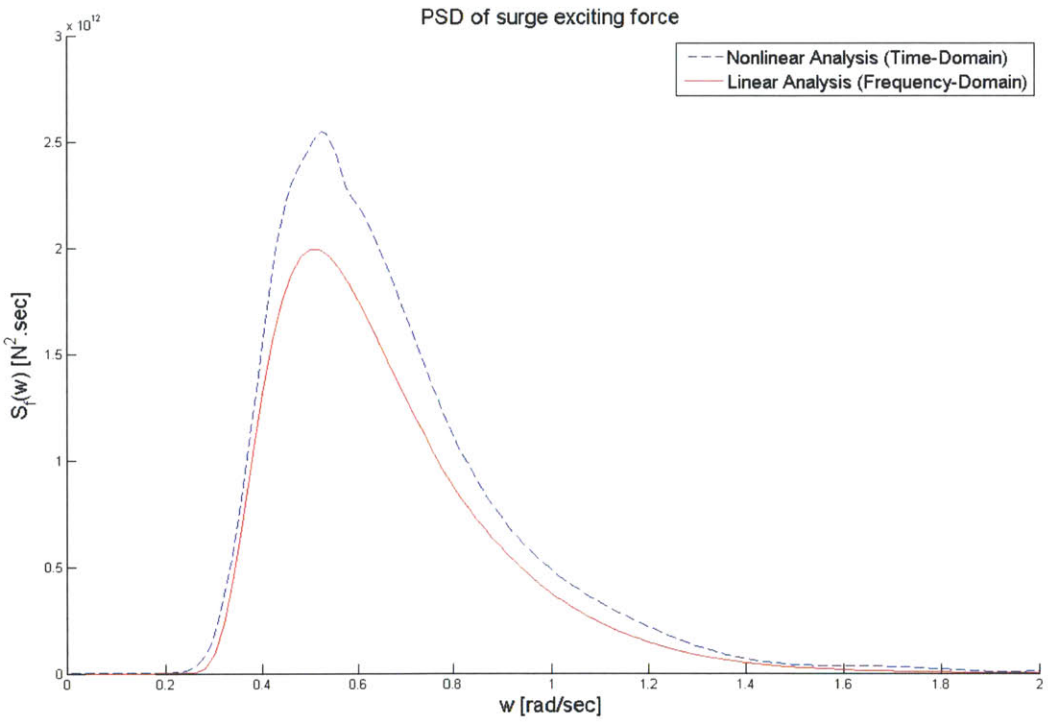


**( ——: Linear analysis; – – –: Nonlinear analysis)**

Figure 3-46: The power spectral density of wave exciting force in surge ( $F_{Hydro_1}$ ) for irregular waves of $H_s$ = 6.0 m and $T_m$ = 11.6 sec.

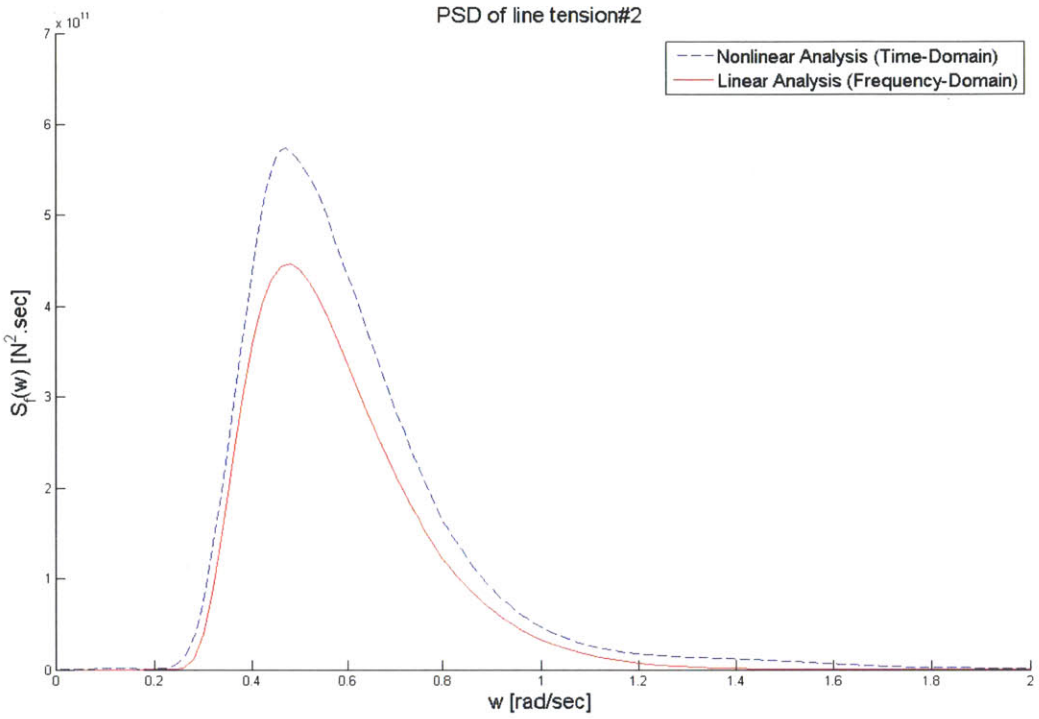


**( ——: Linear analysis; – – –: Nonlinear analysis)**

Figure 3-47: The power spectral density of tether tension#2 $T_2(t)$ for irregular waves of $H_s$ = 6.0 m and $T_m$ = 11.6 sec.

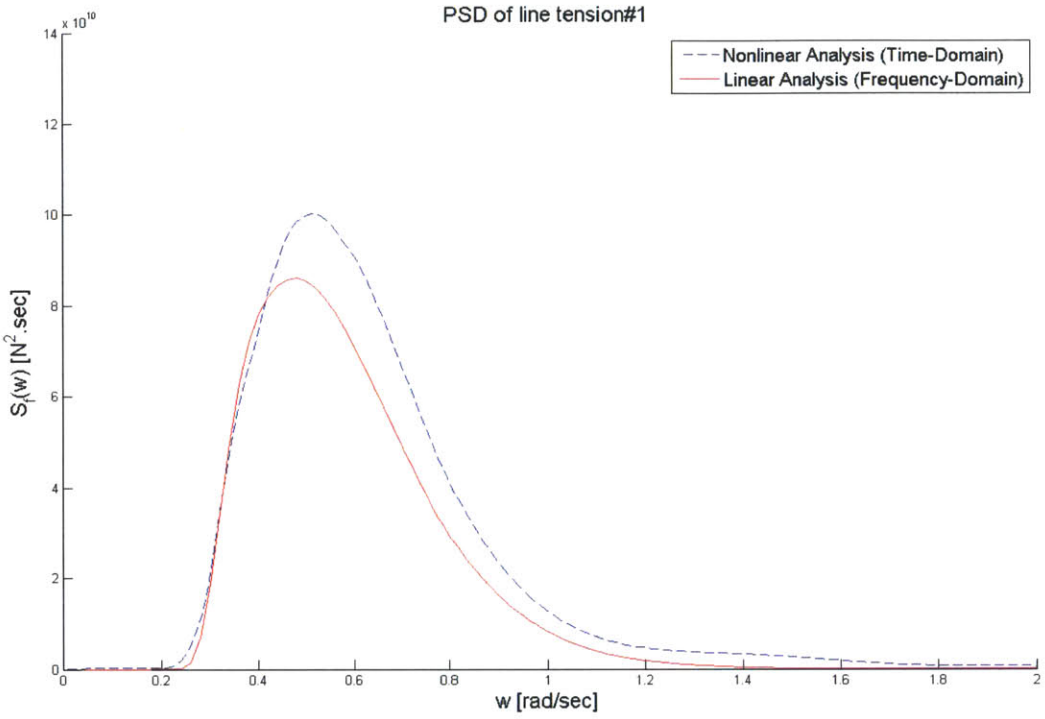


**( ——: Linear analysis; – – –: Nonlinear analysis)**

Figure 3-48: The power spectral density of tether tension#1 $T_1(t)$ for irregular waves of $H_s$ = 6.0 m and $T_m$ = 11.6 sec.

For the analysis of the ringing wave load, an additional set of figures over a high-frequency band is attached as follows.

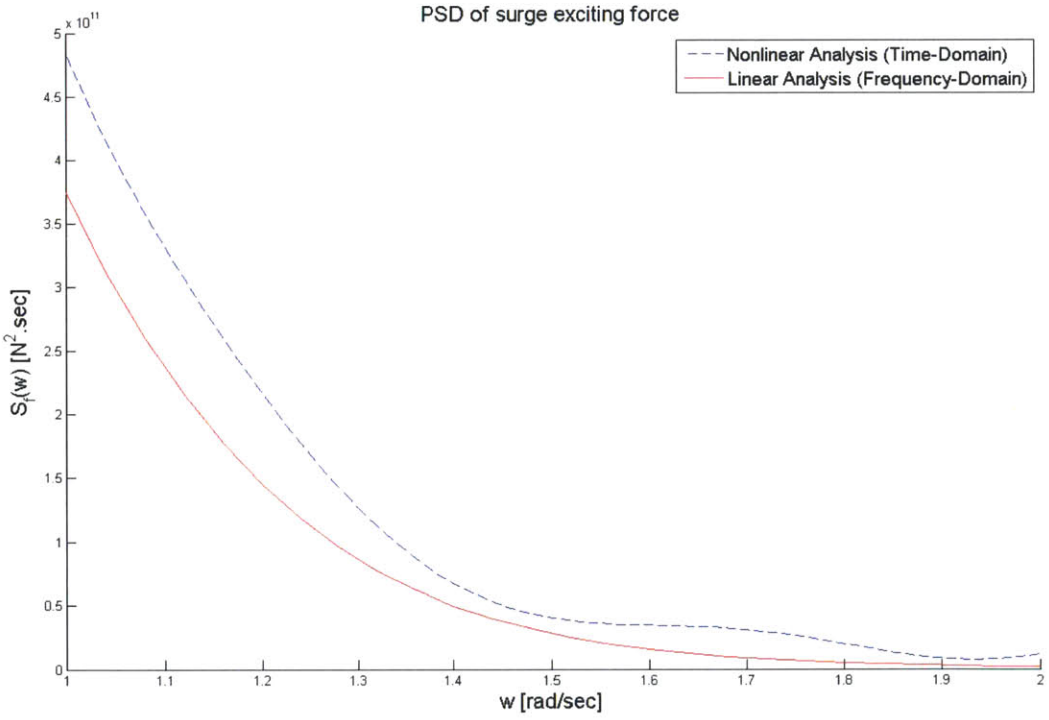


**( ——: Linear analysis; – – –: Nonlinear analysis)**

Figure 3-49: The power spectral density of wave exciting force in surge ( $F_{Hydro_1}$ ) for irregular waves of $H_s$ = 6.0 m and $T_m$ = 11.6 sec.

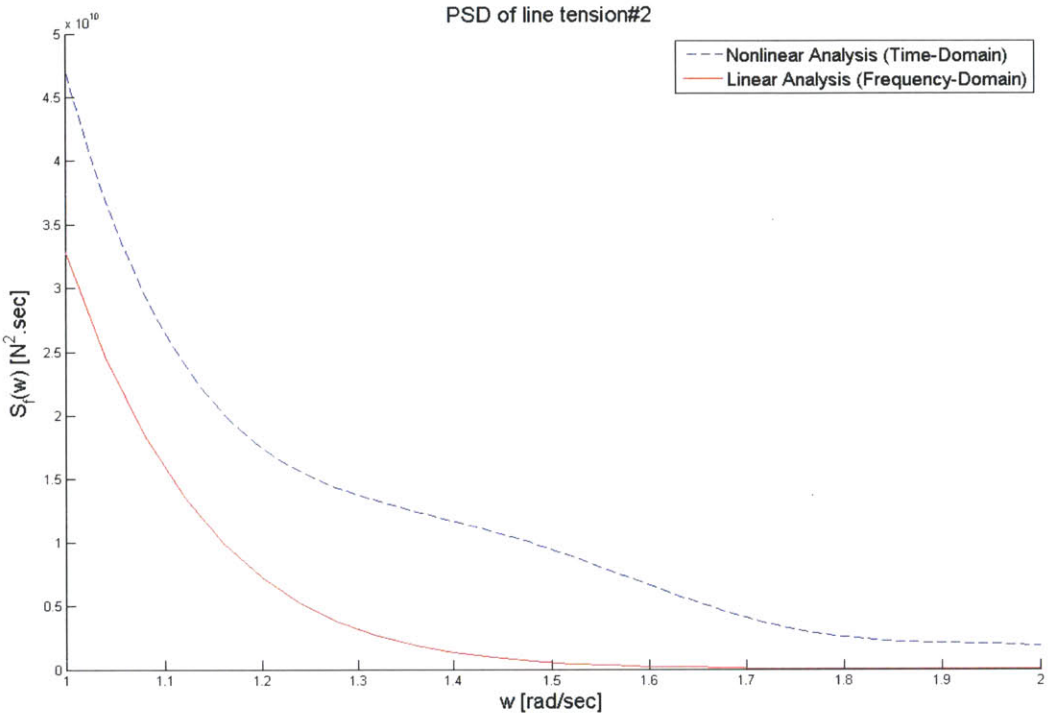


**( ——: Linear analysis; – – –: Nonlinear analysis)**

Figure 3-50: The power spectral density of tether tension#2 $T_2(t)$ for irregular waves of $H_s$ = 6.0 m and $T_m$ = 11.6 sec.

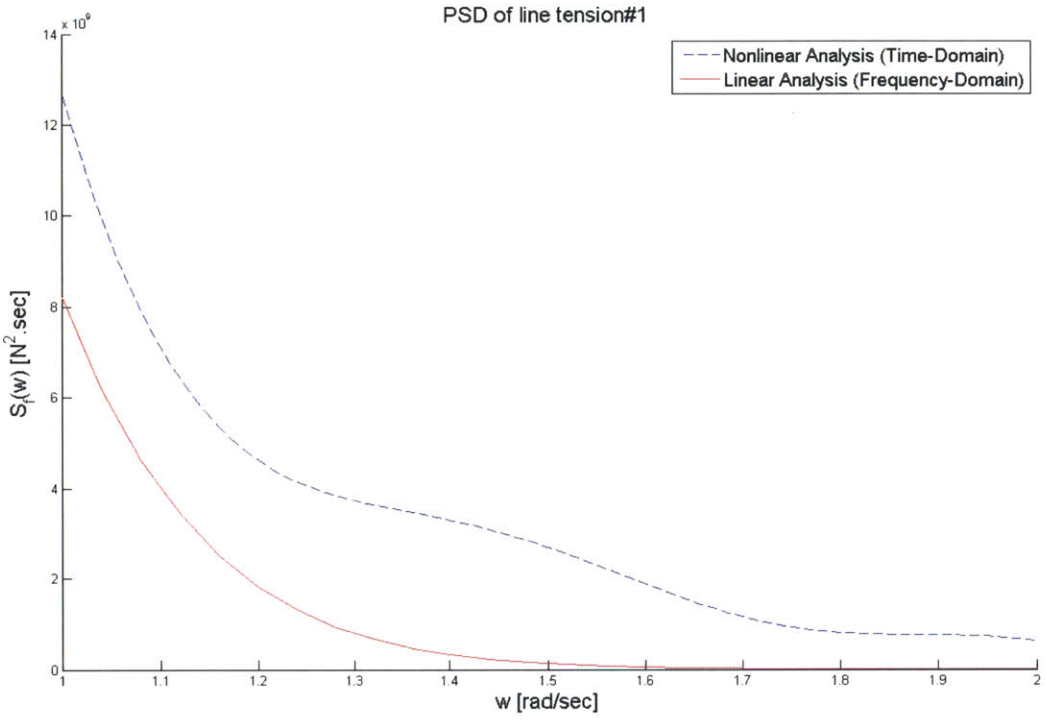


**( ——: Linear analysis; - - -: Nonlinear analysis)**

Figure 3-51: The power spectral density of tether tension#1 $T_1(t)$ for irregular waves of $H_s$ = 6.0 m and $T_m$ = 11.6 sec.

The simulation is carried out for irregular waves of significant wave height $H_s$ of 10.0 m and mean wave period $T_m$ of 13.6 sec.

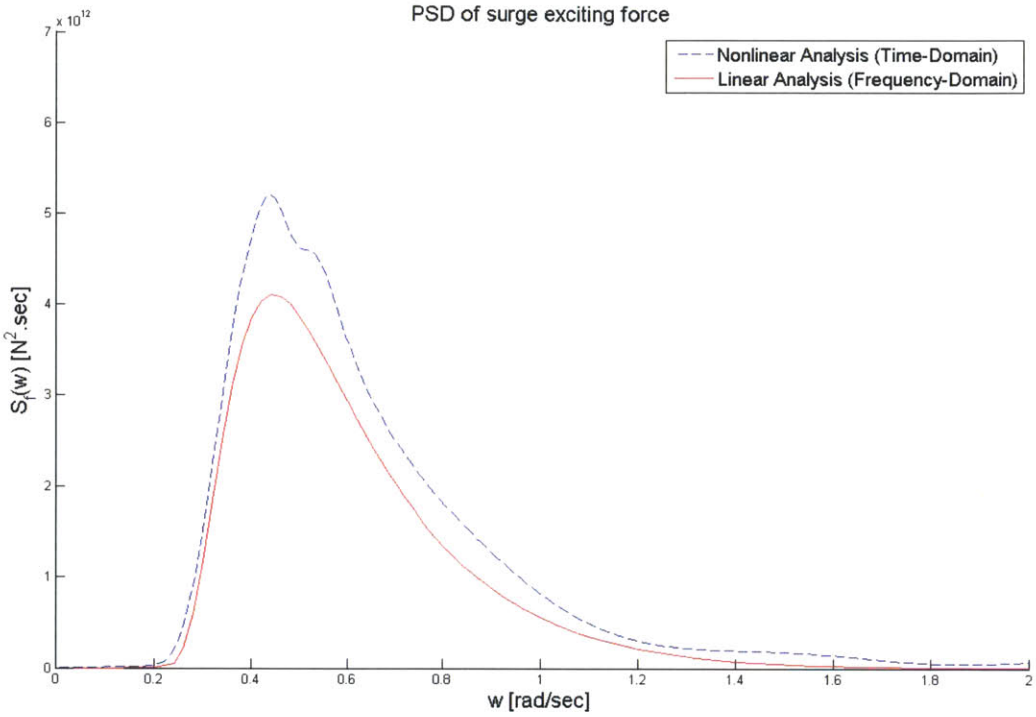


**( ——: Linear analysis; – – –: Nonlinear analysis)**

Figure 3-52: The power spectral density of wave exciting force in surge ( $F_{Hydro_1}$ ) for irregular waves of $H_s$ = 10.0 m and $T_m$ = 13.6 sec.

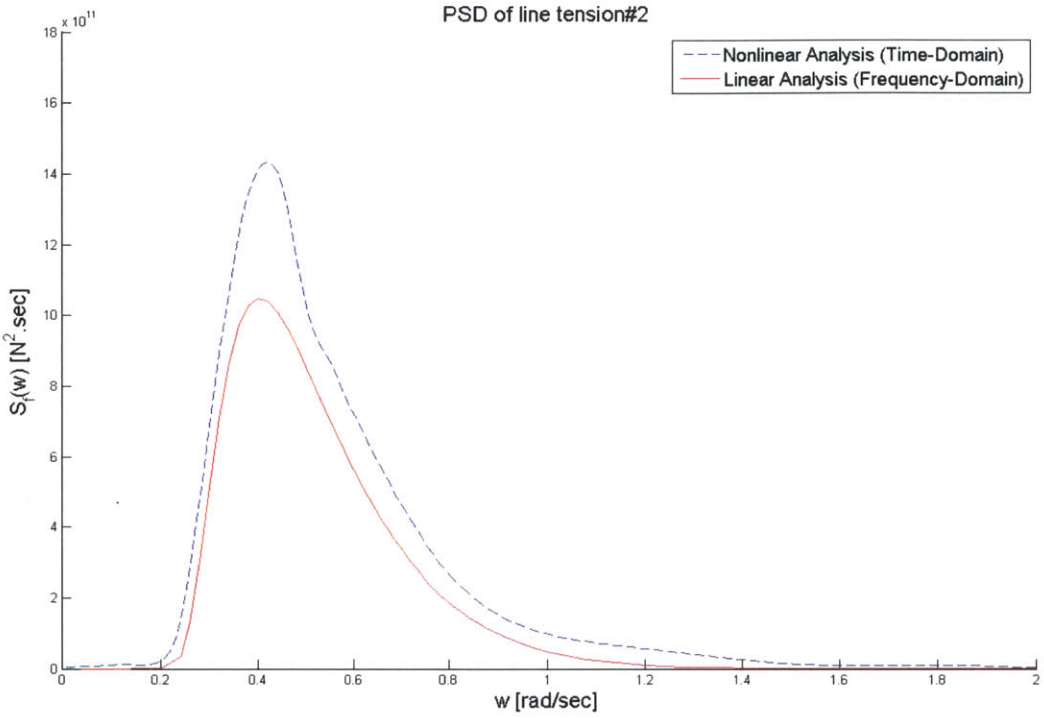


**( ——: Linear analysis; – – –: Nonlinear analysis)**

Figure 3-53: The power spectral density of tether tension#2 $T_2(t)$ for irregular waves of $H_s$ = 10.0 m and $T_m$ = 13.6 sec.

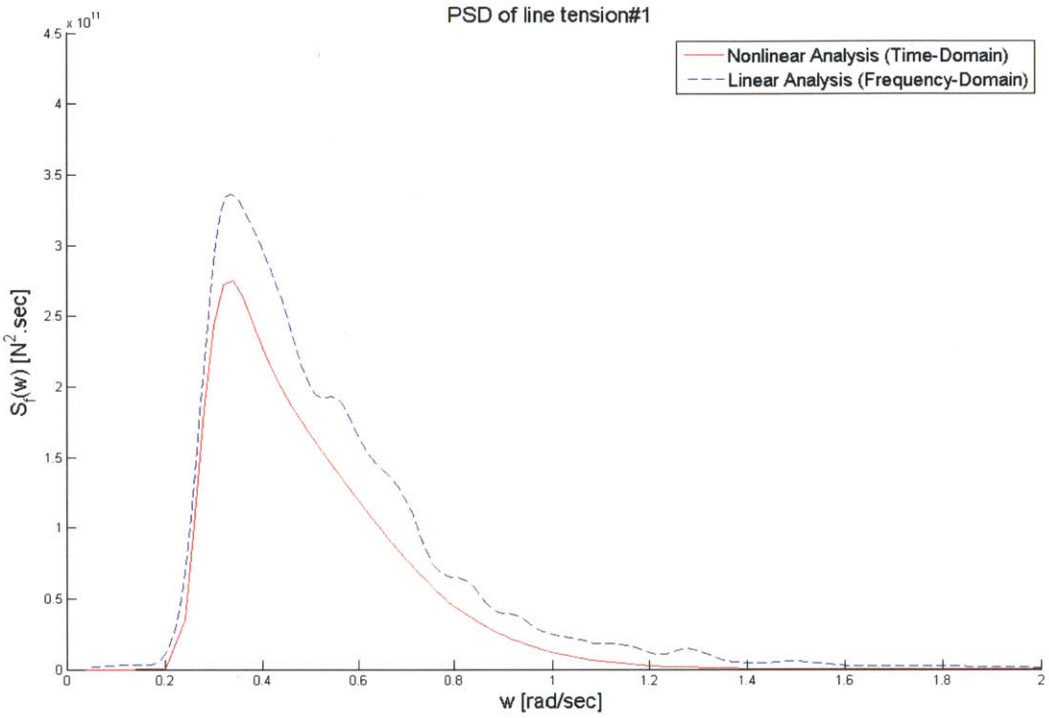


**( ——: Linear analysis; – – –: Nonlinear analysis)**

Figure 3-54: The power spectral density of tether tension#1 $T_1(t)$ for irregular waves of $H_s$ = 10.0 m and $T_m$ = 13.6 sec.

For the analysis of the ringing wave load, an additional set of figures over a high-frequency band is attached as follows.

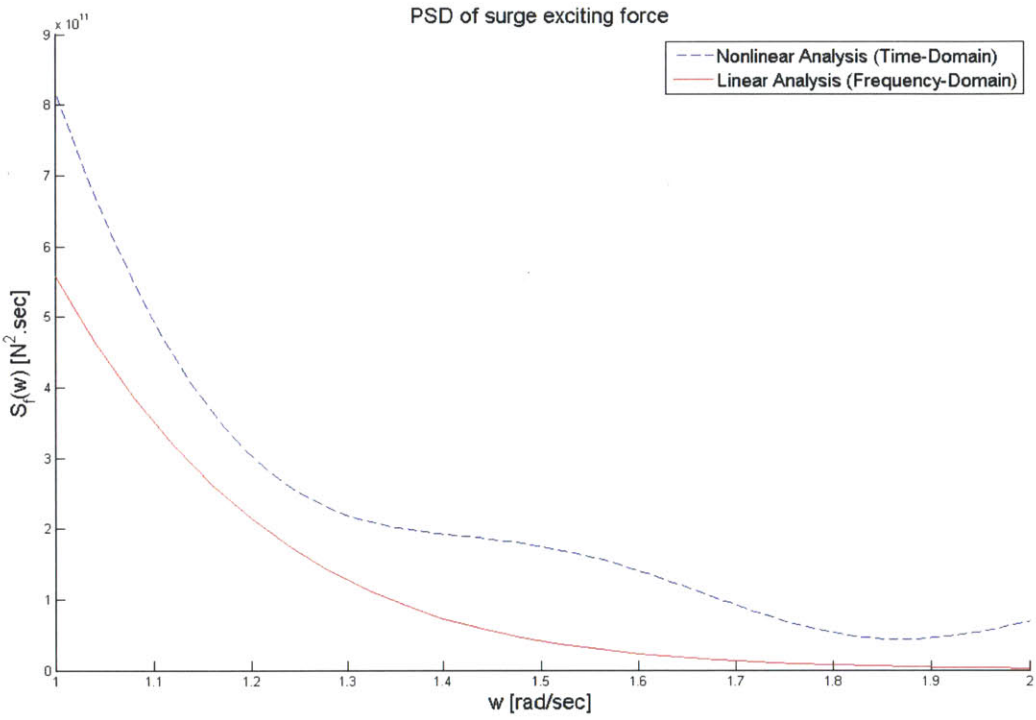


**( ——: Linear analysis; – – –: Nonlinear analysis)**

Figure 3-55: The power spectral density of wave exciting force in surge ( $F_{Hydro_1}$ ) for irregular waves of $H_s$ = 10.0 m and $T_m$ = 13.6 sec.

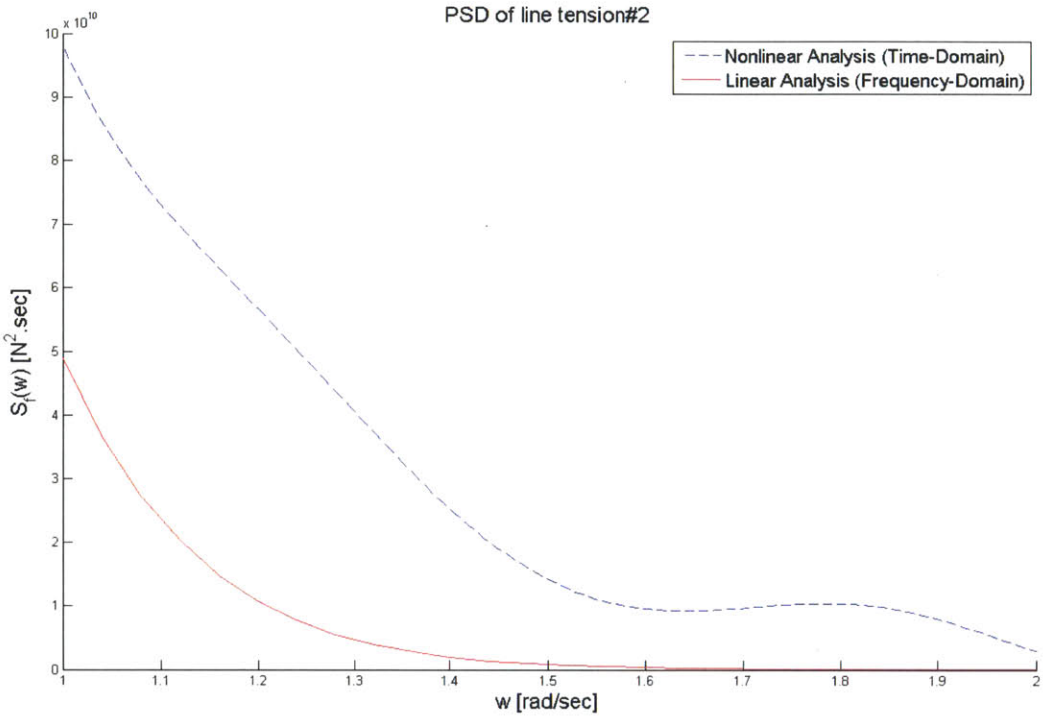


**( ——: Linear analysis; – – –: Nonlinear analysis)**

Figure 3-56: The power spectral density of tether tension#2 $T_2(t)$ for irregular waves of $H_s$ = 10.0 m and $T_m$ = 13.6 sec.

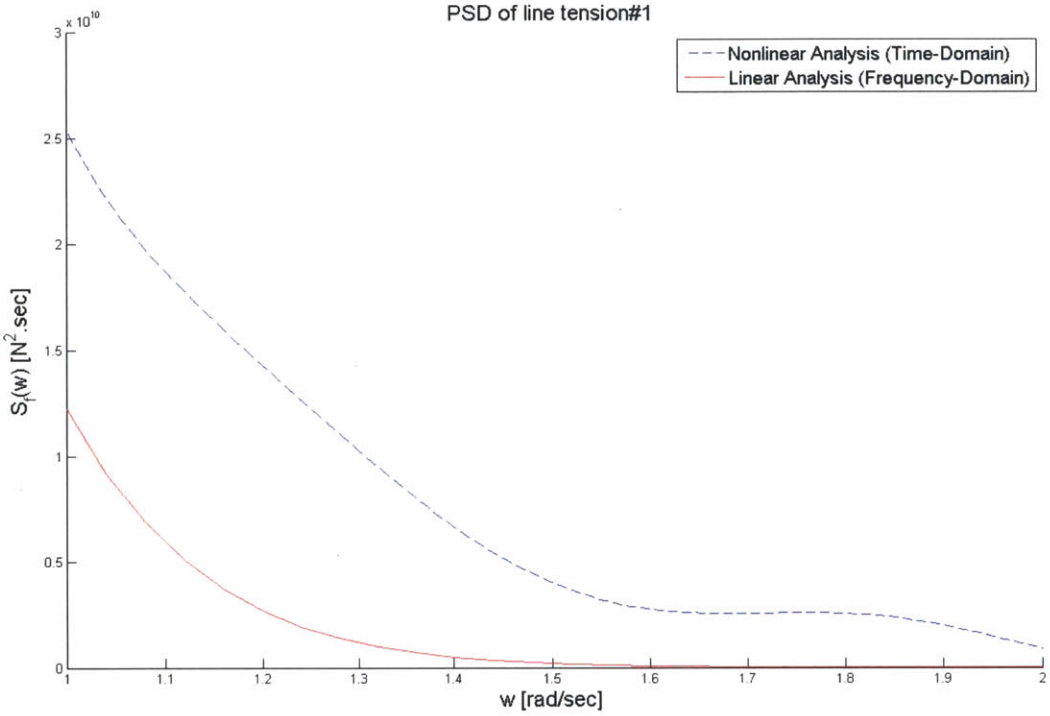


**( ——: Linear analysis; – – –: Nonlinear analysis)**

Figure 3-57: The power spectral density of tether tension#1 $T_1(t)$ for irregular waves of $H_s$ = 10.0 m and $T_m$ = 13.6 sec.

# Chapter 4

# Discussion

A three-dimensional time-domain potential-flow solver has been developed for simulations of nonlinear wave-body interactions based on a transient free-surface Green-function method and the Weak Scatterer Hypothesis. This thesis presents the nonlinear wave load model based on the Fluid Impulse Theory (FIT) under a weak-scatterer free-surface condition. The nonlinear wave load has been addressed and employed in the time domain simulation of the floating wind turbine as two applications of the present research: an analysis of the extreme wave-load response of the floating wind turbine for steep large-amplitude waves, and an analysis of the ringing wave-load response for irregular seas using a power spectral density analysis method.

Based on the FIT, the fluid force on a floating body is driven by two distinct components: the body-surface impulse and the free-surface impulse. The order of magnitude analysis reveals that the contribution from the free-surface impulse is negligible compared to the body-surface impulse. The nonlinear wave-body interaction simulation, which is based on a transient free-surface Green-function method, is carried out to demonstrate the relative significance of the free-surface

impulse from the body-surface impulse for various wave conditions in terms of wave steepness $kA$'s and the body dimensions $kd$'s. We find the following results: the mean fractional error $\bar{e}$ is in the range of 0.03 and 0.06 for the wave steepness $kA$ of around 0.1; the mean error $\bar{e}$ is in the range of 0.06 and 0.12 for the wave steepness $kA$ of around 0.2; and the mean error $\bar{e}$ is in the range of 0.1 and 0.2 for the wave steepness $kA$ of around 0.3. The wave steepness of the most extreme wave may be up to ~0.4. This study reveals that the body-surface impulse dominates the wave loads on floating bodies in a leading order and justifies the simpler form of the FIT, which leads us to an efficient and robust nonlinear wave load model.

With this new nonlinear wave-load model based on the FIT, nonlinear response simulations of the floating wind turbine were performed for several extreme waves. The large-amplitude waves and large-amplitude body motions are the primary source of the nonlinearity on the wave loads and the resultant tether-tensions. The present nonlinear wave load model takes the instantaneous wetted surface of the body into the wave load formulation, which essentially accounts for the time-varying added mass. In other words, this model accounts for the time-varying inertial property of a floating body in extreme waves. In addition, large body motions create a significant nonlinearity on the wave load. The nonlinearity in wave loads is transmitted to the tether tensions and therefore to the anchor loads as well. The comparison with the linear analysis, based on linear wave theory and linear dynamics theory, shows that the linear analysis underestimates the peak values of the tether tension and thus the anchor's pull-out load in particular. However, the performance of the linear analysis was relatively good at predicting

the motion responses and also the leading order values of the tether tensions and the anchor loads.

In the sample simulation for a unidirectional ambient wave of 6 m in amplitude, 0.5 rad/sec in frequency and 0.15 in wave steepness $kA$, the linear analysis method underestimates the amplitude of the tether's tension #1 and tension #2 by 20 metric tons and 40 metric tons, respectively. The linear analysis method underestimates the net pitch moment on the anchor by 1200 metric tons·m. The vertical pull-out load on the anchor is dominated by the wave load in heave, and the difference between the results from the linear analysis and nonlinear analysis is relatively small.

In the sample simulation for a unidirectional ambient wave of 10 m in amplitude, 0.5 rad/sec in frequency and 0.25 in wave steepness $kA$, the results from the nonlinear analysis deviate more severely from the results from the linear analysis, which appear in the form of harmonic oscillations. The linear analysis method underestimates the amplitude of the tether's tension #1 and tension #2 by 70 metric-tons and 130 metric-tons, respectively. The linear analysis method underestimates the net pitch moment on the anchor by 2500 metric tons·m. In the vertical pull-out load on the anchor, the results from the nonlinear analysis severely deviate as well from the results from the linear analysis, but the difference between the results from the linear analysis and nonlinear analysis is relatively small in terms of the peak value of the load.

Separately, nonlinear wave loads in irregular seas were simulated in the time-domain and analyzed in the frequency-domain by a power-spectral-density analysis method. The tether-tension's response due to the nonlinear wave loads on the floating wind turbine was obtained as well and represented in terms of a power-spectral-density. By comparison with the linear wave theory, the spectral energy distribution of the nonlinear wave loads was successfully identified.

Sample simulations were run for the following irregular sea states: 6 m in significant wave height $H_s$ and 12 sec in mean wave period $T_m$; and 10 m in significant wave height $H_s$ and 13 sec in mean wave period $T_m$. The use of the present nonlinear wave-load model successfully estimates the power spectral densities of nonlinear wave loads and tether tensions. We find through the power spectral density analysis that nonlinear wave loads are distributed over a broad range of frequencies and so are the nonlinear loads on tether tensions. The nonlinear wave loads spectrum exceeds the linear analysis results by around 20 % at low frequencies, which are in the regime of extreme wave-loads, and by 200-300 % or even higher at high frequencies, which are in the regime of ringing wave-loads. By using the present wave load model, we can estimate the nonlinear ringing wave-loads, which are not correctly captured by the linear analysis and yet are critical to the fatigue analysis of the wind-turbine tower and blades, and the tether tensions of the offshore floating wind turbine.

Suggestions for future research topics are as follows. In the usage of the free-surface stretching method, the numerical body-surface was generated at each

time step by varying the draft of the buoy in a numerical stretched domain. For extremely steep waves or for non-slender floating bodies, however, the exact mapping of the underwater body-surface into a numerical domain may be required, and investigating this effect would be needed. The validation of nonlinear responses of the floating wind turbine through model testing or full-scaled experiments would be useful. In such a validation study the viscous forces on the floater need to be added as Morrison like terms functions of the relative wave and body kinematics. As another application of the present wave-load model based on the Fluid Impulse Theory, sea-keeping problems of ships in extreme wave conditions can be studied further to confirm the applicability of the Fluid Impulse Theory in a wide range of problems in ocean engineering.

# Appendix A: Specification of MIT TLP-Based Floating Wind Turbine

| | | |
|---|---|---|
| Sea Condition | Water depth [m] | 100.0 |
| | Sea state, Hs [m] | 6/10 |
| | | |
| | | |
| Wind Turbine | Model | 3MW turbine (Nominal model) |
| | Hub height from the tower bottom [m] | 50.0 |
| | Center of gravity in z-axis from the tower bottom [m] | 31.8 |
| | Mass [tons] | 393.3 |
| | | |
| Transition Piece | Radius [m] | 2.1 |
| | Total Vertical Length [m] | 25.0 |
| | Arm Length [m] | 15.0 |
| | Mass [tons] | 271.0 |
| | | |
| | | |
| Floating Buoy | Radius [m] | 4.2 |
| | Draft [m] | 30.0 |
| | Displacement [tons] | 1725.0 |
| | Steel thickness [m] | 0.035 |
| | Number of ring stiffeners | 6 |
| | Mass [tons] | 268.0 |
| | | |
| | | |
| Mooring Lines | Mooring type | TLP |
| | Number of mooring sides | 3 |
| | Number of mooring layers | 1 |
| | Ap [deg] | 90.0 |
| | Pretension per line [tons] | 262.0 |
| | EA per line [N] | 600E06 |
| | L [m] | 17.0 |
| | Rf [m] | 15.0 |
| | Mass [tons] | 4.4 |

# Appendix B: Averaged Samples for the Power Spectral Density

## B.1 Sea state 1 (Hs = 1m)

For a validation study, the simulation is carried out for a cylindrical buoy (2 m in radius; 10 m in draft) for irregular waves of significant wave height $H_s$ of 1.0 m and mean wave period $T_m$ of 13.6 sec.

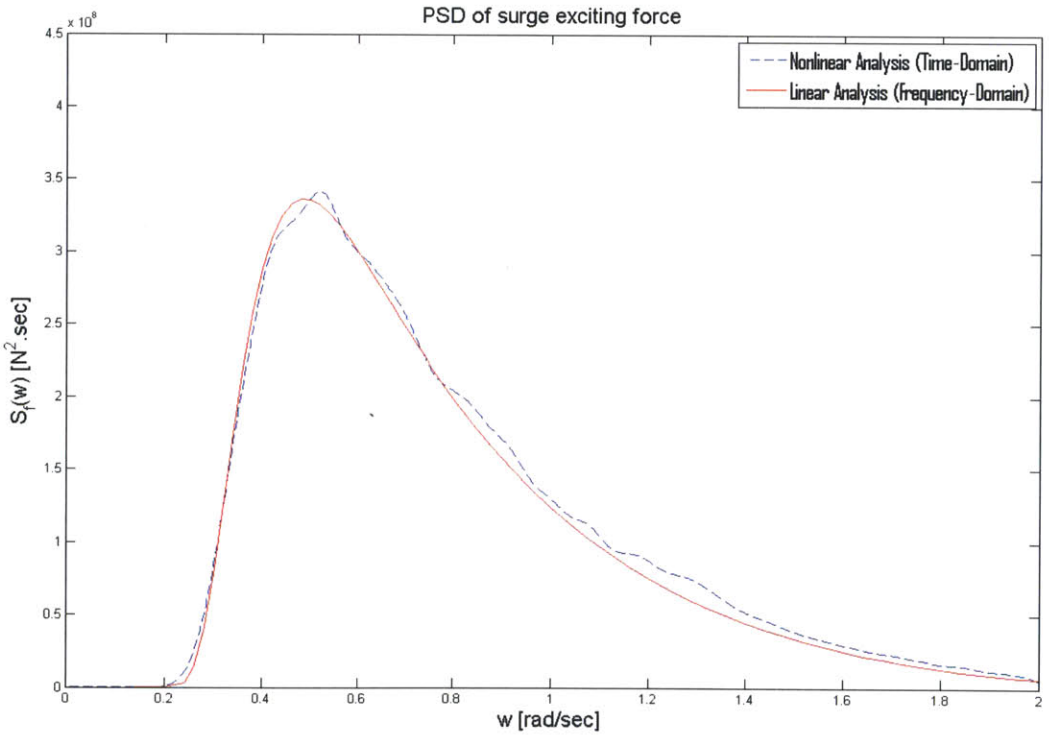


**(– – ·) Nonlinear analysis (time-domain) (——) Linear analysis (frequency-domain)**

Figure B-1: Power spectral density of wave exciting force in surge ( $F_{Hydro_1}$ ) for irregular waves of $H_s$ = 1.0 m and $T_m$ = 13.6 sec.

## B.2 Sea state 2 (Hs = 6m)

The simulation is carried out for irregular waves of significant wave height $H_s$ of 6.0 m and mean wave period $T_m$ of 11.6 sec. Each sample corresponds to a wave elevation signal $\varsigma(x,t)$ and an ambient wave velocity potential $\phi_I(x,z,t)$ created by a different set of random phases $\varphi_n$ uniformly distributed $[-\pi,\pi]$ for $A_n = \sqrt{2 \cdot S_\varsigma(w_n) \cdot \Delta w_n}$ as follows:

$$\varsigma(x,t) = \mathrm{Re}\left\{\sum_{n=1}^{N} A_n \exp(-ik_n x + iw_n t + i\varphi_n)\right\}$$

$$\phi_I(x,z,t) = \mathrm{Re}\left\{\sum_{n=1}^{N} \frac{igA_n}{w_n} \exp(k_n z - ik_n x + iw_n t + i\varphi_n)\right\}$$

where the $A_n = \sqrt{2 \cdot S_\varsigma(w_n) \cdot \Delta w_n}$; $\varphi_n$ is independent random phase, uniformly distributed $[-\pi,\pi]$; $\Delta w_n$ is set to be constant, $\Delta w$, at each frequency band $w_n$.

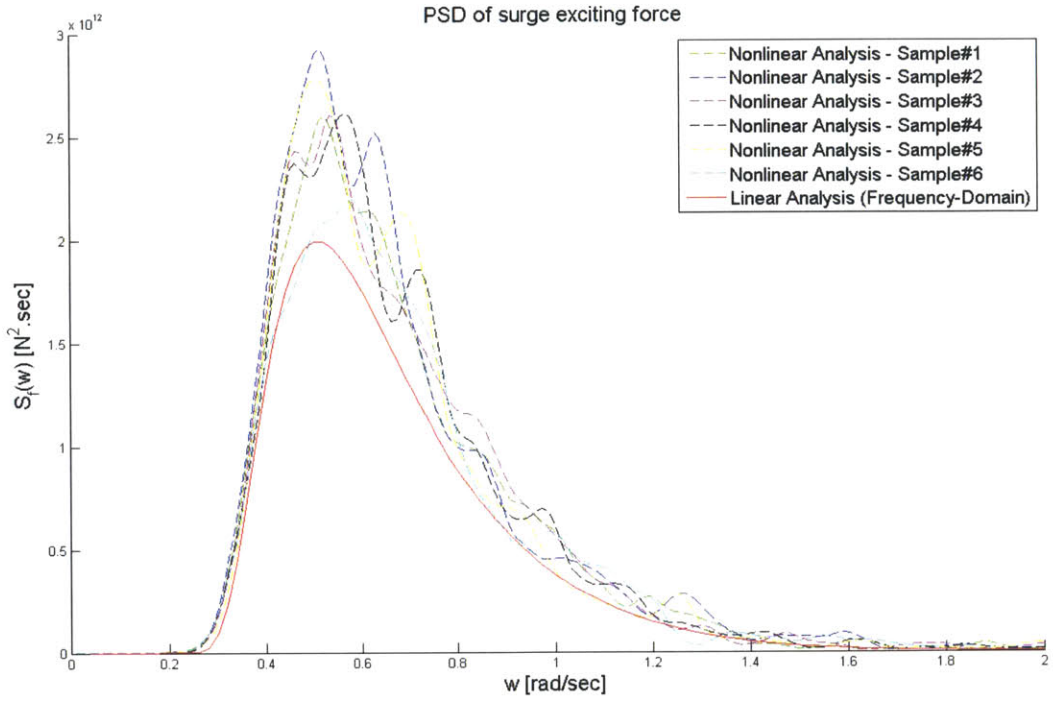


(six samples)

Figure B-2: The power spectral density of wave exciting force in surge ( $F_{Hydro_1}$ ) for irregular waves of $H_s$ = 6.0 m and $T_m$ = 11.6 sec.

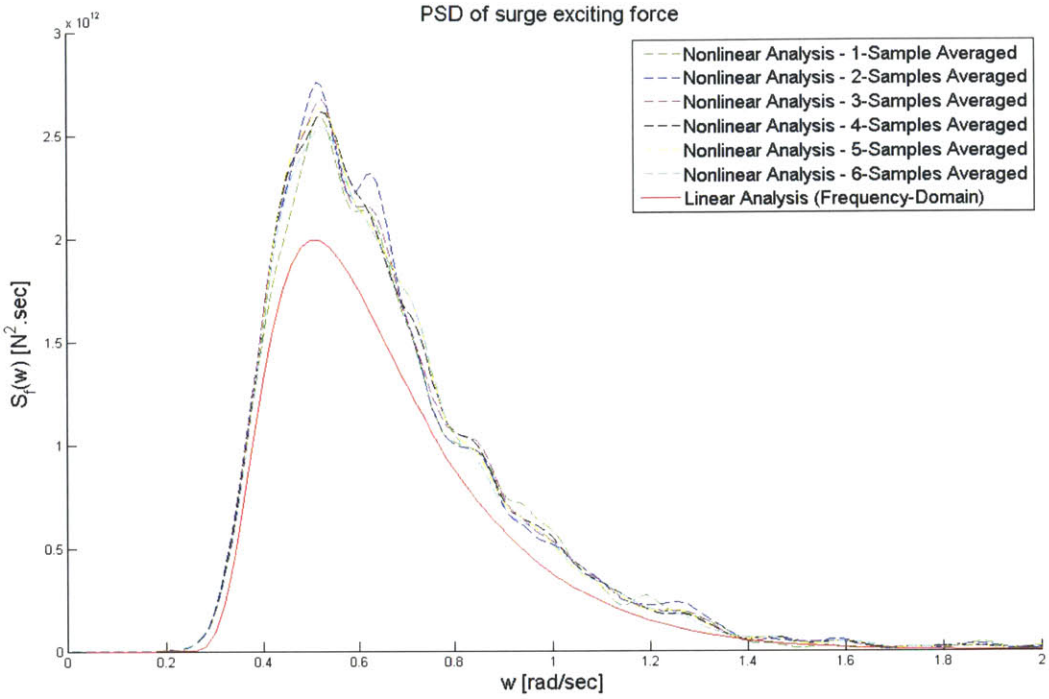


(six averaged-samples)

Figure B-3: The power spectral density of wave exciting force in surge ( $F_{Hydro_1}$ ) for irregular waves of $H_s$ = 6.0 m and $T_m$ = 11.6 sec.

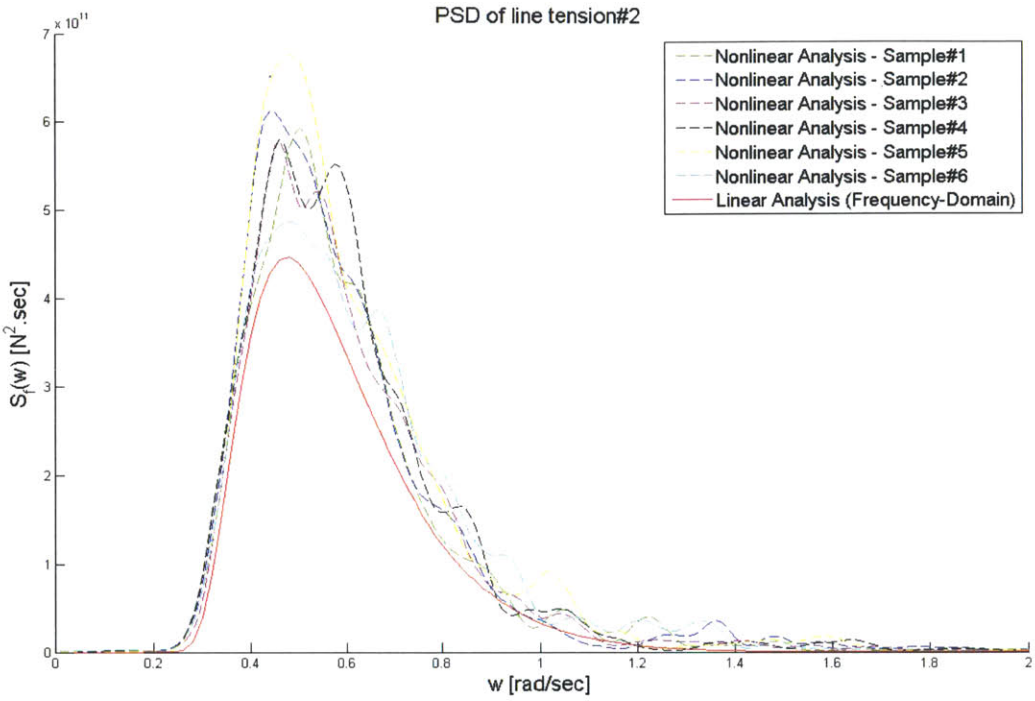


(six samples)

Figure B-4: The power spectral density of tether tension#2 $T_2(\omega)$ for irregular waves of $H_s$ = 6.0 m and $T_m$ = 11.6 sec.

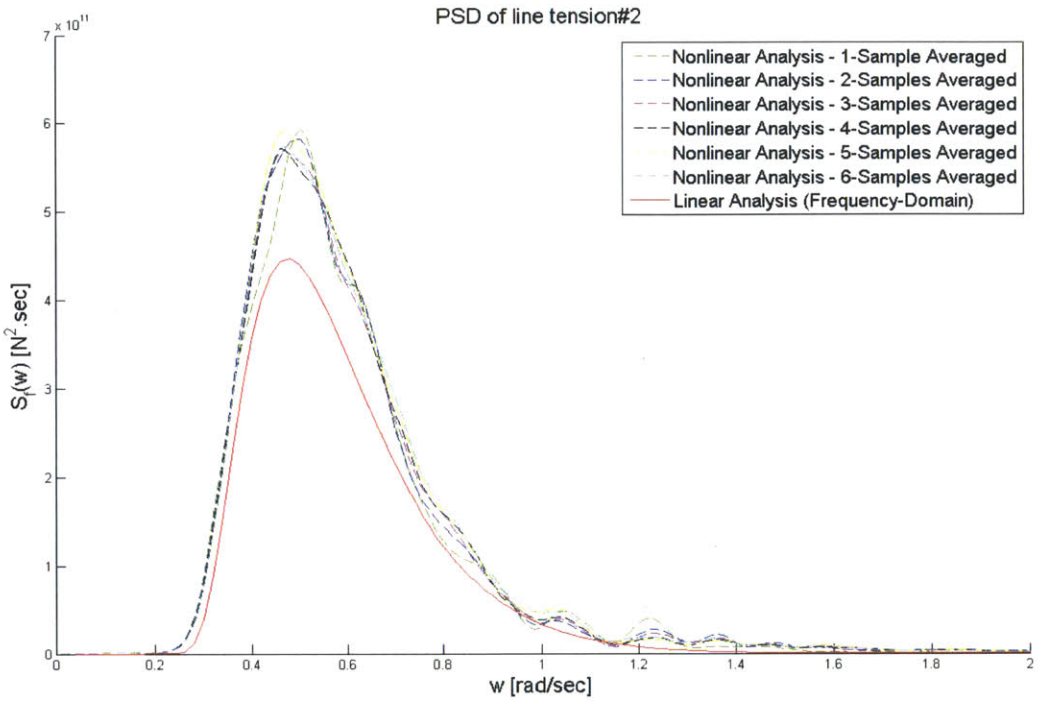


(six averaged-samples)

Figure B-5: The power spectral density of tether tension#2 $T_2(\omega)$ for irregular waves of $H_s$ = 6.0 m and $T_m$ = 11.6 sec.

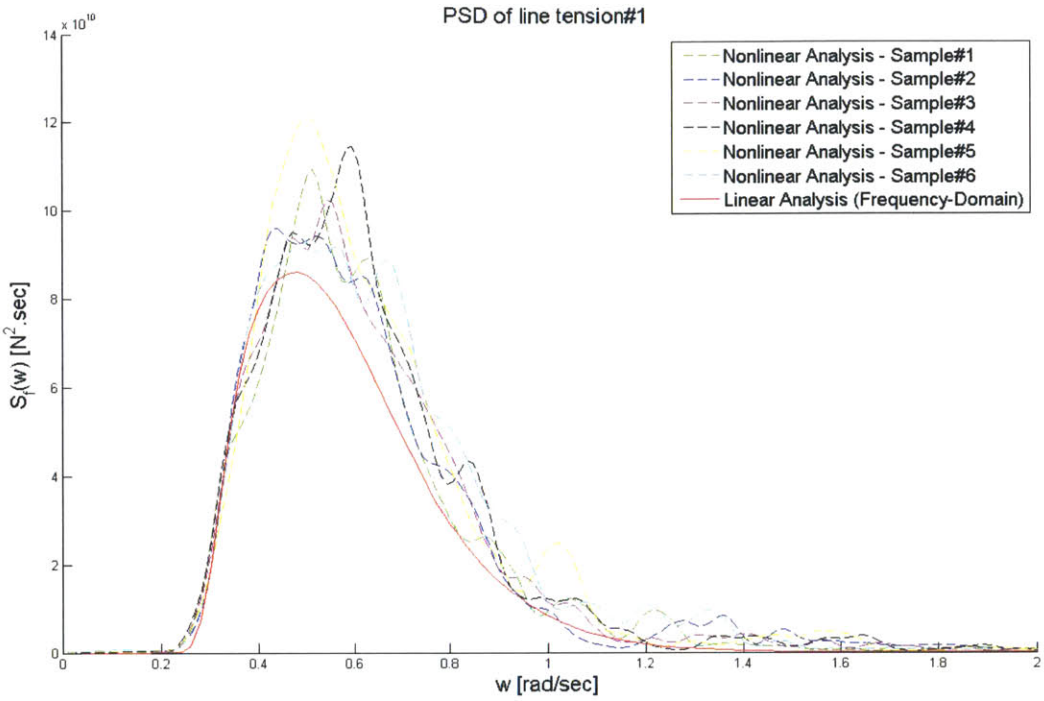


(six samples)

Figure B-6: The power spectral density of tether tension#1 $T_1(\omega)$ for irregular waves of $H_s$ = 6.0 m and $T_m$ = 11.6 sec.

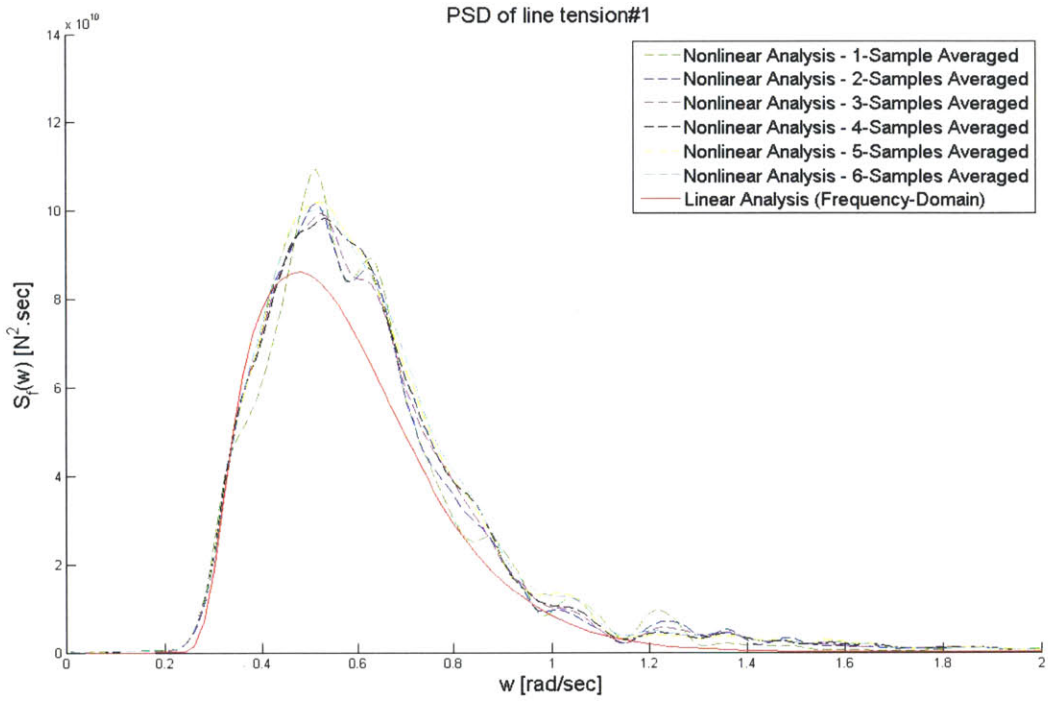


(six averaged-samples)

Figure B-7: The power spectral density of tether tension#1 $T_1(\square)$ for irregular waves of $H_s$ = 6.0 m and $T_m$ = 11.6 sec.

## B.3 Sea state 3 (Hs = 10m)

The simulation is carried out for irregular waves of significant wave height $H_s$ of 10.0 m and mean wave period $T_m$ of 13.6 sec. Each sample corresponds to a wave elevation signal $\varsigma(\square,\square)$ and an ambient wave velocity potential $\phi_\square(\square,\square,\square)$ created by a different set of random phases $\varphi_\square$ uniformly distributed $[-\pi,\pi]$ for $\square_\square=\sqrt{2\cdot\square_\varsigma(\square_\square)\cdot\Delta\square_\square}$ as follows:

$$\varsigma(\square,\square)=\mathrm{Re}\left\{\sum_{\square=1}^{\square}\square_\square\exp(-\square\square_\square\square+\square\square_\square\square+\square\varphi_\square)\right\}$$

$$\phi_\square(\square,\square,\square)=\mathrm{Re}\left\{\sum_{\square=1}^{\square}\frac{\square\square\square_\square}{\square_\square}\exp(\square_\square\square-\square\square_\square\square+\square\square_\square\square+\square\varphi_\square)\right\}$$

where the $\square_\square=\sqrt{2\cdot\square_\varsigma(\square_\square)\cdot\Delta\square_\square}$; $\varphi_\square$ is independent random phase, uniformly distributed $[-\pi,\pi]$; $\Delta\square_\square$ is set to be constant, $\Delta\square$, at each frequency band $\square_\square$.

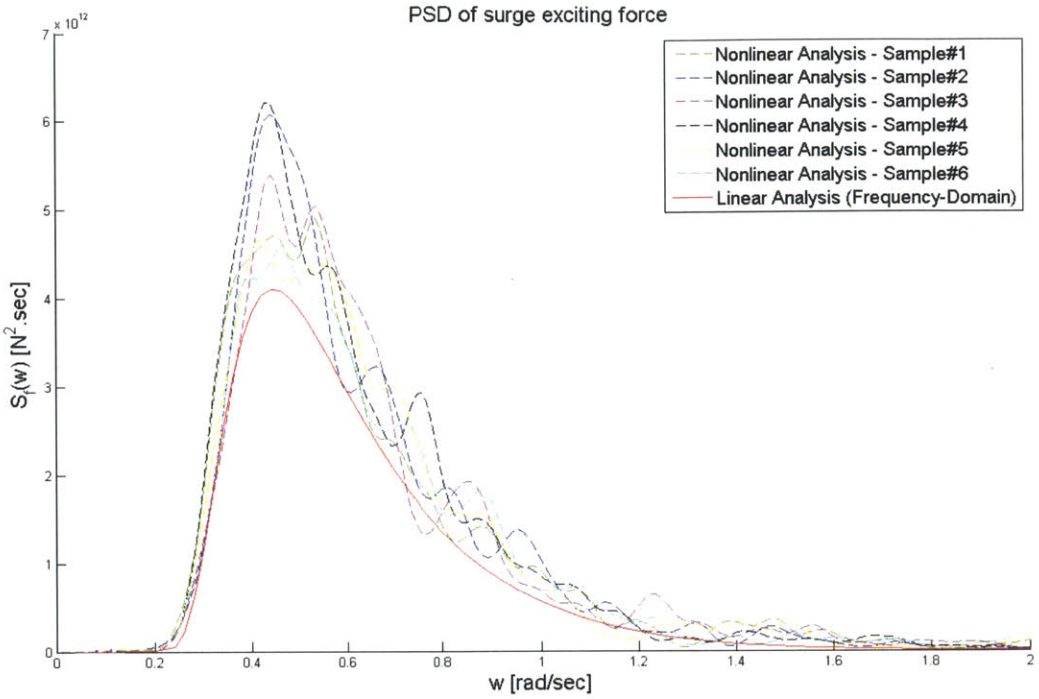


(six samples)

Figure B-8: The power spectral density of wave exciting force in surge ( $F_{Hydro_1}$ ) for irregular waves of $H_s$ = 10.0 m and $T_m$ = 13.6 sec.

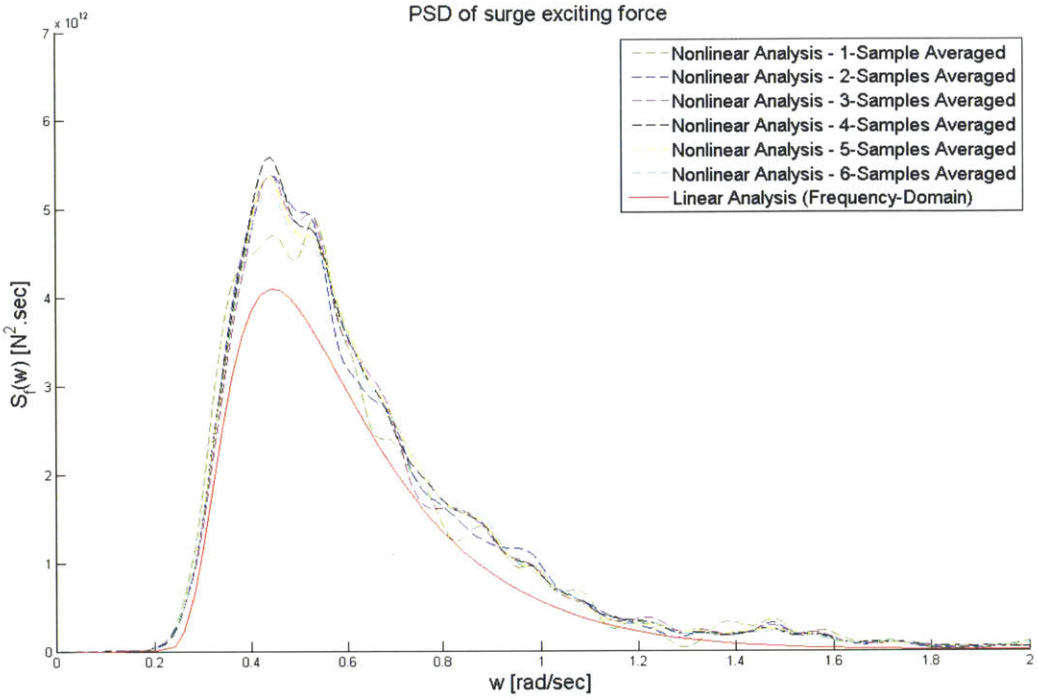


(six averaged-samples)

Figure B-9: The power spectral density of wave exciting force in surge ( $F_{Hydro_1}$ ) for irregular waves of $H_s$ = 10.0 m and $T_m$ = 13.6 sec.

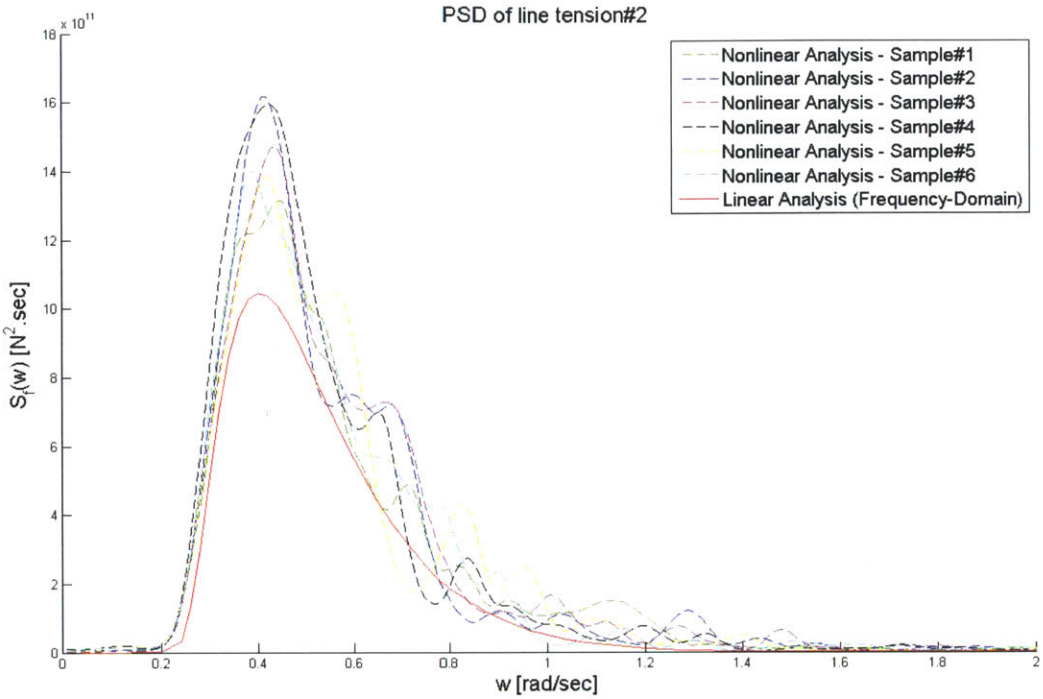


(six samples)

Figure B-10: The power spectral density of tether tension#2 $T_2(\omega)$ for irregular waves of $H_s$ = 10.0 m and $T_m$ = 13.6 sec.

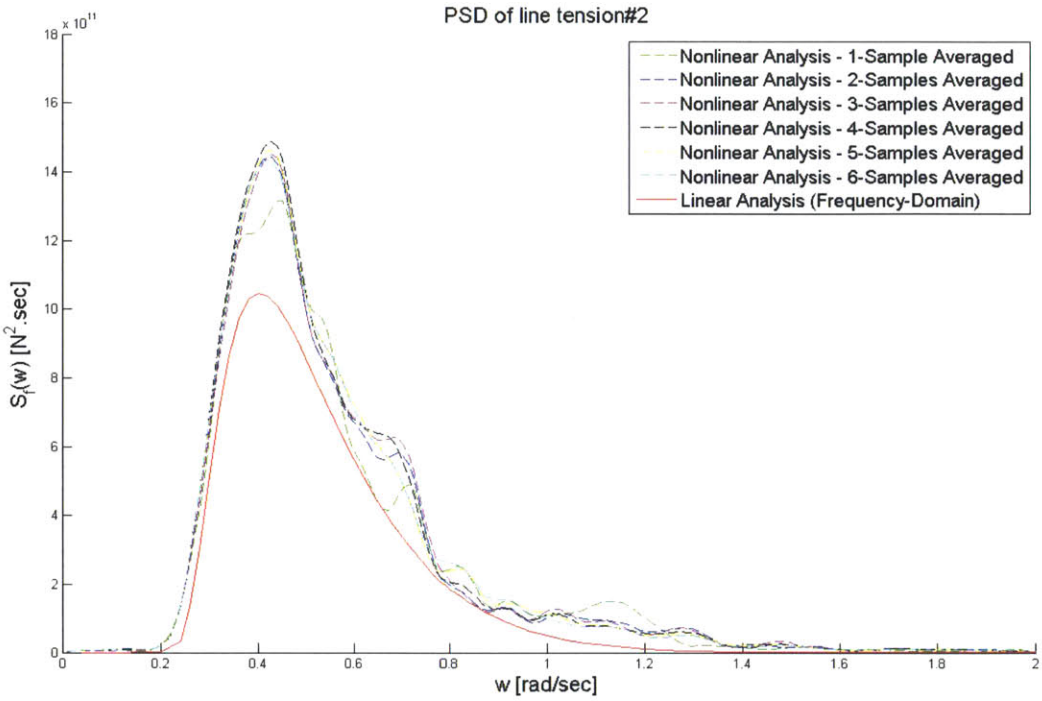


(six averaged-samples)

Figure B-11: The power spectral density of tether tension#2 $T_2(\square)$ for irregular waves of $H_s$ = 10.0 m and $T_m$ = 13.6 sec.

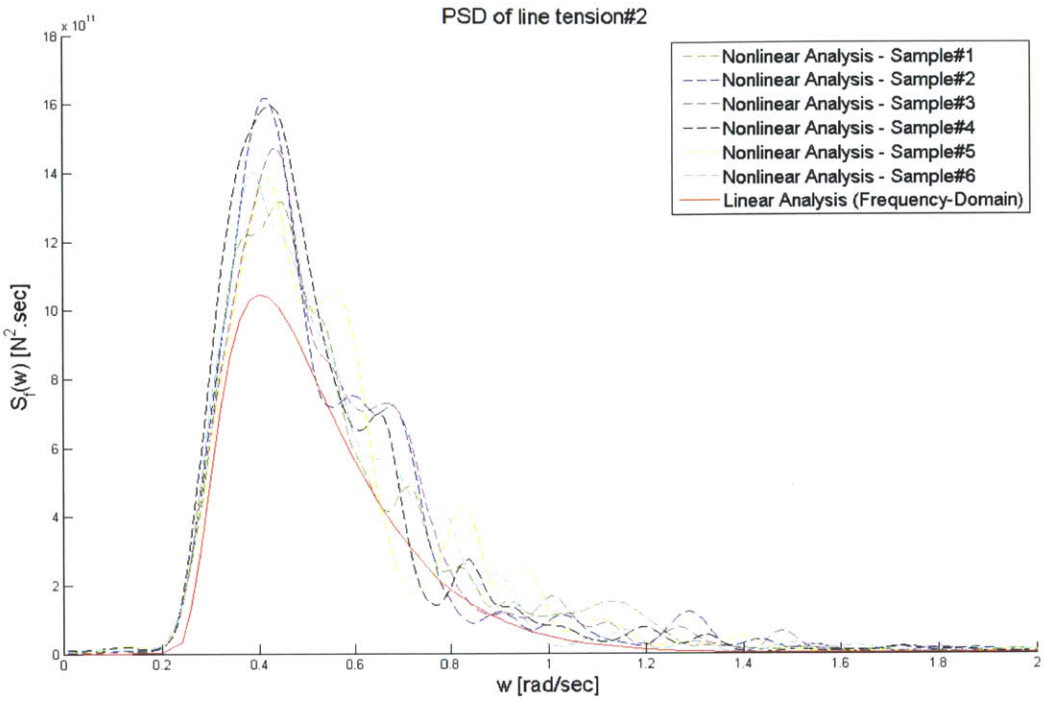


(six samples)

Figure B-12: The power spectral density of tether tension#1 $T_1$(□) for irregular waves of $H_s$ = 10.0 m and $T_m$ = 13.6 sec.

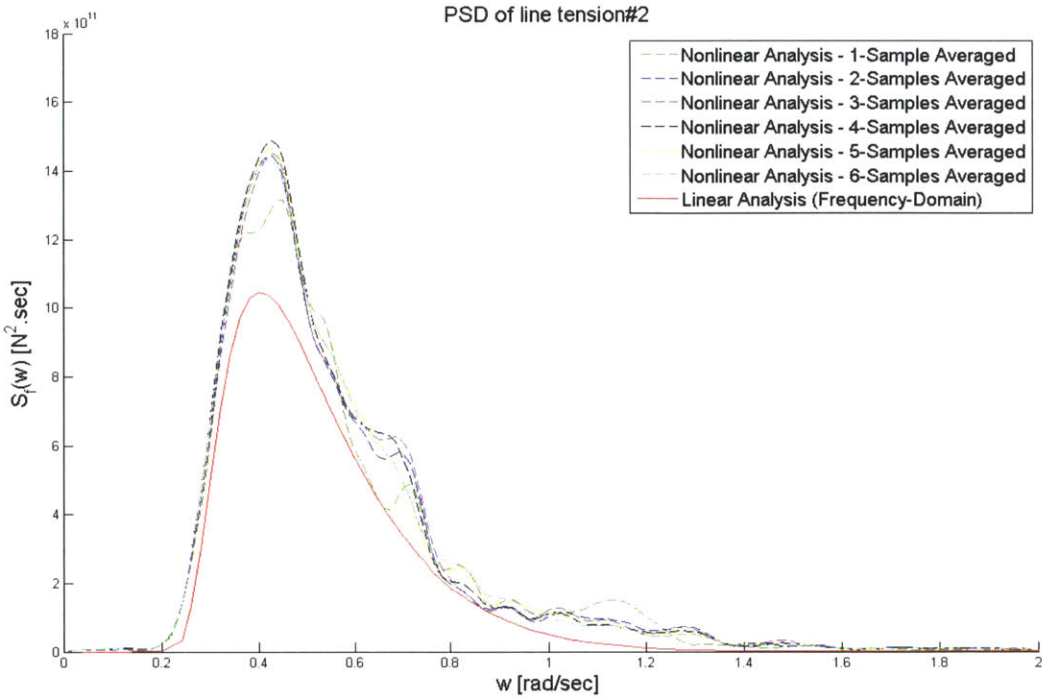


(six averaged-samples)

Figure B-13: The power spectral density of tether tension#1 $T_1(\square)$ for irregular waves of $H_s$ = 10.0 m and $T_m$ = 13.6 sec.

# Bibliography

[1] Abramowitz, M., Stegun, I. "Handbook of mathematical functions with formulas, graphs, and mathematical tables" Dover.

[2] Bingham, H. B. (1994), "Simulating Ship Motions in the Time Domain" Doctoral Thesis. MIT

[3] Beck, R. F. and Magge, A. R., "Time domain analysis for predicting ship motions" IUTAM Symp. Dynamics of Marine Vehicles & Structures in Wave, London, U.K., 1990

[4] Bingham, H. B., Madsen, P. A., "Nonlinear irregular wave forces on near-shore structures by a high-order Boussinesq method"

[5] Chapra, S. C., Canale, R. P. "Numerical methods for engineers" fifth edition, McGraw Hill

[6] Chuang, J. M., Qiu, W., Peng, H., "On the evaluation of time-domain Green function", Ocean Engineering 34 (2007) 962-969

[7] Clement, A. H., "An ordinary differential equation for the Green function of time-domain free-surface hydrodynamics", Journal of Engineering Mathematics 33: 201-217, 1998

[8] St. Denis, M. & Pierson, W.J., On the motions of ships in confused seas, Transactions of the Society of Naval Architects and Marine Engineers, Vol. 61, pp. 280-357, 1953;

[9] Fernandes, A. C. "Analysis of an axissymetric pneumatic buoy by reciprocity relations and a ring-source method" Doctoral thesis, MIT, Dec. 1983.

[10] Froude, W., "On the rolling of ships", Transactions of the Institute of Naval Architecture, Vol. 2, pp. 180-229. 1861.

[11] Faltinsen, O. M., Newman, J. N. and Vinje, T. "Nonlinear wave loads on a slender vertical cylinder" J. Fluid Mech. (1995), vol. 289, pp. 179-198

[12] Faltinsen, O. M., (1990) "Sea Loads on Ships and Offshore Structures" Cambridge University Press.

[13] Huang, Yifeng (1997), "Nonlinear Ship Motions by a Rankine Panel Method" Doctoral Thesis. MIT

[14] Katz, J., Plotkin, A. "Low-speed aerodynamics", McGraw-Hill, Inc.

[15] Krylov, A., "A new theory of the pitching motion of ships on waves", Transactions of the Society of Naval Architectures and Marine Engineers, Vol. 37, pp. 326-368.

[16] Kring, David C. (1994), "Time domain ship motions by a three-dimensional Rankine panel method" Doctoral Thesis. MIT

[17] Sungho Lee, "Dynamic Response Analysis of Spar Buoy Floating Wind Turbine Systems" Masters thesis, MIT, May 2008.

[18] SH. Lee, T. Luypaert, P. Sclavounos, "Fully Coupled Dynamic Modeling and Design Codes for Floating Offshore Wind Turbine Systems: TLP and TLB Concepts in Moderate to Severe Sea

States"[oral presentation] The International Society of Offshore and Polar Engineers ISOPE2011 Conference, Maui, USA, June 2011

[19] Lin, W. M. and Yue, D. K. P. "Large amplitude motions and wave loads for ship design" Twentieth Symp. On Nav. Hydro., Santa Barbara, California, 1994

[20] Newman, J. N. & Sclavounos, P. D., The computation of wave loads on large off-shore structures, 5th International Conference on the behavior of Offshore Structures (BOSS88), Trondheim, Norway, 1988;

[21] Newman, J.N., A slender-body theory for ship oscillations in waves, J. Fluid Mech., Vol. 18, pp. 602-618, 1964;

[22] Newman, J.N., & Tuck, E.O., Current progress in the slender-body theory of ship motions, Proc. 5th Symp. Naval Hydro., pp. 129-167, 1964;

[23] Newman, J. N., Panel methods in marine hydrodynamics, Keynote Lecture, Eleventh Australasian Fluid Mechanics Conference, Hobart, Australia, 1992;

[24] Nakos, D. E., Kring, D. E. and Sclavounos, P. D. "Rankine panel methods for time-domain free surface flows". 6th Intl/. Conf. Num. Ship Hydro., U. Iowa, Iowa City, 1993.

[25] Nakos, D. E. and Sclavounos, P. D. "Ship motions by a three dimensional Rankine panel method", Eighteenth Symp. On Nav. Hydro., Ann Arbor, Michigan, 1990

[26] Newman, J. N., Marine Hydrodynamics, Cambridge, MA: The MIT Press, 1977

[27] Newman, J. N., "Distributions of sources and normal dipoles over a quadrilateral panel", Journal of Engineering Mathematics 20 (1986) 113-126

[28] Ochi, M. K. "Ocean waves, the stochastic approach", Cambridge University Press.

[29] Ogilvie, T.F. & Tuck, E.O., A rational strip theory for ship motions, Part 1, Technical Report 013, The Department of Naval Architecture and Marine Engineering, The University of Michigan, 1969;

[30] Oppenheim, A. V., Willsky, A. S. "signals & systems", second edition, prentice hall, (ISBN: 0-13-814757-4)

[31] Pawlowski, Jack S., "On the Application of the Weak-Scatter Hypothesis on the Prediction of Ship Motions in Heavy Seas"

[32] Pawlowski, Jack S., "A Theoretical and Numerical Model of Ship Motions in Heavy Seas", SNAME Transactions, Vol. 99, 1991, pp. 319-352

[33] "Assessment of offshore wind power resources" Pace Global Energy Services, LLC. 2007 (http://www.lipower.org/newscenter/pr/2007/pace_wind.pdf)

[34] "power spectral density estimation", 18-391 noisy signal representation and processing (http://wiki.nolanhergert.com/lib/exe/fetch.php?media=signals:18391_s11_lab4.pdf)

[35] Sclavounos, P. D., Lee, S., DiPietro, J., Potenza, G., Caramuscio, P. and De Michele G. (2010). "Floating Offshore Wind Turbines: Tension Leg Platform and Taught Leg Buoy Concepts Supporting 3-5 MW Wind Turbines" European Wind Energy Conference EWEC 2010, Warsaw, Poland

[36] Sclavounos, P.D., Tracy, C. and Lee, S., "Floating Offshore Wind Turbines: Responses in a Seastate, Pareto Optimal Designs and Economic Assessment" Offshore Mechanics and Arctic Engineering OMAE 2008 Conference, Lisbon, Portugal, June 2008

[37] Sclavounos, P.D., "Surface Waves and Their Interaction with Floating Bodies" 2.24 Lecture Notes, MIT

[38] Sclavounos, P. D., "On the quadratic effect of random gravity waves on a vertical boundary" J. Fluid Mech. (1992), vol. 242, pp. 475-489

[39] Sclavounos, P. D. (2010) "A Fluid Impulse Theory for the Nonlinear Loads, Responses and Stability of Ships and Floating Structures in Steep Random Waves" Technical Report. Laboratory for Ship and Platform Flows. MIT

[40] Christopher Tracy, "Parametric Design of Floating Wind Turbines" Masters thesis, MIT, May 2007.

[41] Elizabeth Wayman, "Coupled Dynamics and Economic Analysis of Floating Wind Turbine Systems" Masters thesis, MIT, May 2006.

[42] Wehausen, J. V., Laitone, E. V., "Surface waves" Encyclopedia of Physics, pages 446-758, Springer, 1960

[43] Wheeler, J. D. "Method for calculating forces produced by irregular waves", J. of PetroleumTechnology. 249 359-367, 1970.